UCLA
COMPUTATIONAL AND APPLIED MATHEMATICS

A Level Set Approach for Computing Solutions to Incompressible Two-Phase Flow

(Ph.D. Thesis)

Mark Sussman

June 1994

CAM Report 94-13

Department of Mathematics
University of California, Los Angeles
Los Angeles, CA. 90024-1555

UNIVERSITY OF CALIFORNIA

Los Angeles

A level set approach for computing solutions to incompressible two-phase flow

A dissertation submitted in partial satisfaction of the

requirements for the degree Doctor of Philosophy

in Mathematics

by

Mark Sussman

1994

TABLE OF CONTENTS

LIST OF FIGURES

ACKNOWLEDGMENTS

The author wishes to thank Peter Smereka and Stanley Osher for their encouragement and support.

The author also wishes to thank J.M. Morel for bringing an article by Rouy and Tourin to our attention.

The text of this manuscript, excepting material on axisymmetric flow and three-fluid flow, is a preprint of the material as it will appear in the Journal of Computational Physics. The co-authors listed in this publication directed and supervised the research which forms the basis for the manuscript.

Research was supported by ARO DAA L03-91-G0162, a NSF postgraduate fellowship, and in part DARPA/ONR-N00014-92-J-1890, ARO DAA L03-91-G0162, and NSF DMS-91-03104.

ABSTRACT OF THE DISSERTATION

A level set approach for computing solutions to incompressible two-phase flow

by

Mark Sussman

Doctor of Philosophy in Mathematics

University of California, Los Angeles, 1994

Professor Stanley Osher, Chair

A level set approach for computing solutions to incompressible two-phase flow is presented. The interface between the two fluids is considered to be sharp and is described as the zero level set of a smooth function. A new treatment of the level set method allows us to efficiently maintain the level set function as the signed distance from the interface. We never have to explicitly reconstruct or find the zero level set. Consequently, we are able to handle arbitrarily complex topologies, large density and viscosity ratios, and surface tension, on relatively coarse grids. We use a second order projection method along with a second order upwinded procedure for advecting the momentum and level set equations. We consider the motion of air bubbles and water drops. We also compute flows with multiple fluids such as air, oil, and water.

CHAPTER 1

Introduction

A numerical method is developed for computing the motion of incompressible two-phase flow. We will consider immiscible fluids where steep gradients in density and viscosity exist across the interface. Instead of explicitly tracking the interface, we intend to implicitly "capture" the interface using a level set approach. The interface will be identified as the zero level set of a smooth function.

As mentioned in [36], conventional conservative schemes will incur excessive numerical diffusion which will destroy the sharpness of the front. High order conservative schemes can produce numerical oscillations around the front. The approach presented in [36] was to track the velocity using an Eulerian grid while explicitly tracking the interface using a grid that moves through the stationary grid. The investigators cited good results, but the algorithm for tracking the front seems hard to implement. Complications occur when one needs to add or subtract points to the moving grid. These problems are amplified when solving a three dimensional problem.

In [30], a level set formulation for moving interfaces was introduced. The level set function is typically a smooth (Lipschitz continuous) function, denoted as ϕ, which eliminates the problems that conventional difference schemes incur. This

formulation also eliminates the problem of adding/subtracting points to a moving grid and it automatically takes care of merging and breaking of the interface. Furthermore, the level set formulation generalizes well to three dimensions. The actual front location never has to be computed. Instead the front is embedded as a particular level set in a fixed domain PDE.

An application of the level set formulation was used in [27] for compressible fluid flow. Examples from [27] include Kelvin-Helmholtz instability and Rayleigh-Taylor instability for helium and air. The density ratio was about 29 to 4 and both gases were treated as perfect gases. These investigators found it was best to initialize ϕ as the signed distance from the front, thus eliminating steep gradients from ϕ. A second-order non-conservative ENO scheme was used for solving the equation for ϕ.

Instead of helium and air, we shall consider water and air. The density ratio of water to air is about 1000 to 1 and the equation of state for water is not that of a perfect gas. One can approximate the flow of water in the compressible framework if one replaced pressure P with $P + B$ and γ with N. B and N are constants derived from the modified Tait equation (see, for example, [12]). For compressible flow there would be a restriction put on the size of the time step since the sound speed of water is about five times that of air at sea level. In order to avoid this restriction, we will solve the problems involving water and air using the equations for incompressible flow. This is a very good approximation as long as the fluid velocities are much smaller than the speed of sound.

Incompressible flow algorithms that have been used to track the interface of air/water problems include vortex methods [2], boundary integral methods [3], volume tracking methods [15, 18, 10], front tracking methods [36], and projection methods [6, 14, 21, 20]. We will use a projection method similar to [6]. If one combines the level set techniques of [30] with a projection method (see [41]), one can avoid having to explicitly track the interface (hence the term "front capturing"). Furthermore, one can use higher order upwinded methods for differencing the non-linear convective terms. These methods provide robust treatment of convective terms at high Reynolds numbers ([35, 40, 37, 17]).

In this paper we shall also combine a level set technique with a projection method. Our approach allows for large density ratios (about 1000 to 1), surface tension, and jumps in viscosity, while retaining a high order of accuracy. The important feature of our method is that we maintain our level set function as a distance function for all time, without reconstructing the interface. This prevents the interface from ever changing thickness.

CHAPTER 2

Description of Algorithm

2.1 Equations of Motion

In our study we shall consider the fluid motion for rising air bubbles in water and falling water drops in air. We shall denote the density and viscosity inside the bubble (or drop) by ρ_b and μ_b respectively and for the continuous phase by ρ_c and μ_c. The equations of motion are given by the incompressible Navier-Stokes equations

$$\vec{u}_t + (\vec{u} \cdot \vec{\nabla})\vec{u} = \vec{F} + \frac{1}{\rho}(-\vec{\nabla}p + \vec{\nabla} \cdot (2\mu D) + \sigma\kappa\delta(d)\vec{n}) \tag{2.1}$$

$$\vec{\nabla} \cdot \vec{u} = 0 \tag{2.2}$$

where $\vec{u} = (u, v)$ is the fluid velocity, $\rho = \rho(\vec{x}, t)$ is the fluid density, $\mu = \mu(\vec{x}, t)$ is the fluid viscosity, D is the viscous stress tensor, and $\vec{F}$ is a body force. The surface tension term is considered to be a force concentrated on the interface. We denote σ as the surface tension, κ as the curvature of the front, d as the normal distance to the front, δ as the Dirac delta function, and $\vec{n}$ as the unit outward

normal vector at the front. For immiscible liquids the density and viscosity are constant on particle paths, therefore

$$\rho_t + (\vec{u} \cdot \vec{\nabla})\rho = 0 \tag{2.3}$$

$$\mu_t + (\vec{u} \cdot \vec{\nabla})\mu = 0. \tag{2.4}$$

We will assume solid wall boundaries with the free-slip condition

$$\vec{u} \cdot \vec{n} = 0 \tag{2.5}$$

where $\vec{n}$ is the normal vector at the boundary.

The initial radius of the bubble (or drop) is denoted as R and the only body force we consider is gravity denoted as $\vec{g}$.

After the non-dimensionalization of (2.1) we have:

$$\begin{aligned} \vec{u}_t &= -(\vec{u} \cdot \vec{\nabla})\vec{u} + \vec{g}_u + \frac{1}{\rho}(-\vec{\nabla}p + \frac{1}{Re}\vec{\nabla} \cdot (2\mu D) + \frac{1}{B}\kappa\delta(d)\vec{n}) \\ &\equiv L\vec{u} - \vec{\nabla}p/\rho. \end{aligned} \tag{2.6}$$

The key parameters are ρ_b/ρ_c, dimensionless density inside the bubble, μ_b/μ_c, dimensionless viscosity inside the bubble, $Re = (2R)^{\frac{3}{2}}\sqrt{g}\rho_c/\mu_c$, Reynolds number, and $B = 4\rho_c g R^2/\sigma$, Bond number. The dimensionless density and viscosity outside the bubble are equal to 1. We have $\vec{g}_u$ represent a unit gravitational force.

2.2 Projection

From (2.6), we have $\vec{u}_t = L\vec{u} - \vec{\nabla}p/\rho$. Let $\vec{V} = L\vec{u}$. As noted in [5, 14], if the initial value problem for equation (2.6) is well posed, then there exists a unique decomposition (Hodge decomposition) where $\vec{V} = \vec{V}_d + \vec{\nabla}\psi$ and $\vec{V}_d$ is divergence free. As in [6], we define a density weighted inner product such that we can decompose $\vec{V}$ into $\vec{V}_d$ and $\vec{\nabla}\psi/\rho$. Given our density weighted norm, we have $\vec{V}_d \perp \vec{\nabla}\psi/\rho$. Given a vector $\vec{V}$, we define our projection operator as $\vec{P}_\rho(\vec{V}) \equiv \vec{V}_d$. Since the Hodge decomposition is unique and $\vec{u}_t$ is divergence free, we have $\vec{u}_t = \vec{P}_\rho(L\vec{u})$. So, (2.6) and (2.2) are reduced to

$$\vec{u}_t = \vec{P}_\rho(L\vec{u}). \tag{2.7}$$

In order to compute the projection, we take the curl of both sides of the equation $\rho\vec{V} = \rho\vec{V}_d + \vec{\nabla}\psi$ to obtain

$$\vec{\nabla} \times (\rho\vec{V}) = \vec{\nabla} \times (\rho\vec{V}_d).$$

Given any divergence free vector $\vec{V}_d$, there exists a stream function $\vec{\Psi}$ such that $\vec{V}_d = \vec{\nabla} \times \vec{\Psi}$. Furthermore, in two dimensions we have $\vec{\Psi} = (0, 0, \Psi)$. The above equation can now be written as

$$-\vec{\nabla}(\rho\vec{\nabla}\Psi) = \vec{\nabla} \times (\rho\vec{V}). \tag{2.8}$$

We consider problems obeying the free-slip condition (2.5); hence $\Psi = 0$ on the boundary.

2.3 Level Set Description

Since ρ and μ change sharply at the front, conventional finite difference schemes will incur excessive numerical diffusion when solving (2.3) and (2.4). Instead, we shall use the level set technique to "capture" the interface as in [27] and [41]. Our level set function is denoted as ϕ and it is taken positive outside the bubble and negative inside the bubble. Therefore, the bubble interface is the zero level set of ϕ. We shall initialize ϕ to be the signed normal distance from the interface. Consider the following equation

$$\phi_t + (\vec{u} \cdot \vec{\nabla})\phi = 0$$

This equation will move the zero level set of ϕ exactly as the actual bubble interface moves. Since ϕ is a smooth function, unlike ρ or μ, the above equation is more easily solved numerically. Therefore equations (2.3), (2.4), and (2.7) can be written as

$$\vec{u}_t = \vec{P}_\rho(L\vec{u}) \tag{2.9}$$

$$\phi_t = -(\vec{u} \cdot \vec{\nabla})\phi \tag{2.10}$$

$$\rho = \begin{cases} 1 & \text{if } \phi > 0 \\ \rho_b/\rho_c & \text{if } \phi < 0 \\ (\rho_b + \rho_c)/(2\rho_c) & \text{if } \phi = 0 \end{cases} \tag{2.11}$$

$$\mu = \begin{cases} 1 & \text{if } \phi > 0 \\ \mu_b/\mu_c & \text{if } \phi < 0 \\ (\mu_b + \mu_c)/(2\mu_c) & \text{if } \phi = 0 \end{cases} \tag{2.12}$$

We shall solve the above system in the domain

$$\Omega = \{(x, y) \mid 0 \leq x \leq 7R, 0 \leq y \leq 7R\},$$

where $\vec{u}$ obeys the free slip condition (2.5) on $\partial\Omega$.

It should be noted that while ϕ is initially a distance function it will not remain so. Furthermore, solutions of ϕ can develop a jump at the interface when interfaces merge. Below we shall present a novel way of reinitializing ϕ so that it remains a distance function.

2.4 Smoothing

Special care must be taken when resolving the discontinuity in the equation for density at $\phi = 0$ and when computing the delta function that appears in the surface tension term.

If we use (2.11) for determining $\rho(\phi)$, the solution of the elliptic system (2.8) will yield unwanted instabilities at the interface; especially for large density ratios. A method was proposed in [24] for solving (2.8) with a discontinuous ρ. Unfortunately, this method would require the solution of a non-symmetric matrix and the method is difficult to implement. In order to prevent instabilities, we decided to

smooth ρ at the interface. We have the following equation for $\rho(\phi)$:

$$H_\alpha(\phi) \equiv \begin{cases} 1 & \text{if } \phi > \alpha \\ 0 & \text{if } \phi < -\alpha \\ \frac{1}{2}(1 + \frac{\phi}{\alpha} + \frac{1}{\pi}\sin(\pi\phi/\alpha)) & \text{otherwise} \end{cases} \tag{2.13}$$

$$\rho(\phi) = H_\alpha(\phi) + \rho_b/\rho_c(1 - H_\alpha(\phi)) \tag{2.14}$$

The above equation for ρ effectively gives the interface a finite thickness α. $H_\alpha(\phi)$ is our smoothed "Heaviside function". α is constant with respect to time and is assigned values with size $O(h)$. A justification for spreading the interface can be found on p.29 of [36]. Implicit in the above formula is that ϕ is a distance function. This important point will be discussed in section 2.5 below.

The surface tension force is represented by

$$\frac{1}{B}\kappa\delta(d)\vec{n}.$$

As pointed out in [11, 10], the surface tension force can be cast in the level set formulation and smoothed using:

$$(1/B)\kappa\delta(d)\vec{n} = (1/B)\kappa(\phi)\delta(\phi)\vec{\nabla}\phi,$$

where the curvature is

$$\kappa(\phi) = \vec{\nabla} \cdot (\frac{\vec{\nabla}\phi}{|\vec{\nabla}\phi|}). \tag{2.15}$$

If we maintain ϕ as a distance function, as we shall do, then we may numerically approximate $\delta(\phi)$ by a mollified delta function, $\delta_\alpha(\phi)$, smoothed in similar fashion as in [31]:

$$\delta_\alpha(\phi) = \partial H_\alpha(\phi)/\partial\phi$$

$H_\alpha(\phi)$ is defined by equation (2.13) as our smoothed "Heaviside" function. We denote α as the prescribed "thickness" of the interface. In our computations, we use $\alpha = \frac{3}{2}\Delta x$.

2.4.0.1 Inclusion of surface tension into the projection step

When surface tension is active, special care must be taken when computing the right hand side of (2.8). The contribution of surface tension to $\vec{\nabla} \times (\rho \vec{V})$ is

$$-\frac{1}{B}((\kappa(\phi)\delta(\phi)\phi_y)_x - (\kappa(\phi)\delta(\phi)\phi_x)_y)). \tag{2.16}$$

We write $\delta(\phi)$ as $\partial H(\phi)/\partial\phi$. It follows that we can reduce (2.16) to

$$-\frac{1}{B}(\kappa(\phi)_x H_y - \kappa(\phi)_y H_x). \tag{2.17}$$

The equation for $H_\alpha(\phi)$ is defined by equation (2.13).

By writing the surface tension contribution in our "Heaviside" formulation, we eliminate the numerical instabilities that occur when differentiating a delta function.

2.5 Keeping ϕ a Distance Function

While equation (2.10) will move the level set $\phi = 0$ at the correct velocity, ϕ will no longer be a distance function (i.e. $\mid \vec{\nabla}\phi \mid \neq 1$). ϕ can become irregular

after some period of time (see figures 7.1 and 7.2). For example when two bubbles (or drops) merge, a steep gradient in ϕ will arise between the bubbles. Also, a drop moving at constant speed will cause a steep gradient to form in the distance function after a finite amount of time. Maintaining ϕ as a distance function is essential for providing the interface with a width fixed in time. Computation of surface tension is difficult to compute near a steep gradient in the distance function. The values for $\rho(\phi)$, especially for large density ratios, will be greatly distorted if $\mid \vec{\nabla}\phi \mid$ is far from one. In fig. 7.3, we see that without reinitialization, the drop loses 41% of mass at time $t = 3.5$ while mass is conserved with reinitialization. In fig. 7.4, we compare results at time $t = 8.8$ for a gas bubble rising with large surface tension and viscosity. Without reinitialization, the bubble loses 19% of mass and the velocity does not attain a steady state. Furthermore the bubble shape does not attain the characteristic steady state of an ellipsoid. With reinitialization, the bubble velocity and minor axis attain a steady state and the bubble mass is conserved (see figures 7.5,7.6,7.7, and 7.8).

Conventional routines for re-initializing a distance function have to explicitly find the contour $\phi = 0$ and reset ϕ at all points close to the front. This takes $O(n^3)$ operations (see [13]) and can distort the front (e.g. mass loss, corners) depending on how one reconstructs the shape of the contour $\phi = 0$. Through our experiments, we have found that one needs to reinitialize ϕ after every time step in order to keep the solution accurate. Thus any distortions from constantly re-initializing ϕ are amplified.

An iteration method for re-initializing ϕ was introduced by [33]. Given a region Ω^+ with $\phi \geq 0$ on Ω^+ and $\phi = 0$ on $\partial\Omega^+$, evolve the equation $\phi_t = 1 - |\vec{\nabla}\phi|$ until ϕ reaches a steady state. If ϕ is already close to a distance function, then one should not have to evolve too far in time.

Unfortunately, one still has to prescribe boundary conditions on $\partial\Omega^+$ which entails explicitly finding the interface. We can eliminate the problem of finding the interface. Consider the following function $\phi_0(\vec{x})$ whose zero level set is the air-liquid interface; $\phi_0(\vec{x})$ need not be a distance function, however. We shall construct a function, $\phi(\vec{x})$, with the properties that its zero level set is the same as $\phi_0(\vec{x})$ and that ϕ is the signed normal distance to the interface. This is achieved by solving the following problem to steady state

$$\phi_t = S(\phi_0)(1 - \sqrt{\phi_x^2 + \phi_y^2}) \tag{2.18}$$

$$\phi(\vec{x}, 0) = \phi_0(\vec{x}), \tag{2.19}$$

where S is the sign function. For numerical purposes it is useful to smooth the sign function; we do this as

$$S_\epsilon(\phi_0) = \frac{\phi_0}{\sqrt{\phi_0^2 + \epsilon^2}} \tag{2.20}$$

Equation (2.18) has the property that ϕ remains unchanged at the interface; therefore the zero level set of ϕ_0 and ϕ are the same. Away from the interface ϕ will converge to $|\vec{\nabla}\phi| = 1$. Therefore, it will converge to the actual distance. The above algorithm completely avoids finding the interface and it proves to be

efficient to implement numerically. In our computations, one iteration per time step was usually enough for meeting our convergence criterion. In [33], existence and uniqueness proofs are provided for the problem:

$$| \vec{\nabla}\phi(\vec{x}) | = \lambda(\vec{x}) \text{ in } \Omega^+ \qquad (2.21)$$

$$\phi(\vec{x}) = 0 \text{ on } \partial\Omega^+$$

In our case $\lambda(\vec{x}) = 1$.

2.6 Summary

We can now summarize our algorithm.

Step 1 Initialize $\phi(\vec{x}, 0)$ to be signed normal distance to the front.

Step 2 Solve

$$\vec{u}_t = P_\rho(\vec{u}) \quad \text{and} \quad \phi_t + \vec{u} \cdot \vec{\nabla}\phi = 0$$

for one time step with $\rho(\phi)$ given by (2.14), $\mu(\phi)$ given by (2.12), and the surface tension force given by (2.17). Denote the updated ϕ by $\phi^{(n+\frac{1}{2})}$, and the updated $\vec{u}$ by $\vec{u}^{(n+1)}$.

Step 3 Construct a new distance function by solving

$$\phi_t = S(\phi^{(n+\frac{1}{2})})(1 - |\vec{\nabla}(\phi)|) \quad \text{with} \quad \phi(\vec{x}, 0) = \phi^{(n+\frac{1}{2})}(\vec{x})$$

to steady state. We denote the steady state solution by $\phi^{(n+1)}$.

Step 4 We have now advanced one time step. The zero level set of $\phi^{(n+1)}$ gives the new interface position and $\phi^{(n+1)}$ is a distance function. Repeat steps 2 and 3.

CHAPTER 3

Discretization

A staggered mesh will be used for the velocity and the distance function. With h as the mesh size, we define

$$\begin{aligned} \vec{x}_{i,j} &= ((i+\frac{1}{2})h, (j+\frac{1}{2})h) \\ \vec{u}_{i,j} &= \vec{u}(\vec{x}_{i,j}) \\ \phi_{i,j} &= \phi(\vec{x}_{i,j}) \end{aligned}$$

$$\begin{aligned} i &= 0 \ldots M-1 \\ j &= 0 \ldots N-1. \end{aligned}$$

For a square box, we have $Mh = 7R$ and $Nh = 7R$. For a rectangular box, we have $Mh = 5R$ and $Nh = 10R$.

3.1 Discretization in Time

We will use a second order Adam Bashforth method for evolving the equation in time (see [21]).

$$\vec{u}^{n+1} = \vec{u}^n + k(\frac{3}{2}\vec{P}_{\rho^n}(L\vec{u}^n) - \frac{1}{2}\vec{P}_{\rho^{n-1}}(L\vec{u}^{n-1})) \tag{3.1}$$

where k is the time step. A similar formula as above is used in discretizing the equation for ϕ.

3.2 Convection Terms

We will use a second order ENO method for the approximation of the convective terms.

For $\vec{u}$ divergence free, we have:

$$(\vec{u}\cdot\vec{\nabla})\phi = (u\phi)_x + (v\phi)_y \tag{3.2}$$

$$(\vec{u}\cdot\vec{\nabla})\vec{u} = \vec{f}_x + \vec{g}_y \tag{3.3}$$

where

$$f = \begin{pmatrix} u^2 \\ uv \end{pmatrix} \; g = \begin{pmatrix} uv \\ v^2 \end{pmatrix} \tag{3.4}$$

For a conservative scheme, we approximate f_x using $f_{i+\frac{1}{2},j} - f_{i-\frac{1}{2},j}$. Unfortunately, there are unwanted oscillations since (3.3) is not always numerically accurate. We will use an algorithm similar to that of equation (2.9) in [6]. For the equation for ϕ, we have:

$$\begin{aligned}
(u\phi)_x + (v\phi)_y &\approx ((u\phi)_{i+\frac{1}{2},j} - (u\phi)_{i-\frac{1}{2},j} + (v\phi)_{i,j+\frac{1}{2}} - (v\phi)_{i,j-\frac{1}{2}})/(2h) \\
&= (u_{i+\frac{1}{2},j} + u_{i-\frac{1}{2},j})(\phi_{i+\frac{1}{2},j} - \phi_{i-\frac{1}{2},j})/(2h) \\
&+ (v_{i,j+\frac{1}{2}} + v_{i,j-\frac{1}{2}})(\phi_{i,j+\frac{1}{2}} - \phi_{i,j-\frac{1}{2}})/(2h) \\
&+ (\phi_{i+\frac{1}{2},j} + \phi_{i-\frac{1}{2},j})(u_{i+\frac{1}{2},j} - u_{i-\frac{1}{2},j})/(2h)
\end{aligned}$$

$$+ \quad (\phi_{i,j+\frac{1}{2}} + \phi_{i,j-\frac{1}{2}})(v_{i,j+\frac{1}{2}} - v_{i,j-\frac{1}{2}})/(2h)$$

For smooth data, we have $\phi_{i+\frac{1}{2},j}+\phi_{i-\frac{1}{2},j} \approx \phi_{i,j+\frac{1}{2}}+\phi_{i,j-\frac{1}{2}}$. Since $\vec{u}$ is numerically divergence free, we have $u_{i+\frac{1}{2},j} - u_{i-\frac{1}{2},j} \approx -(v_{i,j+\frac{1}{2}} - v_{i,j-\frac{1}{2}})$. We find the following approximation

$$\begin{aligned}(u\phi)_x + (v\phi)_y &\approx (u_{i+\frac{1}{2},j} + u_{i-\frac{1}{2},j})(\phi_{i+\frac{1}{2},j} - \phi_{i-\frac{1}{2},j})/(2h) \\ &+ (v_{i,j+\frac{1}{2}} + v_{i,j-\frac{1}{2}})(\phi_{i,j+\frac{1}{2}} - \phi_{i,j-\frac{1}{2}})/(2h).\end{aligned}$$

Similarly we have

$$\begin{aligned}(f_1)_x + (g_1)_y &\approx (u_{i+\frac{1}{2},j} + u_{i-\frac{1}{2},j})(u_{i+\frac{1}{2},j} - u_{i-\frac{1}{2},j})/(2h) \\ &+ (v_{i,j+\frac{1}{2}} + v_{i,j-\frac{1}{2}})(u_{i,j+\frac{1}{2}} - u_{i,j-\frac{1}{2}})/(2h) \\ (f_2)_x + (g_2)_y &\approx (u_{i+\frac{1}{2},j} + u_{i-\frac{1}{2},j})(v_{i+\frac{1}{2},j} - v_{i-\frac{1}{2},j})/(2h) \\ &+ (v_{i,j+\frac{1}{2}} + v_{i,j-\frac{1}{2}})(v_{i,j+\frac{1}{2}} - v_{i,j-\frac{1}{2}})/(2h).\end{aligned}$$

For computing $u_{i+\frac{1}{2},j}$ (similarly for $u_{i,j+\frac{1}{2}}$, $\phi_{i+\frac{1}{2},j}$, $\ldots$), we use a second order ENO scheme (see [35, 27]):

Define

$$m(a,b) \equiv \begin{cases} a & \text{if } \mid a \mid \leq \mid b \mid \\ b & \text{otherwise} \end{cases}.$$

Let

$$u_L \equiv u_{i,j} + \frac{1}{2} m(u_{i+1,j} - u_{i,j}, u_{i,j} - u_{i-1,j})$$

$$
\begin{aligned}
u_R &\equiv u_{i+1,j} - \frac{1}{2} m(u_{i+2,j} - u_{i+1,j}, u_{i+1,j} - u_{i,j}) \\
u_M &\equiv \frac{1}{2}(u_L + u_R).
\end{aligned}
$$

We now have

$$
u_{i+\frac{1}{2},j} \equiv \begin{cases} u_M & \text{if } u_L \leq 0 \text{ and } u_R \geq 0 \\ u_R & \text{if } u_M \leq 0 \text{ and } u_R \leq 0 \\ u_L & \text{if } u_M \geq 0 \text{ and } u_L \geq 0 \end{cases} .
$$

3.3 Viscous and Curvature Terms

We approximate the components of the viscous stress tensor D using central differencing:

$$
\begin{aligned}
(u_x)_{i+1/2,j+1/2} &\approx (u_{i+1,j} + u_{i+1,j+1} - u_{i,j} - u_{i,j+1})/(2h) \\
(u_y)_{i+1/2,j+1/2} &\approx (u_{i+1,j+1} - u_{i+1,j} + u_{i,j+1} - u_{i,j})/(2h).
\end{aligned}
$$

Similar equations are used for v_x and v_y.

The divergence of the stress tensor is computed as follows:

$$
\begin{aligned}
((\mu D^{m,n})_x)_{i,j} &\approx ((\mu D^{m,n})_{i+1/2,j+1/2} + (\mu D^{m,n})_{i+1/2,j-1/2} \\
&\quad -(\mu D^{m,n})_{i-1/2,j+1/2} - (\mu D^{m,n})_{i-1/2,j-1/2})/(2h) \\
((\mu D^{m,n})_y)_{i,j} &\approx ((\mu D^{m,n})_{i+1/2,j+1/2} - (\mu D^{m,n})_{i+1/2,j-1/2} \\
&\quad +(\mu D^{m,n})_{i-1/2,j+1/2} - (\mu D^{m,n})_{i-1/2,j-1/2})/(2h)
\end{aligned}
$$

with

$$\mu_{i+\frac{1}{2},j+\frac{1}{2}} = (\mu_{i,j} + \mu_{i+1,j} + \mu_{i,j+1} + \mu_{i+1,j+1})/4.$$

We use the free-slip condition (2.5) to determine the discretization at the left boundary. For example,

$$(u_x)_{-\frac{1}{2},j+\frac{1}{2}} = 2(u_{0,j} + u_{0,j+1})/(2h)$$

$$\mu_{-\frac{1}{2},j+\frac{1}{2}} = (\mu_{0,j} + \mu_{0,j+1})/2.$$

Similar equations are used for the other boundaries.

The curvature is discretized in the same fashion as the discretization of the divergence of the viscous stress tensor.

3.4 Discretization of the Projection

Given $\vec{V} \equiv L\vec{u}^n$, we decompose $\vec{V}$ into the form $\vec{V}_d + \vec{\nabla}\psi/\rho$ where $\vec{V}_d$ is divergence free and define $\vec{P}^n_\rho(L\vec{u}^n) \equiv \vec{V}_d$ and $\vec{\nabla}p^n \equiv \vec{\nabla}\psi$. Following [6], in order to define the discrete approximation of the projection, we must first define discrete divergence and gradient operators and a discrete ρ-weighted inner product.

For divergence we have:

$$(\vec{\nabla}\cdot\vec{U})_{i+\frac{1}{2},j+\frac{1}{2}} \approx (D\vec{U})_{i+\frac{1}{2},j+\frac{1}{2}} \equiv$$

$$(u_{i+1,j+1} - u_{i,j+1} + u_{i+1,j} - u_{i,j})/(2h)$$

$$+(v_{i+1,j+1} - v_{i+1,j} + v_{i,j+1} - v_{i,j})/(2h)$$

For the gradient we have:

$$\begin{aligned}
(\vec{\nabla}\Phi)_{i,j} \approx (\vec{G}\Phi)_{i,j} &\equiv ((G_x\Phi)_{i,j}, (G_y\Phi)_{i,j}) \\
(G_x\Phi)_{i,j} &\equiv (\Phi_{i+\frac{1}{2},j+\frac{1}{2}} - \Phi_{i-\frac{1}{2},j+\frac{1}{2}} + \Phi_{i+\frac{1}{2},j-\frac{1}{2}} - \Phi_{i-\frac{1}{2},j-\frac{1}{2}})/(2h) \\
(G_y\Phi)_{i,j} &\equiv (\Phi_{i+\frac{1}{2},j+\frac{1}{2}} - \Phi_{i+\frac{1}{2},j-\frac{1}{2}} + \Phi_{i-\frac{1}{2},j+\frac{1}{2}} - \Phi_{i-\frac{1}{2},j-\frac{1}{2}})/(2h)
\end{aligned}$$

For the inner product we have:

$$(\vec{V}_1, \vec{V}_2)_\rho \equiv \sum_{i=0}^{M-1} \sum_{j=0}^{N-1} (\vec{V}_{1,ij} \cdot \vec{V}_{2,ij}) \rho_{ij}$$

Note: The divergence operator and Φ are defined at the cell corners $\vec{x}_{i+\frac{1}{2},j+\frac{1}{2}}$ where $i = -1 \ldots M-1$ and $j = -1 \ldots N-1$.

With the above definitions for D and G, the discrete operators are skew adjoint ($G = -D^T$ see [6]). Using our definitions of G, D and $(\cdot,\cdot)_\rho$, discretely divergence free vector fields with zero normal components are orthogonal to discrete vector fields of the form $\vec{G}\Phi/\rho$. Consequently, we can uniquely decompose any discrete vector field into $\vec{U} + \vec{G}\Phi/\rho$ where $D\vec{U} = 0$.

In two dimensions, a divergence free vector can be written as the curl of a vector $\vec{\Psi} = (0, 0, \Psi)$ (see p. 77-78 of [4]). Define a discrete function Ψ at the cell corners $\vec{x}_{i+\frac{1}{2},j+\frac{1}{2}}$. Since our divergence free vector field has zero normal component at the boundary, $\Psi = 0$ at the boundary ($i = -1, M-1$ or $j = -1, N-1$). Define $\vec{G}^\perp\vec{W}$ as the discrete curl of $\vec{W}$; e.g. $\vec{G}^\perp\vec{\Psi} \equiv (G_y\Psi, -G_x\Psi)$. Then we have :

$$\vec{G}^\perp\vec{\Psi} + \vec{G}\psi/\rho = \vec{V} \tag{3.5}$$

$$\vec{G}^{\perp}(\rho\vec{G}^{\perp}\vec{\Psi}) = \vec{G}^{\perp}(\rho\vec{V}) \tag{3.6}$$

$$-G_x(\rho(G_x\Psi)) - G_y(\rho(G_y\Psi)) = G_x(\rho V_2) - G_y(\rho V_1) \tag{3.7}$$

When surface tension is active, we modify the right hand side of (3.7) using our Heaviside formulation (2.17).

The difference formula for (3.7) is

$$\begin{aligned} &- \Big[\rho_{i,j}\Psi_{i-\frac{1}{2},j-\frac{1}{2}} + \rho_{i,j+1}\Psi_{i-\frac{1}{2},j+\frac{3}{2}} + \rho_{i+1,j}\Psi_{i+\frac{3}{2},j-\frac{1}{2}} + \rho_{i+1,j+1}\Psi_{i+\frac{3}{2},j+\frac{3}{2}} \\ &\quad -(\rho_{i,j} + \rho_{i+1,j} + \rho_{i,j+1} + \rho_{i+1,j+1})\Psi_{i+\frac{1}{2},j+\frac{1}{2}}\Big] \\ &\quad = G_x(\rho\tilde{V}_2) - G_y(\rho\tilde{V}_1) - \frac{1}{B}(G_x\kappa(\phi)G_yH - G_y\kappa(\phi)G_xH) \end{aligned}$$

where $\tilde{\vec{V}}$ is $\vec{V}$ with the surface tension terms excluded.

Once Ψ is known, we can set $\vec{U} \equiv \vec{G}^{\perp}\Psi$. The matrix system is solved using a preconditioned conjugate gradient (PCG) algorithm using an incomplete Cholesky factorization as a preconditioner. The initial data for the PCG algorithm is a linear combination of the results of previous time steps.

3.5 The Reinitialization of ϕ

In this section, we describe how to numerically evolve (2.18) to steady state. We can write (2.18) in the form

$$\phi_t + \vec{w}\cdot\vec{\nabla}\phi = S(\phi_0) \tag{3.8}$$

where

$$\vec{w} = S(\phi_0)\frac{\vec{\nabla}\phi}{|\vec{\nabla}\phi|}.$$

Equation (3.8) is a nonlinear hyperbolic equation whose characteristics are given by $\vec{w}$. The vector $\vec{w}$ is a unit normal always pointing outward from the zero level set ($\phi = 0$).

One possible discretization of (2.18) is as follows. We define

$$\begin{aligned} a \equiv D_x^- \phi_{i,j} &= (\phi_{i,j} - \phi_{i-1,j})/h \\ b \equiv D_x^+ \phi_{i,j} &= (\phi_{i+1,j} - \phi_{i,j})/h \\ c \equiv D_y^- \phi_{i,j} &= (\phi_{i,j} - \phi_{i,j-1})/h \\ d \equiv D_y^+ \phi_{i,j} &= (\phi_{i,j+1} - \phi_{i,j})/h \end{aligned}$$

and

$$\begin{aligned} S_\epsilon(\phi)_{i,j} &= \phi_{i,j}/\sqrt{\phi_{i,j}^2 + \epsilon^2} \\ G(\phi)_{i,j} &= \begin{cases} \sqrt{\max((a^+)^2,(b^-)^2) + \max((c^+)^2,(d^-)^2)} - 1 & \text{if } \phi_{i,j}^0 > 0 \\ \sqrt{\max((a^-)^2,(b^+)^2) + \max((c^-)^2,(d^+)^2)} - 1 & \text{if } \phi_{i,j}^0 < 0 \\ 0 & \text{otherwise} \end{cases} \end{aligned}$$

where the $+$ superscript denotes the positive part and the $-$ superscript denotes the negative part. Equation (2.18) is then updated using

$$\phi_{i,j}^{N+1} = \phi_{i,j}^N - \Delta t S_\epsilon(\phi_{i,j}^0) G(\phi_{i,j}^N). \tag{3.9}$$

It is shown in [33] that (3.9) is a consistent, monotone scheme of (2.21), which is known to converge to the unique viscosity solution of (2.21). If $\phi^0 > 0$ and

$G(\phi^0) < 0$, then [33] proved that $\phi \nearrow$ implies $G(\phi) \nearrow$. An extension of this can easily be deduced for $\phi^0 < 0$. If $\phi^0 < 0$ and $G(\phi^0) < 0$, then $\phi \searrow$ implies $G(\phi) \nearrow$. So, if $G(\phi^0) \leq 0$ and if Δt sufficiently small, then $G(\phi^N) \nearrow 0$ as $N \rightarrow \infty$. This follows from the fact that as long as $G(\phi^N) < 0$, then $\phi^N \leq \phi^{N+1}$ for $\phi^N \geq 0$ and $\phi^N \geq \phi^{N+1}$ for $\phi^N \leq 0$.

While (3.9) has the advantage of being a monotone scheme, it has the disadvantage of being only first order. We observed a significant improvement in our results by approximating the derivatives of ϕ by higher order schemes. In our tests, we used a second order ENO scheme upwinded in the proper direction (see [35]). As mentioned previously, we typically needed only one iteration per time step in order to meet our convergence criterion. We have also done tests where ϕ was initialized as $+1$ outside of a unit circle and -1 inside of a unit circle and our iteration converged successfully (see figure 7.34).

The stopping criterion for the iteration is

$$E = \frac{\sum_{|\phi^N_{i,j}|<\alpha} \mid \phi^{N+1}_{i,j} - \phi^N_{i,j} \mid}{M} < \Delta t \; h^2,$$

where $M \equiv$ number of grid points where $\mid \phi^N_{i,j} \mid < \alpha$. In our experiments we had $\Delta t = h/10$ and we used $\epsilon = h$ in the expression for S_ϵ.

3.6 Computation of Δt

The time step must obey the CFL conditions due to the convective terms. Restrictions due to stiff source terms (e.g. gravity and surface tension), and due to viscous terms must also be satisfied (see (6.3) of [27] and (61) of [10]):

$$\begin{aligned}
\Delta t_s &\equiv \sqrt{\frac{(\rho_c + \rho_b)B}{8\pi}} h^{3/2} \\
\Delta t_v &\equiv \min_{\Omega}((\frac{3}{14})\frac{\rho(Re)h^2}{\mu}) \\
\Delta t_c &\equiv \min_{\Omega}(\frac{h}{|\vec{u}|}) \\
\Delta t^{n+1} &= \frac{1}{2}\min(\Delta t_v, \Delta t_s, \Delta t_c)
\end{aligned}$$

CHAPTER 4

Axisymmetric Flow

4.1 Introducing Axisymmetric Flow

In axisymmetric flow, instead of our grid consisting of x and y coordinants, we replace them with r and z respectively. If our flow is assumed to be axisymmetric about the z axis, then we may approximate fully three dimensional problems using only two dimensions. In other words, we assume our fluid variables are independent of θ where the three independent variables in cylindrical coordinants are (r, θ, z). On axisymmetric grids we can model fully spherical bubbles and drops, so that we may compare with the toroidal bubbles in [25] (figure 7.16) or the colliding drops in [28] (figure 7.32). We will also model the capillary jet problem found in [10] (figure 7.35), the problem of a gas bubble rising to the surface of an air/water interface [9] (figure 7.36), and the problem of a water drop splashing down on a surface of water [29] (figure 7.41).

4.2 Changes to Two-Dimensional Algorithm

In axisymmetric flow, the divergence and laplacian operators depend on r. For example, the divergence free condition now becomes:

$$\vec{\nabla} \cdot \vec{u} = (ru)_r/r + v_z = 0. \tag{4.1}$$

The expression for the laplacian of a scalar is:

$$\Delta\phi = (r\phi_r)_r/r + \phi_{zz}.$$

The computation of the projection, the viscous terms, and the curvature are all effected by the above issues.

4.2.1 Axisymmetric Projection

In section 2.2, it was shown that any vector $\vec{V}$ can be uniquely decomposed into a divergence free vector $\vec{V}_d$ and the gradient of a scalar $\vec{\nabla}\psi/\rho$. In cylindrical coordinants $\vec{V}_d$ and $(\vec{V}_1, \vec{V}_2)$ have the form,

$$\vec{V}_d = (\Psi_z/r, -\Psi_r/r)$$
$$(\vec{V}_1, \vec{V}_2) = \int_\Omega \vec{V}_1 \cdot \vec{V}_2 \rho r dr dz.$$

The equation for Ψ (see eq. (2.8)) is now written as

$$-\vec{\nabla}(\frac{\rho}{r}\vec{\nabla}\Psi) = \vec{\nabla} \times (\rho\vec{V}). \tag{4.2}$$

We discretize the projection in a similar manner as that in section 3.4. In cylindrical coordinants, our discrete divergence has the form,

$$(\vec{\nabla}\cdot\vec{U})_{i+\frac{1}{2},j+\frac{1}{2}} \approx (D\vec{U})_{i+\frac{1}{2},j+\frac{1}{2}} \equiv$$

$$((ru)_{i+1,j+1} - (ru)_{i,j+1} + (ru)_{i+1,j} - (ru)_{i,j})/(2hr_{i+\frac{1}{2}})$$

$$+((rv)_{i+1,j+1} - (rv)_{i+1,j} + (rv)_{i,j+1} - (rv)_{i,j})/(2hr_{i+\frac{1}{2}}).$$

For the inner product we have:

$$(\vec{V}_1, \vec{V}_2)_\rho \equiv \sum_{i=0}^{M-1}\sum_{j=0}^{N-1}(\vec{V}_{1,ij}\cdot\vec{V}_{2,ij})\rho_{ij}r_{ij}.$$

We can write our discrete gradient and divergence free vector in the form,

$$\begin{aligned}
(\vec{\nabla}\Phi)_{i,j} \approx (\vec{G}\Phi)_{i,j} &\equiv ((G_x\Phi)_{i,j}, (G_y\Phi)_{i,j}) \\
(G_x\Phi)_{i,j} &\equiv (\Phi_{i+\frac{1}{2},j+\frac{1}{2}} - \Phi_{i-\frac{1}{2},j+\frac{1}{2}} + \Phi_{i+\frac{1}{2},j-\frac{1}{2}} - \Phi_{i-\frac{1}{2},j-\frac{1}{2}})/(2h) \\
(G_y\Phi)_{i,j} &\equiv (\Phi_{i+\frac{1}{2},j+\frac{1}{2}} - \Phi_{i+\frac{1}{2},j-\frac{1}{2}} + \Phi_{i-\frac{1}{2},j+\frac{1}{2}} - \Phi_{i-\frac{1}{2},j-\frac{1}{2}})/(2h)
\end{aligned}$$

$$\vec{V}_d \equiv (G_y\Psi/r, -G_x\Psi/r)$$

Finally, we solve a system of equations for Ψ using a formula that is similar to equation (3.7:

$$-G_x(\frac{\rho}{r}(G_x\Psi)) - G_y(\frac{\rho}{r}(G_y\Psi)) = G_x(\rho V_2) - G_y(\rho V_1) \qquad (4.3)$$

4.2.2 Divergence of the Stress Tensor in Axisymmetric Coordinants

In cylindrical coordinants (for axisymmetric flow), the stress tensor is as follows:

$$e^{rr} = u_r$$

$$e^{rz} = \frac{1}{2}(u_z + v_r)$$

$$e^{zz} = v_z$$

$$e^{\phi\phi} = u/r$$

The divergence of the stress tensor $(\vec{\nabla} \cdot (\mu e))$ has the following form:

$$(\vec{\nabla} \cdot \mu e)_1 = (r\mu e^{rr})_r/r + (\mu e^{rz})_z - \mu e^{\phi\phi}/r \tag{4.4}$$

$$(\vec{\nabla} \cdot \mu e)_2 = (r\mu e^{rz})_r/r + (\mu e^{zz})_z \tag{4.5}$$

We discretize the above equations using similar equations as that found in section 3.3. In equation (4.4), the term $e^{\phi\phi}/r$ can become large near $r = 0$. We rewrite equation (4.4) as,

$$(\vec{\nabla} \cdot \mu e)_1 = (\mu e^{rr})_r + \mu(e^{\phi\phi})_r + (\mu e^{rz})_z. \tag{4.6}$$

When we discretize equation (4.6), we need to evaluate u/r at $r = 0$. Since the normal component of the velocity is zero at the boundary, we have $u = 0$ at $r = 0$. So, we can use the limit of u/r at $r = 0$ which is u_r.

4.2.3 Computation of curvature in Axisymmetric Coordinants

As in equation (2.15), the curvature is written as,

$$\kappa(\phi) = \vec{\nabla} \cdot (\frac{\vec{\nabla}\phi}{|\vec{\nabla}\phi|}). \tag{4.7}$$

We use equation (4.1) to express the gradient of a vector in cylindrical coordinants,

$$\kappa(\phi) = \frac{(r\phi_r / \mid \vec{\nabla}\phi \mid)_r}{r} + (\phi_z / \mid \vec{\nabla}\phi \mid)_z. \tag{4.8}$$

Equation 4.8 is discretized in similar fashion as the viscosity. The curvature is approximated as follows:

$$\begin{aligned}
(\phi_r)_{i+\frac{1}{2},j+\frac{1}{2}} &= (\phi_{i+1,j+1} + \phi_{i+1,j} - \phi_{i,j+1} - \phi_{i,j})/(2h) \\
(\phi_z)_{i+\frac{1}{2},j+\frac{1}{2}} &= (\phi_{i+1,j+1} + \phi_{i,j+1} - \phi_{i+1,j} - \phi_{i,j})/(2h) \\
\mid \vec{\nabla}\phi \mid_{i+\frac{1}{2},j+\frac{1}{2}} &= \sqrt{(\phi_r)^2_{i+\frac{1}{2},j+\frac{1}{2}} + (\phi_z)^2_{i+\frac{1}{2},j+\frac{1}{2}}} \\
c_{i+\frac{1}{2},j+\frac{1}{2}} &\equiv r_{i+\frac{1}{2}}(\phi_r)_{i+\frac{1}{2},j+\frac{1}{2}} / \mid \vec{\nabla}\phi \mid_{i+\frac{1}{2},j+\frac{1}{2}} \\
d_{i+\frac{1}{2},j+\frac{1}{2}} &\equiv (\phi_z)_{i+\frac{1}{2},j+\frac{1}{2}} / \mid \vec{\nabla}\phi \mid_{i+\frac{1}{2},j+\frac{1}{2}} \\
\kappa(\phi)_{i,j} &= (c_{i+\frac{1}{2},j+\frac{1}{2}} + c_{i+\frac{1}{2},j-\frac{1}{2}} - c_{i-\frac{1}{2},j+\frac{1}{2}} - c_{i-\frac{1}{2},j-\frac{1}{2}})/(2r_i h) \\
&\quad +(d_{i+\frac{1}{2},j+\frac{1}{2}} + d_{i-\frac{1}{2},j+\frac{1}{2}} - d_{i+\frac{1}{2},j-\frac{1}{2}} - d_{i-\frac{1}{2},j-\frac{1}{2}})/(2h)
\end{aligned}$$

CHAPTER 5

Three Fluid Flow

5.1 Motivation for Multi-Fluid Flow

Many flows consist of more than two immiscible fluids. Examples include stratified flow [38] (figure 7.45) and flow consisting of air, oil, and water (such as flow through pipes [1]). We have computed flows of gas bubbles rising up to a water/oil interface (figure 7.43). There are also many problems consisting of two fluids where one would like to study the motion of multiple interfaces. An illustration of this is the case where one would like to study the subsequent motion of the point of impact of merging bubbles and drops (figure 7.32). Also, when a gas bubble rises to the surface of an air/water interface [9] (figure 7.40), or when a water drop hits an air/water interface [29] (figure 7.42), one would like to study the motion of the bubble or drop as it penetrates the interface.

The main complication with multi-fluid flow is the computation of the flow at "triple points". A triple point is a point where two interfaces intersect (in three fluid flow, a point where all three fluids touch). An example of this occurring

would be a gas bubble rising in water which intersects a water/oil interface (see figure 7.43). In [7], a paper on multiple interfaces whose motion is determined by mean curvature, level sets were used to automatically resolve the intersection of interfaces without any extra work needed for reconnecting or separating interfaces. We will use ideas similar to that in [7] for applying level sets to multi-fluid flow.

5.2 Changes for Three-Fluid Flow

For each fluid i, we will introduce a level set function ϕ_i which is used to capture the interface between fluid i and all the other fluids. Each ϕ_i will be advected and re-initialized similar to that of ϕ which was used for two-fluid flow. Special care must be taken when computing density and surface tension for multi-fluid flow. One must be careful to avoid cases where all the ϕ_i are bigger than zero at some grid cell ("void"). At all points in the domain, one and only one ϕ_i should be less than zero. In [7], where each front was advected by a different velocity determined by its respective mean curvature, a special procedure had to be performed every time step in order to prevent voids from forming in the domain. For incompressible applications, where each ϕ_i is advected with the same velocity, the problem of voids forming should not be an issue, but the problem still persists on a lesser scale. In certain cases where corners in the flow occur, the re-initialization step tends to smooth the corners, thus possibly producing an area where all ϕ_i are greater than zero. In [7], the ϕ_i were modified with the following equation after each time step;

thus eliminating voids and insuring the proper motion of triple points:

$$\phi_i = \frac{1}{2}(\phi_i - \min_{i \neq j} \phi_j). \tag{5.1}$$

We also use equation (5.1), but we do not update the existing ϕ_i with the new values. Instead we store the values from the above equation in the quantities d_i which are to be used when computing density and surface tension. We do not update the ϕ_i for two reasons:

1. As opposed to flow by mean curvature, our void areas remain small.

2. Equation (5.1) does not preserve the distance property at triple junctions, thus distorting the solution and also giving rise to more iterations in the re-initialization step.

Using figure 7.44, we can compare our "multi-level set" formulation for a gas bubble rising through water with the single level set solution (fig. 7.11).

5.2.1 Computing Density in Multi-Fluid Flow

We compute the temporary variables d_i using equation 5.1:

$$d_i = \frac{1}{2}(\phi_i - \min_{i \neq j} \phi_j). \tag{5.2}$$

The density is computed similarly to that in equation (2.14),

$$\rho(\phi_1, \ldots, \phi_n) = \rho(d_1, \ldots, d_n) = \frac{\sum_{i=1}^{n} \rho_i H_\alpha(d_i)}{\sum_{i=1}^{n} H_\alpha(d_i)}.$$

The Heaviside function H_α is determined by equation (2.13). The denominator is assured of being positive because of how the d_i are computed in equation (5.2).

5.2.2 Computing Surface Tension in Multi-Fluid Flow

There are two ways to compute surface tension when capturing multiple interfaces. For the first way, we assume that interfaces "burst" immediately on contact with another interface of the same fluid. For the second way, we assume that interfaces never "burst" (rupture). To illustrate this, we use the merging of two water drops as an example (see figures 7.31 and 7.32). For both cases, as for the computation of density, we first compute the values d_i from equation (5.2). These values will be used in determining the curvature and delta function.

5.2.2.1 Computing Surface Tension with Rupture

We describe the computation of surface tension, where we assume the interface will rupture on contact with another interface of the same fluid (figure 7.31). We compute the surface tension at fluid interface d_{ij} if the following conditions are met:

- d_i and d_j are less than all other d_k.
- $\mid d_i \mid$ and $\mid d_j \mid$ are less than α (interface thickness).

- d_i and d_j represent different fluids.

If the above criteria are met, then we compute the surface tension at interface d_{ij} using the formula,

$$\vec{s}_{ij} = \frac{1}{2}(B_{ij}\kappa(d_i)\delta(d_i)\vec{\nabla}d_i + B_{ij}\kappa(d_j)\delta(d_j)\vec{\nabla}d_j). \tag{5.3}$$

As for two-fluid flow, we do not explicitly compute equation (5.3). Instead we compute the above equation as part of the projection step in our "Heaviside" formulation (see equation (2.17)).

5.2.2.2 Computing Surface Tension without Rupture

We describe the computation of surface tension, where we assume the interface will not rupture on contact with another interface of the same fluid (figure 7.32). We will assume the simple case of the problem where two water drops collide. There are three level set functions:

ϕ_1 Negative in the top drop and positive elsewhere.

ϕ_2 Negative in the air and positive in the drops.

ϕ_3 Negative in the bottom drop and positive elsewhere.

We use equation (5.2) to initialize the d_i. Let B_{aw} represent the Bond coefficient for an air/water interface. Since surface tension acts to keep the drops spherical, we choose to use only d_1 and d_3 for computing surface tension. Since we assume

that the collision of the two drops will not rupture the interface, we compute the surface tension at the point of collision (water/water interface) exactly the same as at an air/water interface. So, we use the following formula for computing surface tension:

$$\vec{s} = B_{aw}\kappa(d_1)\delta(d_1)\vec{\nabla}d_1 + B_{aw}\kappa(d_3)\delta(d_3)\vec{\nabla}d_3). \tag{5.4}$$

As for the ruptured case, we do not explicitly compute equation (5.4). Instead we compute the above equation as part of the projection step in our "Heaviside" formulation (see equation (2.17)).

5.2.2.3 Discrepancies When Computing Surface Tension With Rupture

We again study the case of two drops merging. In figure 7.31, we average the contribution at interface d_{ij} using d_i and d_j. Unfortunately this may not be very accurate as the drops get closer. The distance function representing air (d_2) has almost zero curvature near the middle of the two drops, which is an inaccurate representation of the curvature if the drops are near each other. For example, at a cell near drop d_1, and also near the midpoint of the two drops, we compute the surface tension by averaging the contribution from d_1 (curvature about one - ok) with that of d_2 (curvature near zero - not ok). If we know that the surface tension is acting to keep the drops spherical (as in the case where we do not assume

rupture - eq. (5.4)), we should not average the two contributions, but instead just use the contribution from d_1 which has the proper representation for curvature. We modify equation 5.3 in a similar fashion as equation 5.4. If we assume all the criteria for the "burst" case are met, then we use the following equation for our drop merge case (see figure 7.33):

$$\vec{s}_{ij} = \begin{cases} B_{aw}\kappa(d_1)\delta(d_1)\vec{\nabla}d_1 & \text{if } \mid d_1 \mid \text{and } \mid d_2 \mid < \mid d_3 \mid \\ B_{aw}\kappa(d_3)\delta(d_3)\vec{\nabla}d_3 & \text{if } \mid d_3 \mid \text{and } \mid d_2 \mid < \mid d_1 \mid \\ 0 & \text{otherwise} \end{cases} \tag{5.5}$$

CHAPTER 6

Analysis of Results for 2D, 3D axisymmetric, and Three Fluid Flow

Our experiments simulate the flow of air bubbles and water drops. We will assume the flow is symmetric about the axis $x = 0$ ($r = 0$). The key parameters are density ratio ρ_c/ρ_b, viscosity ratio μ_c/μ_b, Bond number $B = 4\rho_c g R^2/\sigma$, and Reynolds number $Re = (2R)^{\frac{3}{2}}\sqrt{g}\rho_c/\mu_c$. Using the tables in [4], we have $\rho_{air} = 1.226 \times 10^{-3}\text{g/cm}^3$, $\rho_{water} = 1.000\text{g/cm}^3$, $\mu_{air} = 1.78 \times 10^{-4}\text{g/(cm sec)}$, $\mu_{water} = 1.137 \times 10^{-2}\text{g/(cm sec)}$, $g = 980$ cm/sec^2, and $\sigma = 72.8$ dynes/cm. These physical constants are used in determining the above parameters.

6.1 Convergence study

6.1.1 2D Rising Gas Bubbles

We consider two 2D rising bubble problems. The first problem is a bubble rising with medium range Reynolds number and small surface tension. For the second problem, we consider a bubble rising with low Reynolds number and high surface tension. We let the second bubble rise to a steady state.

For the first test, we have $B = 200.0$, $Re = 100.0$, $\rho_c/\rho_b = 1000.0$ and $\mu_c/\mu_b = 100.0$. Grids of 36×36,72×72, and 144×144 are used. The number of time steps for each of the respective grids is 734, 1467, and 2934. We compare results up to time $t = 4.4$ (see figures 7.10 and 7.11). We compute the relative error between successive grids as follows:

$$E_{h,2h} \equiv \sum_{t=0.0}^{4.4} \mid f_h - f_{2h} \mid .$$

Table 6.1 contains values for the position and velocity of the center of the bubble. Table 6.1 also contains relative errors for minor axis size and area. Figure 7.12 compares the position of the center of the bubble.

For the second test, we have $B = 0.40$, $Re = 5.0$,$\rho_c/\rho_b = 40.0$, and $\mu_c/\mu_b = 500$. Grids of 16×32,32×64, and 64×128 are used (see figure 7.5). The bubble reaches a steady state where its oblate shape is the expected result (see [36], p. 31). The area, velocity, and minor axis are each plotted with respect to time (see figures 7.6,7.7, and 7.8).

6.1.2 3D Axisymmetric Gas Bubble - Convergence at Singularity

We would like to investigate the convergence properties of a 3D axisymmetric gas bubble as it evolves through its first break up. We will study a gas bubble with $Re = 200$ and $B = 200$. The motion was computed on grids of size 50×50, 100×100, and 200×200. In figure 7.18, we compare results at the time of pinch off

	$E_{h,2h}$	$E_{2h,4h}$	Order
position	0.01	0.05	2.3
velocity	0.02	0.07	1.8
area	0.02	0.16	3.0
minor axis	0.04	0.12	1.6

Table 6.1: 2D Convergence study: $t = 4.4$

on the two finest grids. In figure 7.19, we compare the mass conservation properties. The time of break up on the three grids are 1.85, 1.55, and 1.61 respectively. The minor axis sizes at $t = 1.5$ were 0.37, 0.09, and 0.06 respectively. From figure 7.19, we see that more mass is conserved as the grid is refined. On the finest grid, we see that break-up occurs slightly offset from center; a tiny bubble, unresolved on the coarser grids, appears between the two main broken parts of the bubble. While more mass is conserved as the grid is refined, we see that even on the finest grid, mass is lost at a steady rate after break up. This is due to the inability of the algorithm to resolve on our finest grid either the tiny bubble or the upper tips of the two main broken pieces.

6.2 Analysis of Gas Bubble Problems

6.2.1 Validation of 3D Rising Gas Bubble

As with the 2D case in section 6.1.1, a gas bubble rising with low Reynolds number, and a substantial amount of surface tension, will reach a steady state after a finite amount of time. The resultant shape and velocity of the bubble depends on the Reynolds number $2\rho UR/\mu$, Weber number $2\rho U^2R/\sigma$, and Froude number $U^2/(2Rg)$. One can also represent the flow using the drag coefficient $C_d = 4/(3Fr)$ instead of the Froude number. In [8, 19], physical experiments were done to determine the resultant steady shape and velocity. They initialized their apparatus with values for the Morton number $g\mu^4/(\rho\sigma^3)$ and Eotvos number (similar to Bond number) $4gR^2\rho/\sigma$. After the experiment was finished, they used their measured values of U in order to determine Re, We, and C_d. The resultant steady shapes ranged from almost spherical to cap shaped. Numerical experiments were done in [34] using equations for incompressible steady state flow. In our computations, we will compute the evolution of a 3D axisymmetric gas bubble as it rises and reaches its characteristic steady shape. In figure 7.9, we have results for $M = 0.056$ and $E0 = 39.8$. For $t > 3.0$, the computed dimensionless velocity varied between 0.82 and 0.86. The dimensionless major axis size was 1.26. Finally, our computed values for Re, We, and C_d were 16.8, 10.6, and 5.01 respectively. In [8] the following formula was used to predict the steady rise speed,

$$u = \frac{2}{3}\sqrt{r_c g}.$$

For our problem, the predicted dimensionless rise speed is 0.86 which compares well with our computed steady rise speed of about 0.84. We also have good agreement with [34] (figure 2), [8] (figure 8), and with [19] (fig. 1a) for the resultant shape of our bubble.

6.2.2 Effects of Surface Tension

We study the effects of adding surface tension to the rising bubble problem where $Re = 100.0$. In figure 7.13, we compare the results with Bond number of 200.0 (a) to that of $Bd = 25.0$ (b). The change in shape is similar to that found in [25] (experiments using the boundary integral method) where the bubble skirts become more thin and the indentation at the bottom flattens out.

6.2.3 Effects for varying Reynolds Number

6.2.3.1 Computation of 2D gas bubble for low,medium, and high Re

We compare the results of figure 7.14 ($Re = 10.0$), figure 7.11 ($Re = 100.0$), and figure 7.15 ($Re = 1000.0$). The change in shape due to low Reynolds number is similar to that found in the experiments of [8] (see figure 3 of [8]). The results for high Reynolds number flow compares well to the results in [3]. In [3], the authors

computed the solution until pinch off ($t = 4.0$), of an inviscid gas bubble. They used both the boundary integral method and the point vortex method and got almost identical results using those methods. The fact that our results using an Eulerian grid are also very close to the above Lagrangian schemes validates our code for high Reynolds number and for steep density ratios.

6.2.3.2 Convergence as Re approaches ∞ for 3D gas bubble

In [25], computations using the boundary integral method were done for an inviscid 3D axisymmetric gas bubble with slight surface tension. We will compare with the case for Bond number of 200.0. We ran successively higher Reynolds number cases until finally we ran a case with $Re = \infty$. Our density ratio is 1000 to 1 and our viscosity ratio is 100 to 1. Our thickness parameter α is $3h/2$. In table 6.2 and figure 7.17, we show that the minor axis size and bubble shape converges as Re approaches ∞. For $Re = \infty$ our results (see 7.16) are remarkably similar to that of [25] (figure 2a), including the time that the bubble begins to break up. The fact that we can compare with the boundary integral method demonstrates that, for this particular problem, we do not have added numerical viscosity. We also note that in figure 7.16, the solution is fully resolved up to $t = 1.30$. The solution was computed with a mesh size of 240×240 ($h = 0.025$) and a thickness of $\alpha = 3h$. There are no significant changes in bubble shape, rise speed, or minor axis size when the mesh is refined and/or the interfacial thickness (α) is enlarged.

Re	Minor Axis
100	0.38
200	0.24
400	0.18
800	0.17
∞	0.17

Table 6.2: Convergence of shape of a 3D gas bubble in the inviscid limit. $t = 1.4$, $\alpha = 3h/2$

6.2.4 Effects of Different Density Ratios

We compare the results of figure 7.11 ($\rho_c/\rho_b = 1000.0$) to that of figure 7.20 ($\rho_c/\rho_b = 5.0$). The shape of the bubbles are similar except that the skirts on the low density-ratio bubble are allowed to grow longer than those on the high density-ratio bubble. The pinch off time is 4.5 for the high density-ratio bubble and 5.6 for the low density ratio bubble. We also compare the above results to that of figure 7.21. For slight density ratios, the skirts of the bubble begin to roll up (see [2]). In figure 7.22, we plot the velocity of the bubble for different density ratios.

6.2.5 Gas Bubble bursting at surface

As a gas bubble rises to the surface of an air/water interface, the buoyancy force due to gravity interacts with surface tension effects at the interface, thus causing the bubble to burst, and emitting a jet of water. According to [9], studying and minimizing the burst effects can minimize the cell death rate in a bioreactor. We will run computations on problems similar to that computed in [9] which used the boundary integral method. We non-dimensionalize the problem by normalizing the surface tension coefficient to one and the gravitational coefficient to the Bond (Eotvos) number (see [9]). The calculations will be for inviscid flow. In figure 7.36, we observe the expected jet of water. As in other calculations with change in topology, we are able to automatically compute the break up of the water jet as it falls back to the surface. In figure 7.37, we compare with [9] for $E0 = 0.3$. We have similar shapes and velocity profiles (see figure 7.38) except that the jet in [9] (fig. 4a) is taller and their velocity profile is less oscillatory. An advantage of the boundary integral method, for inviscid problems without complex topology, is the ability to place many more points on the interface than Eulerian schemes. Also, while we enforce solid wall boundary conditions, the boundary integral scheme can approximate flow in an infinite domain. In figure 7.39, we run the same problem again, except that we demonstrate the advantages of our level set scheme by starting with our gas bubble fully submerged. We have similar results as with the "pre-burst" case except that a small air bubble is entrained. Finally, we run

the problem with $E0 = 0.3$ using multiple level set functions. Thus, we are able to compute the flow of the air bubble as it bursts out of the water (see figure 7.40). The results for the multiple interface version are similar to the other results except that the jet emitted is shorter than in the "pre-burst" case.

6.3 Analysis of Water Drop Problems

6.3.1 Surface tension validation; Surface Tension Driven Oscillations

A cylindrical or spherical drop of liquid, which has a slightly perturbed circular cross section, will display oscillatory motion in the presence of surface tension and in the absence of gravity. In [23], equations are derived for the predicted frequency of oscillation for the 2D drop (p.472, eq. (8)) and for the 3D drop (p.475, eq. (11)). These equation are valid for small perturbations in inviscid flow. In figures 7.23 (2d case) and 7.24 (3d case) we compute the above motion and compare our computed frequencies with that of [23]. We have $Re = 20.0$, $B = 0.5$, $\rho_c/\rho_b = 0.01$, $\mu_c/\mu_b = 0.01$, $a = 1.0$, $A = 0.06$, $s = 2$, and $\Delta x = 0.07$. "A" is the amplitude of the initial perturbation, "s" is the disturbance type and "a" is the base radius of the drop. For the 2D case, our computed period of 1.92 agrees closely with the result predicted by the formula $2\pi/\sigma$ (1.81) where $\sigma^2 = 6/B$. For the 3D case, we also get close agreement. The computed period is 1.71 and the expected result is

1.57. Any discrepancies in our results should be due to the presence of viscosity and also due to our size of the initial amplitude.

6.3.2 Analysis of falling drop hitting boundary

We study the flow of a falling water drop hitting a solid wall boundary (see [16]). We refer the reader to figures 7.25 and 7.26. When the required surface tension is added, we get the expected circular shape as the drop is in mid-flight. We compare our results ($R = 0.125cm$, $B = 0.00125$, $Re = 10.0$) to that of [26] ($R = 0.140cm$). Our results are similar to that of [26]. The added surface tension prevents the drop from "flattening out" near the lower boundary. Figure 7.27 displays the position of the drop versus time. The average acceleration was 0.95 (5% error).

6.3.3 Analysis of head-on collision of two drops

As stated in [28], drop collisions can be classified into four categories:

- bouncing collision; drops separate after colliding, retaining their original "identity".
- coalescence collision; drops collide to form as one drop.
- separation collision; drops temporarily become one but then break up again.

- shattering collisions; upon impact, drops break up into many smaller drops.

The motion of drops is important in a number of applications such as combustion of fuel sprays, spray painting, coating processes, and rain drops. We will study the collision of two equal sized drops in the absence of gravitational forces. The two drops are each accelerated at each other with a body force of 0.5. After time $t = 2.0$, when the drops are traveling with a dimensionless velocity of about 1.0, the force is turned off.

In figure 7.28, we have the collision of two 2D drops. The drops are allowed to coalesce into one large drop. Mass is conserved throughout the collision (see figure 7.29). After the collision, the combined drop undergoes oscillation due to the surface tension forces ($Re = 20.0$, $Bd = 1.33$). As with bubble pinch-off above, our level set formulation enables us to merge the two drops without any extra programming.

In figure 7.30, we have the collision of two 3D drops ($Re = 20.0$,$Bd = 12$). As in the 2D case, the drops are allowed to coalesce. We get similar profiles as in [28] (fig. 17) where they manually merged their drops. In figure 7.32, we use multiple level set functions to compute the motion of each drop separately. The surface tension is computed using equation 5.4 for the "non-ruptured" case. In this case we get a "bouncing collision" where the drops separate after colliding. Our results here can be compared to those in [28] (fig. 9). Finally, in figure 7.33, we use multiple level set functions again. This time, we compute the surface tension

using equation 5.5 for the "ruptured" case. We get a "separation collision" for this case, where the drops eventually separate again, following initial coalescence (see [28], fig. 9).

6.3.4 Capillary Jet

We start our problem with a vertical cylindrical column of liquid. We assume the flow is inviscid and we ignore gravitational effects. In [32], theory was developed for the evolution of this column, driven by surface tension forces, in the presence of a small radial perturbation in the jet. After a finite amount of time, the perturbation grows until parts of the jet contracts and eventually breaks up into detached drops (see figure 7.35). Equations were developed in [32] that predicted the time when the jet is supposed to break up. The equation depended only on the perturbation wave number k. We will run with parameters similar to that found in [22]. The computations in [22] were done using a volume tracking algorithm. We non-dimensionalize our parameters so that our dimensionless initial radius is one, and the dimensionless surface tension is $1/2$. We set $k = 0.3$ and our initial perturbation amplitude $\epsilon = 0.05$. The expected break up time is $t_b = 25.92$ and our observed break up time was about 20.5. Our results (see figure 7.35) are in good agreement with the results in [22] (see fig. 13). The results here demonstrate yet again, the ability of our algorithm to effortlessly and accurately compute through pinch-off with relatively low resolution. The results also demonstrate the ability

of our scheme to compute flows heavily influenced by surface tension forces.

6.3.5 water drop splashing water surface

As a high speed water drop hits an air/water interface, a "splash" occurs causing water to be displaced to the sides of the drop. In [29], many inviscid computations were done using the boundary integral method and compared with experimental results. We will non-dimensionalize our parameters in a similar fashion as in [29]. Since we are computing flow with air and water, values for σ,ρ, and g are fixed. One must specify the impact velocity U and the drop radius R. The dimensionless surface tension force depends on the Weber number $We = 2\rho U^2 R/\sigma$ and the dimensionless gravitational force depends on the Froude number $Fr = U^2/(2gR)$. Our dimensionless impact velocity is 10 and our dimensionless drop radius is 1. We initialize our problem with the drop exactly one drop radii above the surface. The gravitational force is initialized as 50 and reduced back to the specified force after $t = 0.2$ (time of impact). In figure 7.41, we compute the splash profile for $U = 7.6$m/s and $R = 1$mm. In figure 7.42, we compute the same problem except that we use multiple level set functions. Thus, we are able to compute the shape of the falling drop as it combines with the other water.

CHAPTER 7

Conclusion

In summary, we have designed a formally second order accurate algorithm for tracking the interface(s) of multiple incompressible fluids. The interface remains sharp ($\rho_c/\rho_b = 1000$) without ever having to explicitly find the front. As in [36], the front is given a finite thickness $O(h)$ which does not change in time; hence there is no added numerical diffusion. Since we solve a PDE for ϕ (insured to be a smooth distance function for all time) instead of for ρ, relatively coarse grids can be used. The algorithm is easy to code since the initial Eulerian grid remains the same throughout simulation. There is no extra code needed for handling merging, break-up, dilation, or contraction of the interface. Since the algorithm does not have to explicitly find the interface, the code can be easily generalized to three dimensions. Furthermore, surface tension is incorporated as a body force term which is easy to compute. Because of the special treatment of the convective terms, the algorithm can accurately handle high Reynolds number flow. Finally, we can generalize our study of bubbles and drops to many different incompressible ("low-speed") flow applications requiring complex interfacial structures, surface tension, and large density ratios. Applications include coating processes, ink-jet printers (drop dynamics), mold-filling and solidification, fuel sprays in internal

combustion engines, liquid extraction processes, and free-surface flows, to name a few.

Bibliography

[1] Acikgoz, M., Franca, F., and Lahey Jr., R.T., *An Experimental Study of Three-Phase Flow Regimes*, Int. J. Multiphase Flow, 18 (3), 327-336 (1992).

[2] Anderson, C.R., *A Vortex Method for Flows with Slight Density Variations*, J. Comp. Phys., 61, 3 (1985).

[3] Baker, G.R. and Moore, D.W., *The rise and distortion of a two-dimensional gas bubble in an inviscid liquid*, Phys. Fluids A 1 (9), pp. 1451-1459, (1989).

[4] Batchelor, G.K., *An Introduction to Fluid Dynamics*, Cambridge University Press, 1967.

[5] Bell, J.B., Colella, P. and Glaz, H.M., *A Second-Order Projection Method for the Incompressible Navier-Stokes Equations*, J. Comp. Phys., 85, pp. 257-283 (1989).

[6] John B. Bell and Daniel L. Marcus, *A Second-Order Projection Method For Variable-Density Flows*, J. Comp. Phys., 101, pp. 334-348, (1992).

[7] Bence, J., *Motion of Multiple Junctions: A Level Set Approach*, UCLA Ph.d thesis, submitted June 1993.

[8] Bhaga, D. and Weber, M.E., *Bubbles in viscous liquids: shapes, wakes and velocities*, J. Fluid Mech., 105, 61 (1981).

[9] Boulton-Stone, J.M. and Blake, J.R., *Gas Bubbles Bursting at a Free Surface*, J. Fluid Mech., 254, 437 (1993).

[10] Brackbill, J.U., Kothe, D.B., and Zemach, C., *A Continuum Method for Modeling Surface Tension*, J. Comp. Phys., 100, pp. 335-353, (1992).

[11] Chang, Y.C., Hou, T.Y., Merriman, B. and Osher, S., *A Level Set Formulation of Eulerian Interface Capturing Methods for Incompressible Fluid Flows* , preprint (1994).

[12] Chen, T.J. and Cooke, C.H., *On The Riemann Problem For Liquid Or Gas/Liquid Media*, Dept. of Mathematics and Statistics Old Dominion University, (1991).

[13] Chopp, D.L., *Computing Minimal Surfaces Via Level Set Curvature Flow*, Ph.d. thesis, Lawrence Berkeley Laboratory and Department of Mathematics, University of California Berkeley (1991).

[14] Chorin, A.J., *Numerical Solution of the Navier-Stokes Equations*, Math. Comput., 22, 745 (1968).

[15] Fatemi, E., *Modified Volume of Fluid Method for Calculation of Free-Surface Viscous Flows*, submitted to J. Comp. Phys., (1993).

[16] Fukai, J., Zhao, Z., Poulikakos, D., Megaridis, C.M., and Miyatake, O., *Modeling of the deformation of a liquid droplet impinging upon a flat surface*, Phys. Fluids A, 5 (11), pp. 2588-2599, (1993).

[17] Godunov, S.K., (1959), Mat Sb. 47, 271 (in Russian). Also in USJPRS translations 7226, (1960).

[18] Hirt, C.W. and Nichols, B.D., *Volume of Fluid (VOF) Method for the Dynamics of Free Boundaries*, J. Comp. Phys., 39, pp. 201-225, (1981).

[19] Hnat, J.G. and Buckmaster, J.D., *Spherical Cap Bubbles and Skirt Formation*, Phys. Fluids A, 19 (2), pp. 182-194, (1976).

[20] J. Van Kan, *A second-order accurate pressure-correction scheme for viscous incompressible flow*, SIAM J. Sci. Statist. Comput., 7, 870 (1986).

[21] Kim, J. and Moin, P., *Application of a fractional-step method to incompressible Navier-Stokes equations*, J. Comp. Phys., 59, 308 (1985).

[22] Kothe, D.B., Mjolsness, R.C., and Torrey, M.D., *RIPPLE: A Computer Program for Incompressible Flows with Free Surfaces*, Los Alamos National Laboratory Report, LA-12007-MS (1991).

[23] Lamb, H., *Hydrodynamics*, Dover Publications, 1945.

[24] LeVeque, R.J. and Li, Z., *The Immersed Interface Method for Elliptic Equations with Discontinuous Coefficients and Singular Sources*, Technical Report

92-12, Dept. of Appl. Math., Univ. of Washington (1992).

[25] Lundgren, T.S. and Mansour, N.N., *Vortex ring bubbles*, J. Fluid Mech., 224, 177 (1991).

[26] McDonald, J.E., *The Shape of Raindrops*, Scientific American,190:18,64-8, February (1954).

[27] Mulder, W., Osher, S., and Sethian, J.A., *Computing Interface Motion In Compressible Gas Dynamics*, J. Comp. Phys., 100, 209 (1992).

[28] Nobari, M.R., Jan, Y.J., and Tryggvason, G., *Head-On Collision of Drops-A Numerical Investigation*, NASA Technical Memorandum 106394, (1993).

[29] Oguz, H.N. and Prosperetti, A., *Bubble Entrainment by the Impact of Drops on Liquid Surfaces*, J. Fluid Mech., 219, 143 (1990).

[30] Osher, S. and Sethian, J.A., *Fronts Propagating with Curvature-Dependent Speed: Algorithms Based on Hamilton-Jacobi Formulations*, J. Comp. Phys., 79,1, pp. 12-49, (1988).

[31] Peskin, C.S., *Numerical analysis of blood flow in the heart*, J. Comp. Phys., 25, 220 (1977).

[32] Lord Rayleigh, *On the Instability of Jets*, Proc. London Math. Soc. 10, 4 (1878).

[33] Rouy, E. and Tourin, A., *A Viscosity Solutions Approach to Shape-From-Shading*, SIAM J. Numer. Anal., Vol. 29, No. 3, pp. 867-884, June 1992.

[34] Ryskin, G. and Leal, L.G., *Numerical Solution of Free-Boundary Problems in Fluid Mechanics. Part 2. Buoyancy-Driven Motion of a Gas Bubble Through a Quiescent Liquid*, J. Fluid Mech., 148, 19 (1984).

[35] Shu, C.W. and Osher,S., *Efficient Implementation of Essentially Non-Oscillatory Shock Capturing Schemes, II*, J. Comp. Phys., 83, pp. 32-78, (1989).

[36] Unverdi, S.O. and Tryggvason, G., *A Front-Tracking Method for Viscous, Incompressible, Multi-fluid Flows*, J. Comp. Phys., 100, pp. 25-37, (1992).

[37] B. Van Leer, *Multidimensional explicit difference schemes for Hyperbolic Conservation Laws*, Computing Methods in Applied Sciences and Engineering, VI, p. 493 (Elsevier Science, Amsterdam, 1984).

[38] Voropayev, S.I. and Afanasyev, Y.D., *Experiments on the Evolution of Gravitational Instability of an Overturned, Initially Stably Stratified Fluid*, Phys. Fluids A, 5 (10), 2461-2466 (1993).

[39] Walters, J.K. and Davidson, J.F., J. Fluid Mech., 12, 408 (1962).

[40] Woodward, P. and Colella, P., J. Comp. Phys., 54, 115 (1984).

[41] Zhu, J. and Sethian, J., *Projection Methods Coupled to Level Set Interface Techniques*, J. Comp. Phys., 102, pp. 128-138 (1992).

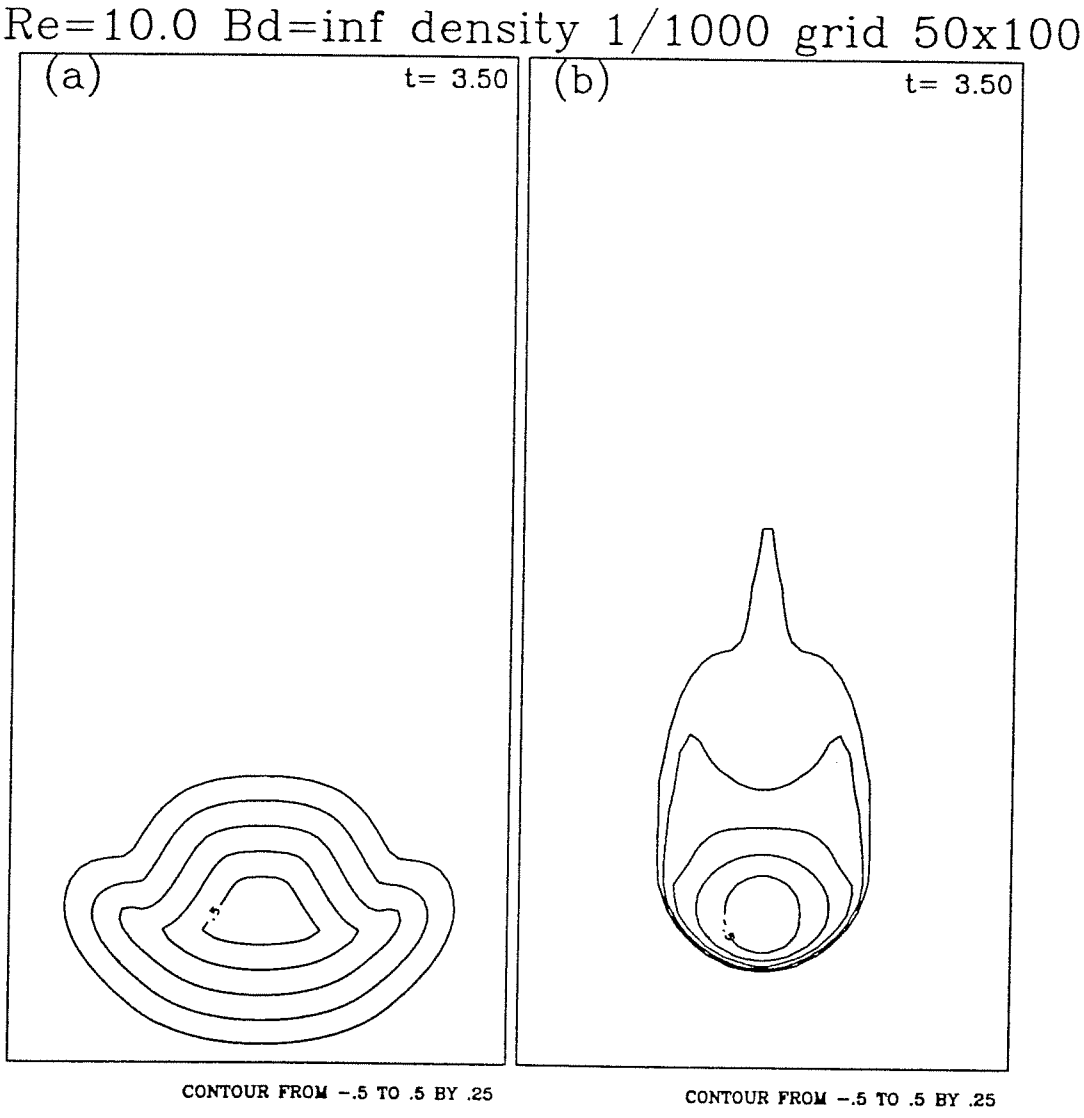

Figure 7.1: Level sets of a large water drop (a) reinit. (b) no reinit.

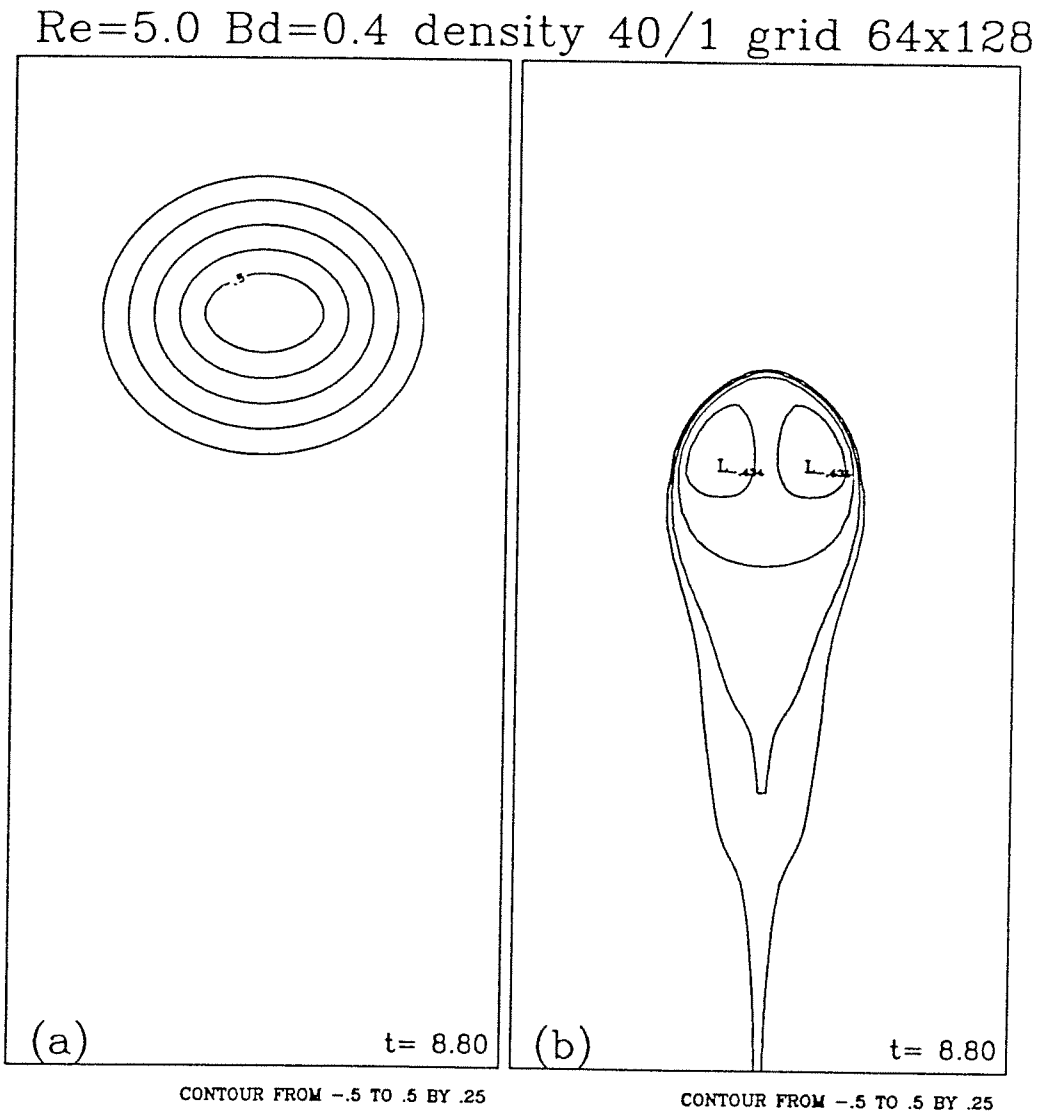

Figure 7.2: Level sets of rising bubble (a) reinit. (b) no reinit.

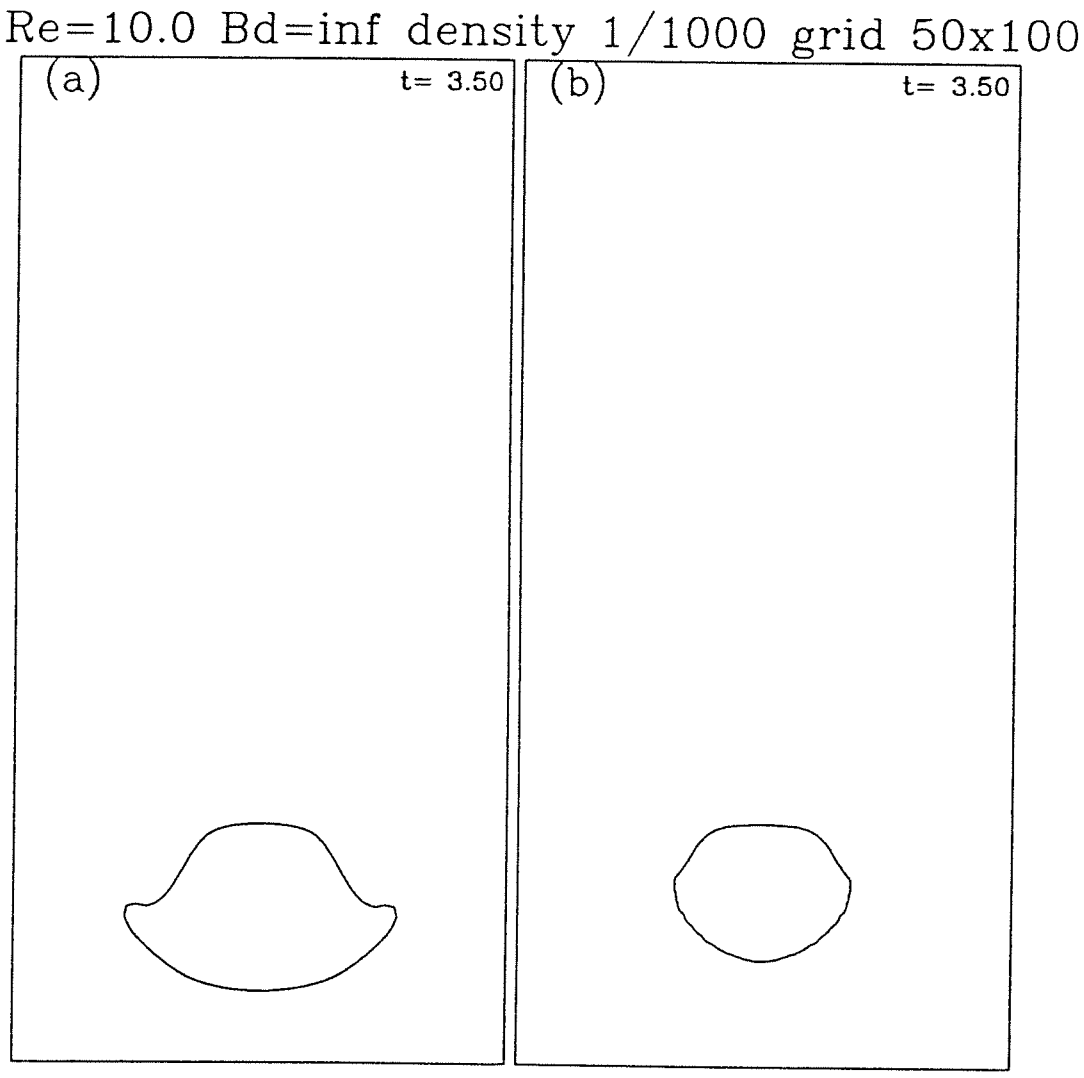

Figure 7.3: Without surface tension, large drop should deform as it hits the base (a) reinit. (b) no reinit.

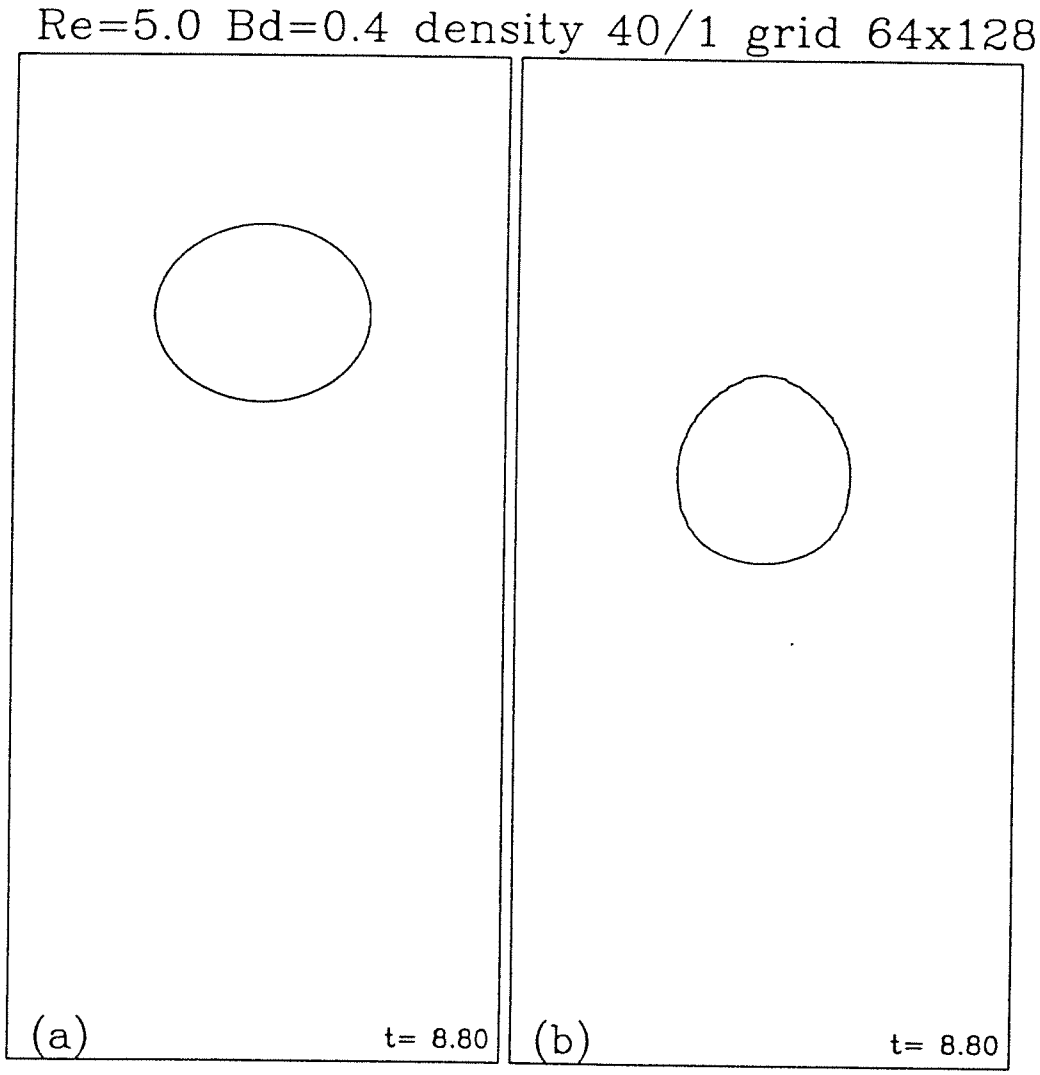

Figure 7.4: With large surface tension, bubble should reach ellipsoidal steady state (a) reinit. (b) no reinit.

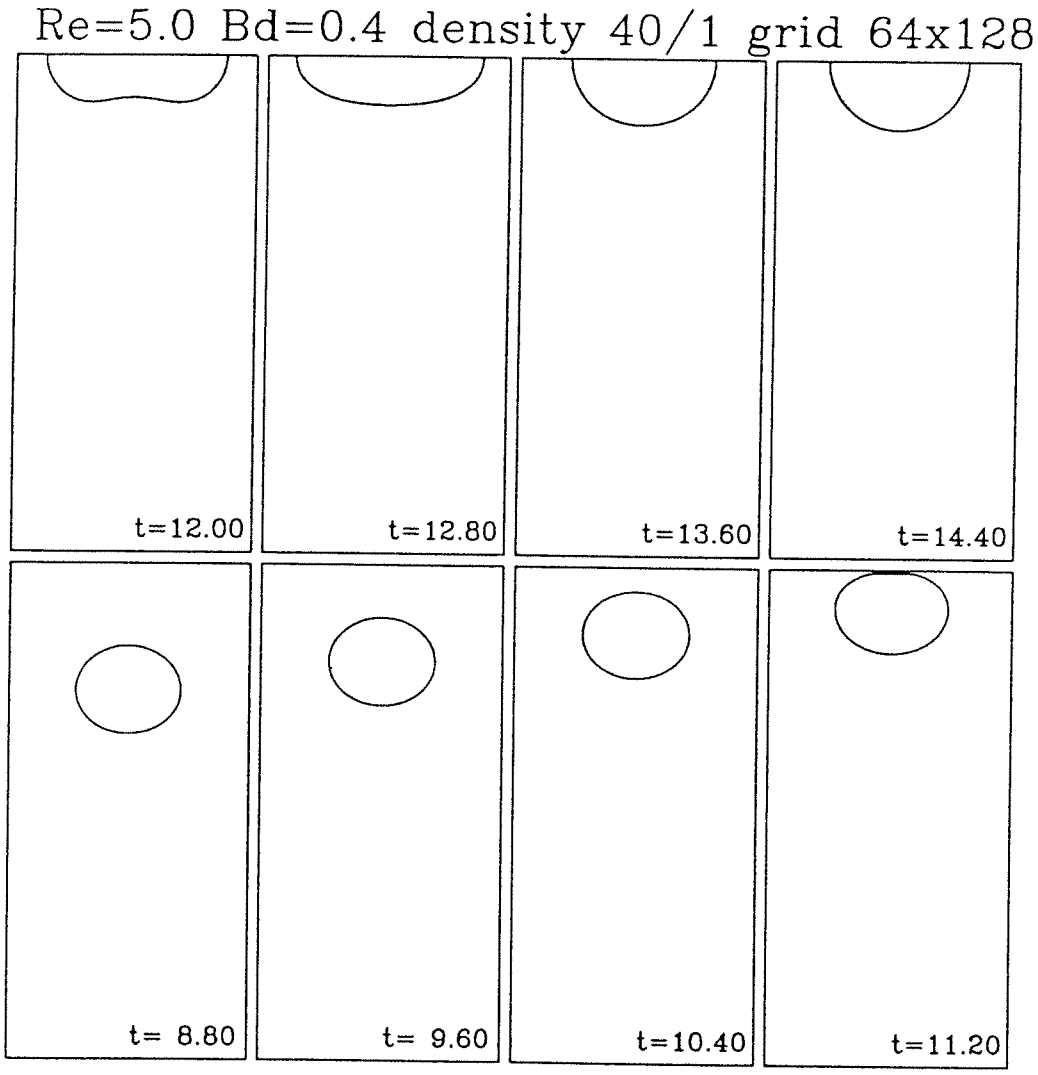

Figure 7.5: Evolution of 2D rising bubble with large surface tension. Bubble reaches a steady shape and velocity.

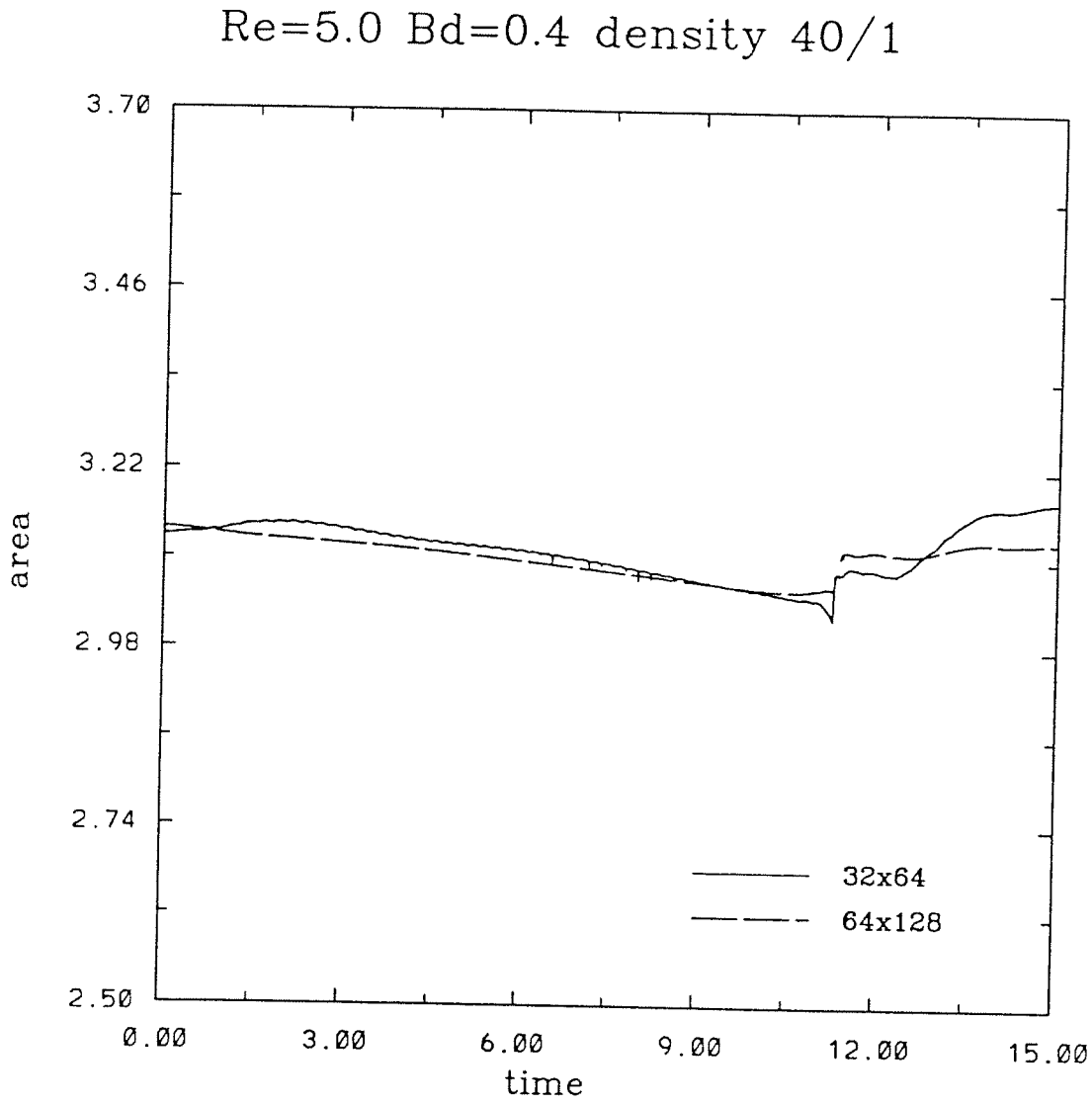

Figure 7.6: Convergence test for bubble rising with large surface tension: mass conservation.

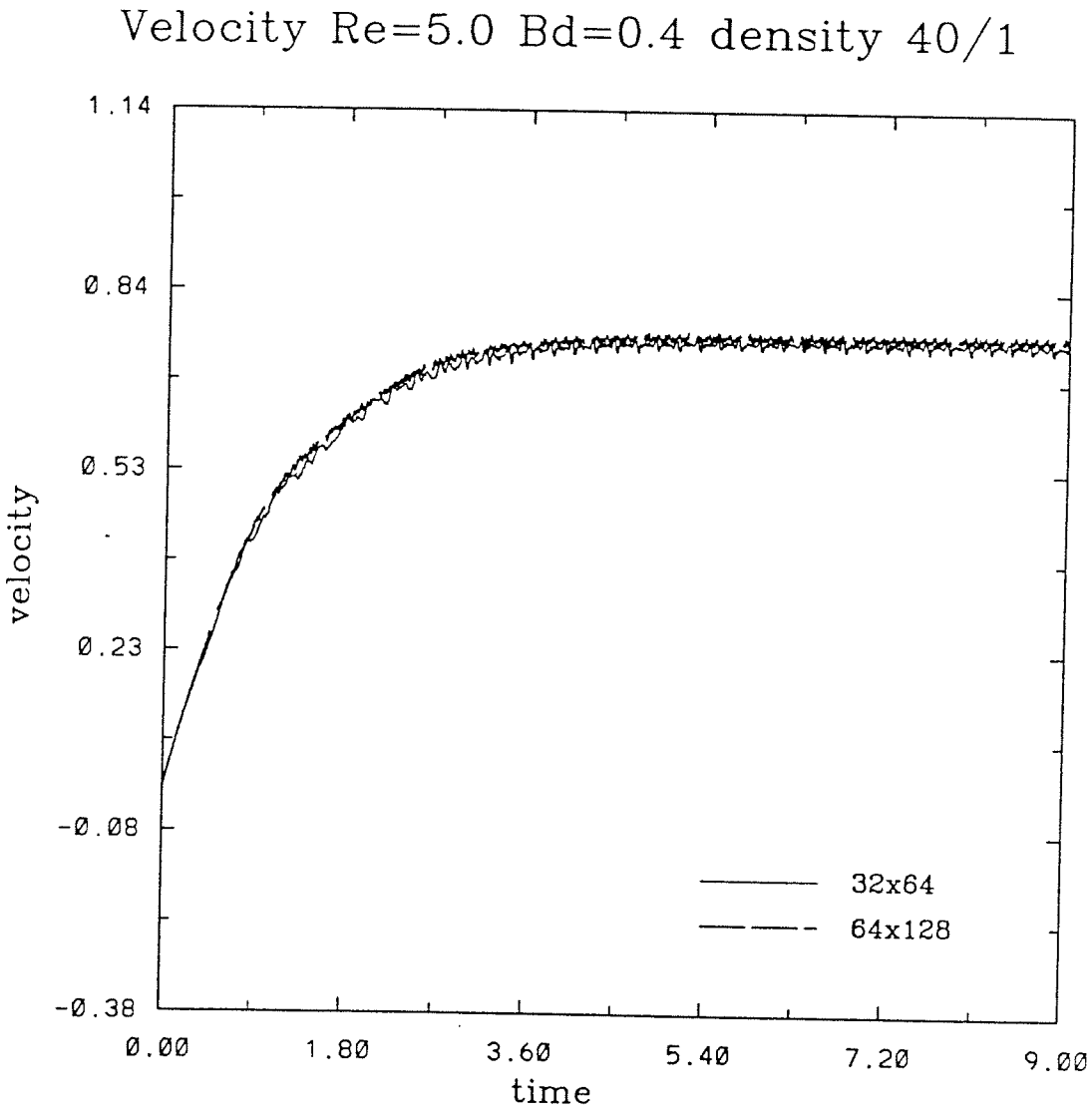

Figure 7.7: Convergence test for bubble rising with large surface tension: velocity steady state.

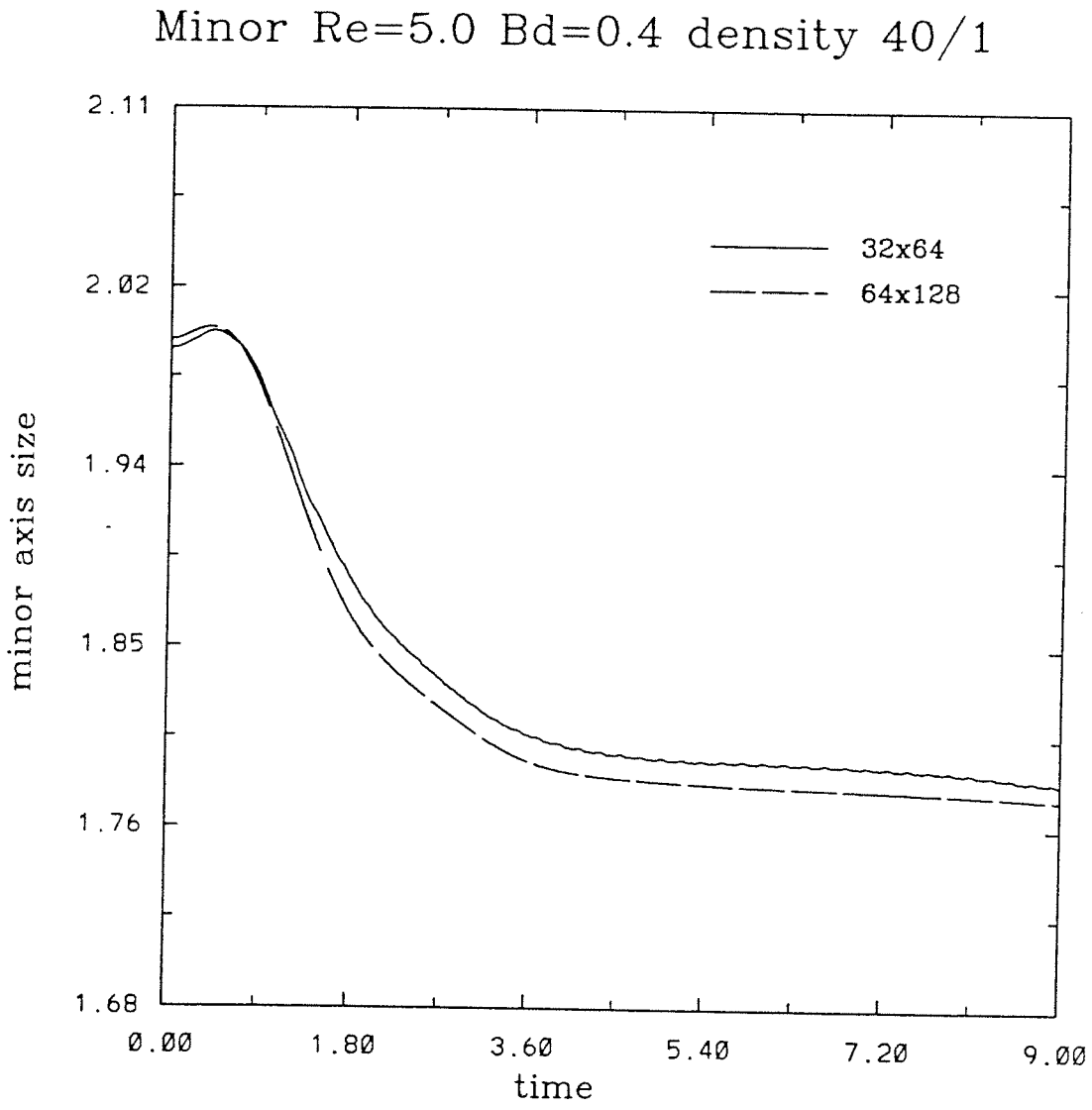

Figure 7.8: Convergence test for bubble rising with large surface tension: minor axis steady state.

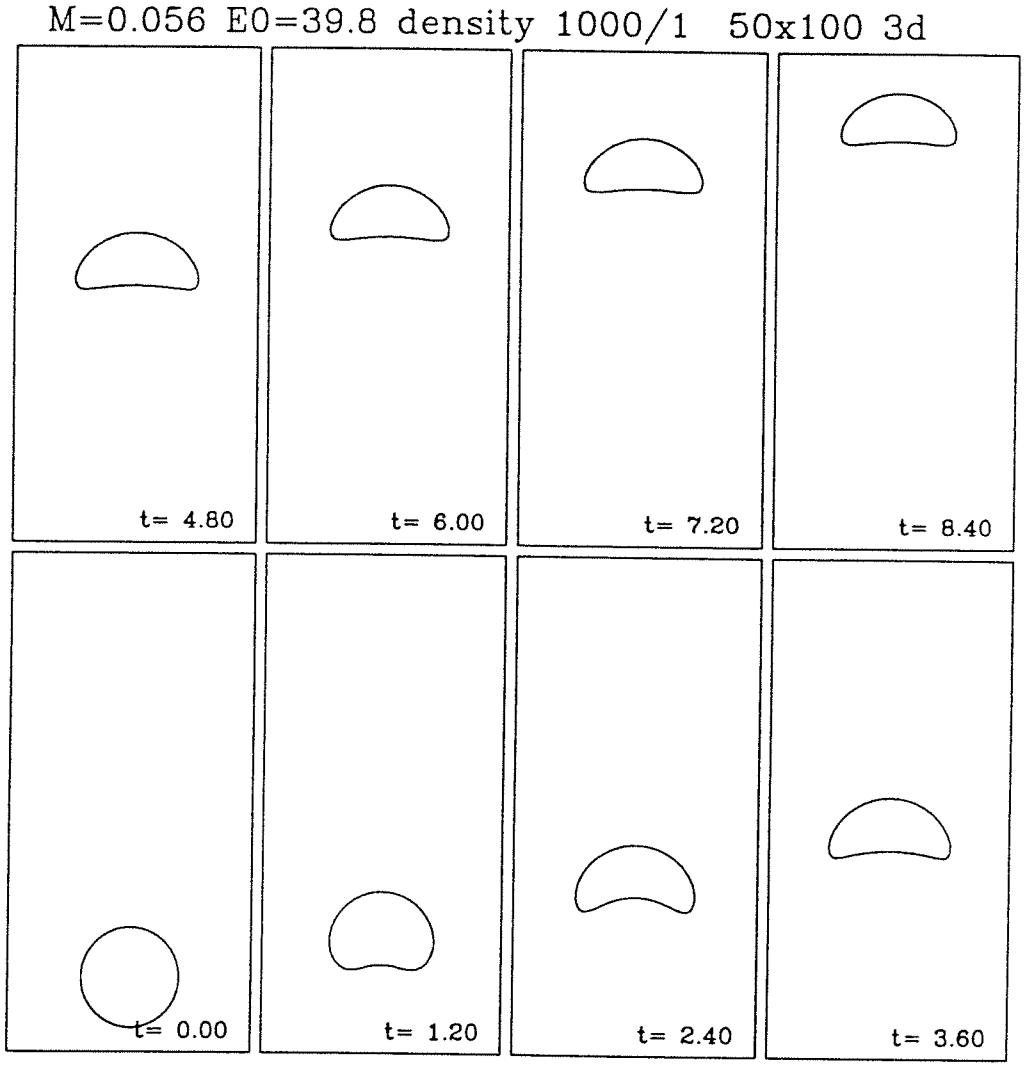

Figure 7.9: Evolution of 3D rising bubble with large surface tension. Bubble reaches a steady shape and velocity.

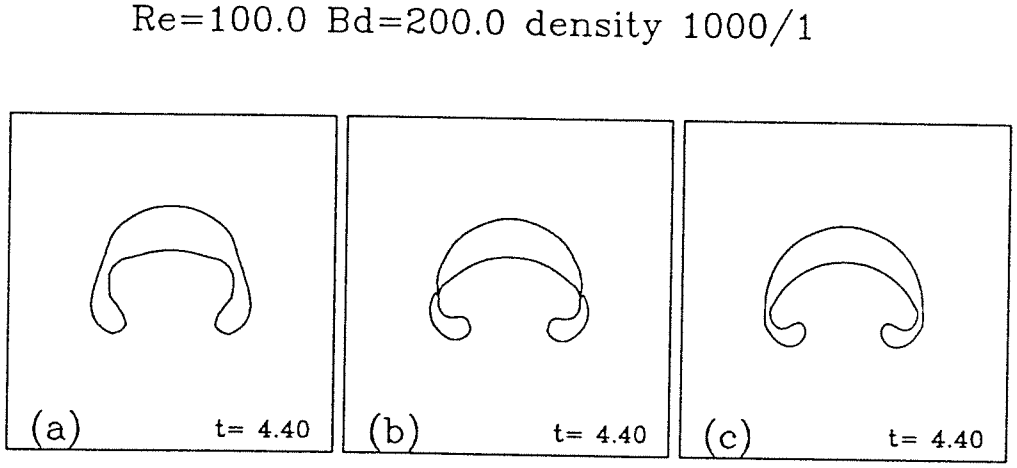

Figure 7.10: Convergence test for bubble rising with medium range Reynolds number and small surface tension. (a) 36×36 (b) 72×72 (c) 144×144

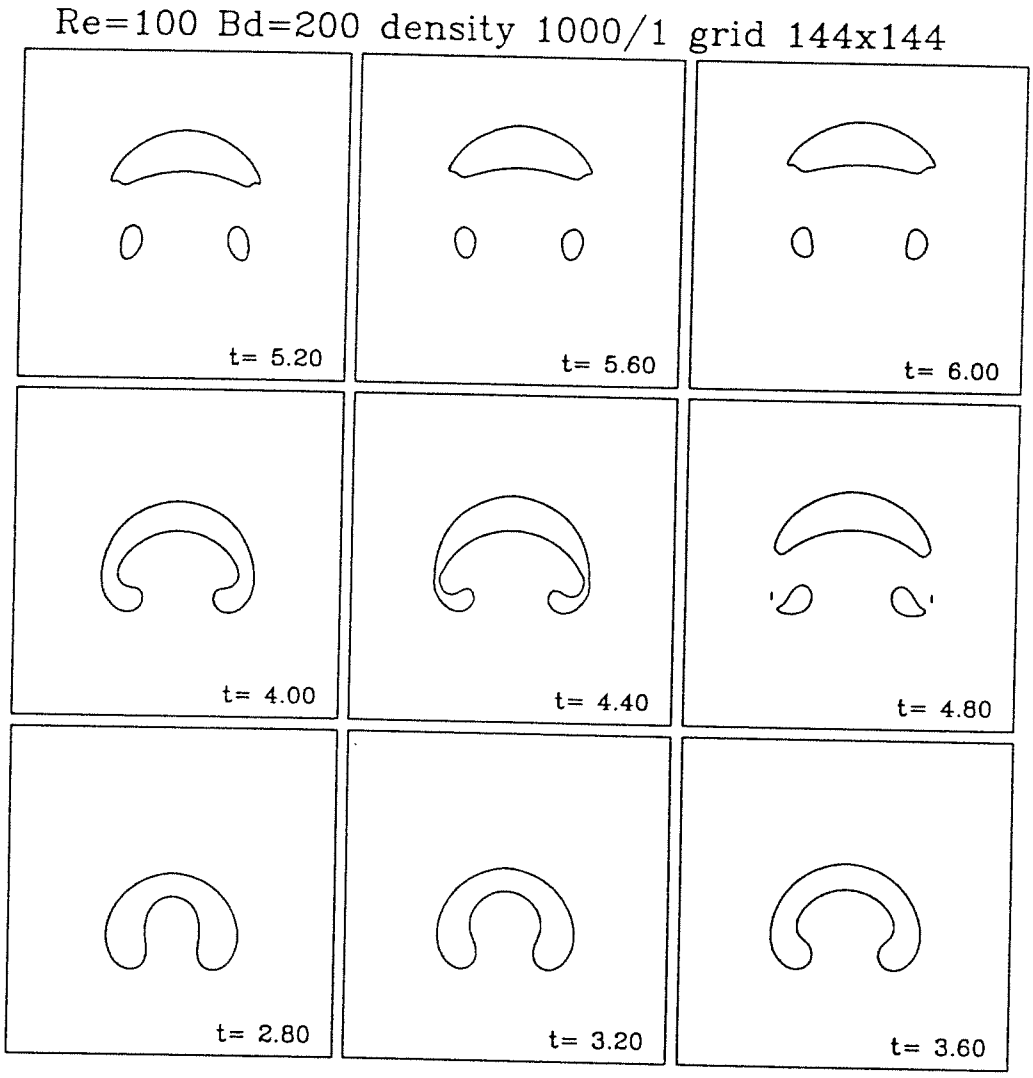

Figure 7.11: Evolution of rising bubble with medium range Reynolds number and small surface tension.

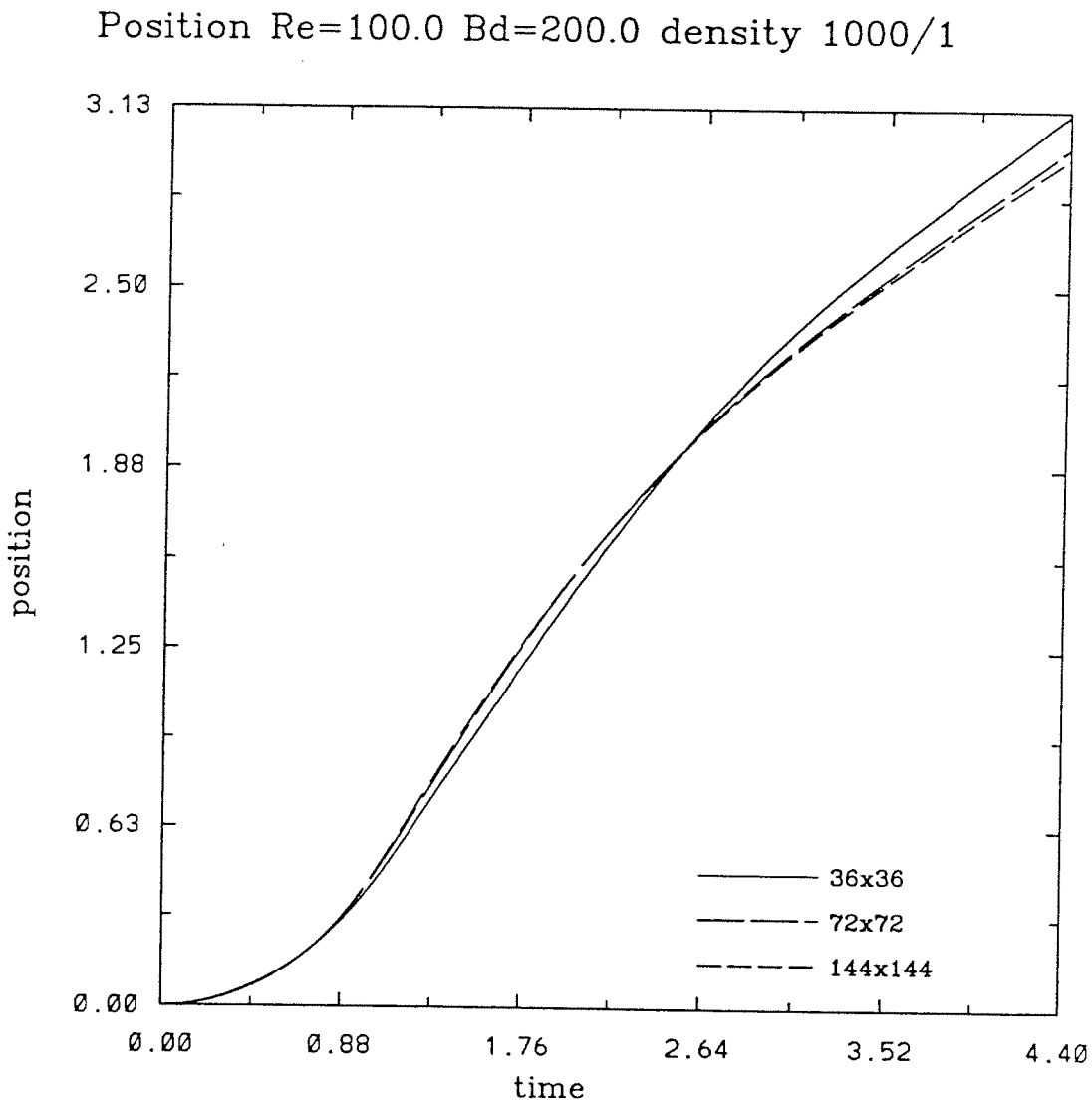

Figure 7.12: Convergence test for bubble rising with medium range Reynolds number and small surface tension: position.

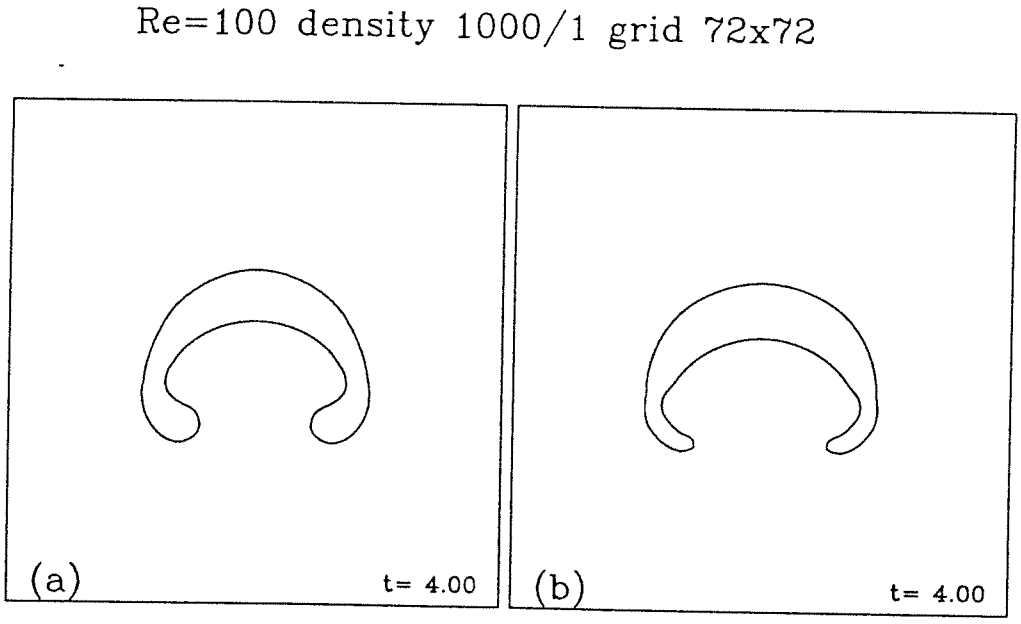

Figure 7.13: Surface tension effects on bubble rising with medium range Reynolds number. (a) Bond number 200.0 (b) Bond number 25.0

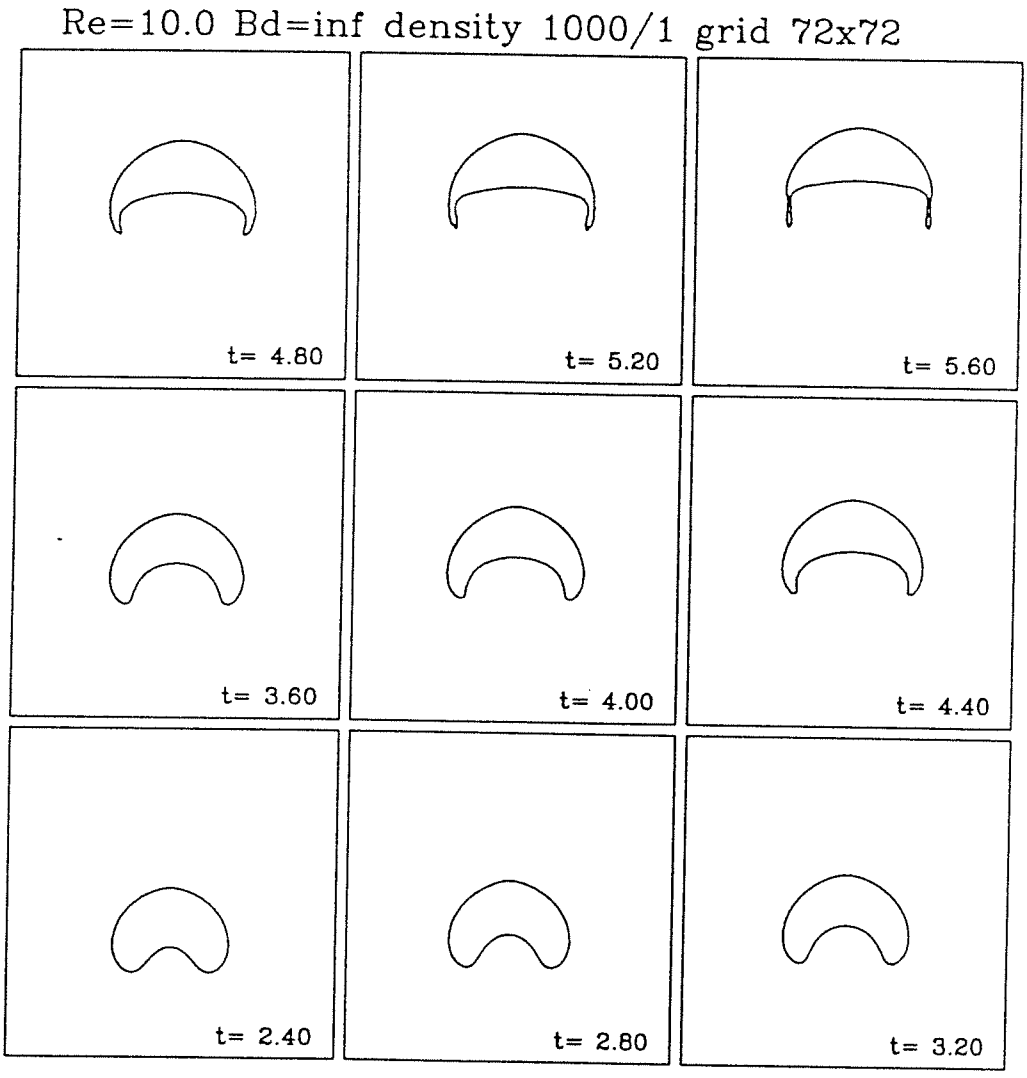

Figure 7.14: Evolution of rising bubble with low Reynolds number and no surface tension.

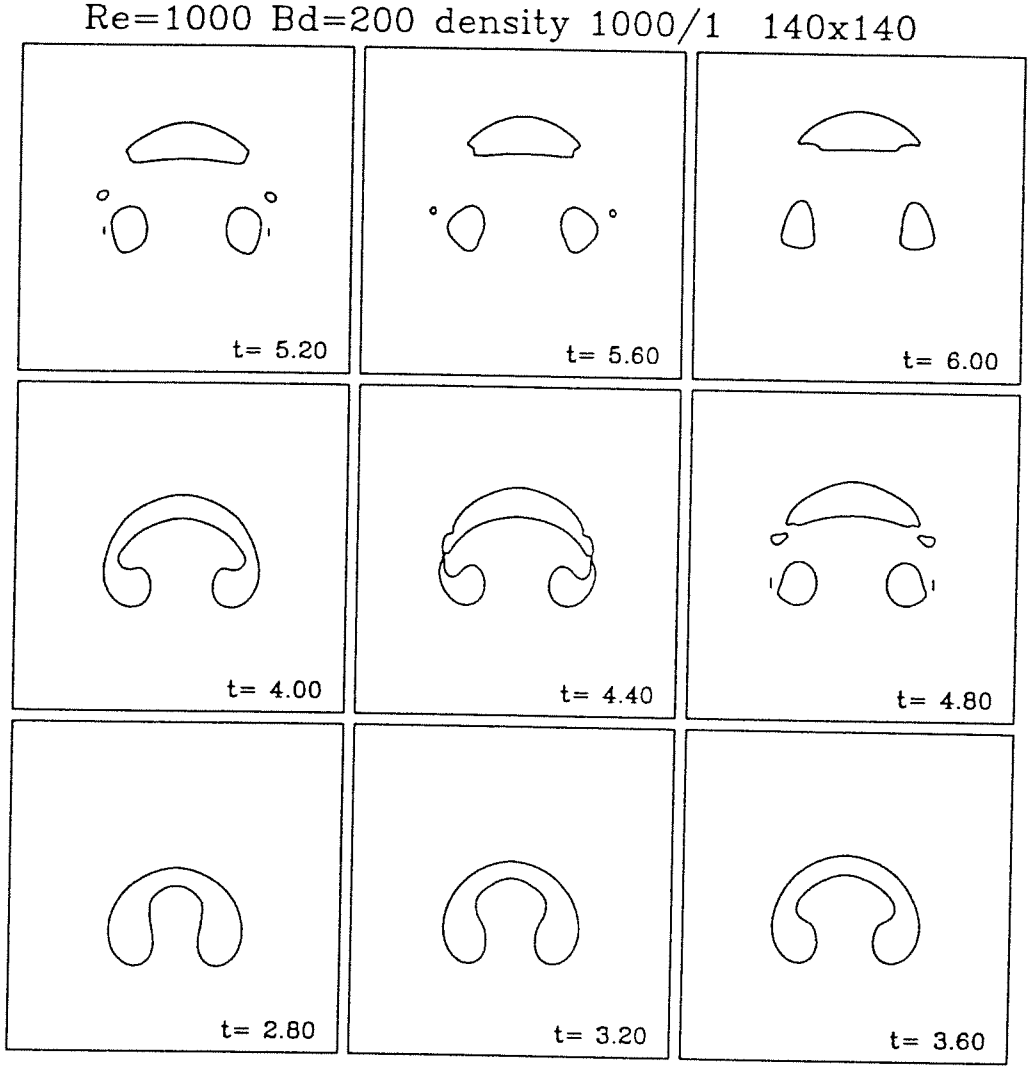

Figure 7.15: Evolution of 2D rising bubble with high Reynolds number and low surface tension.

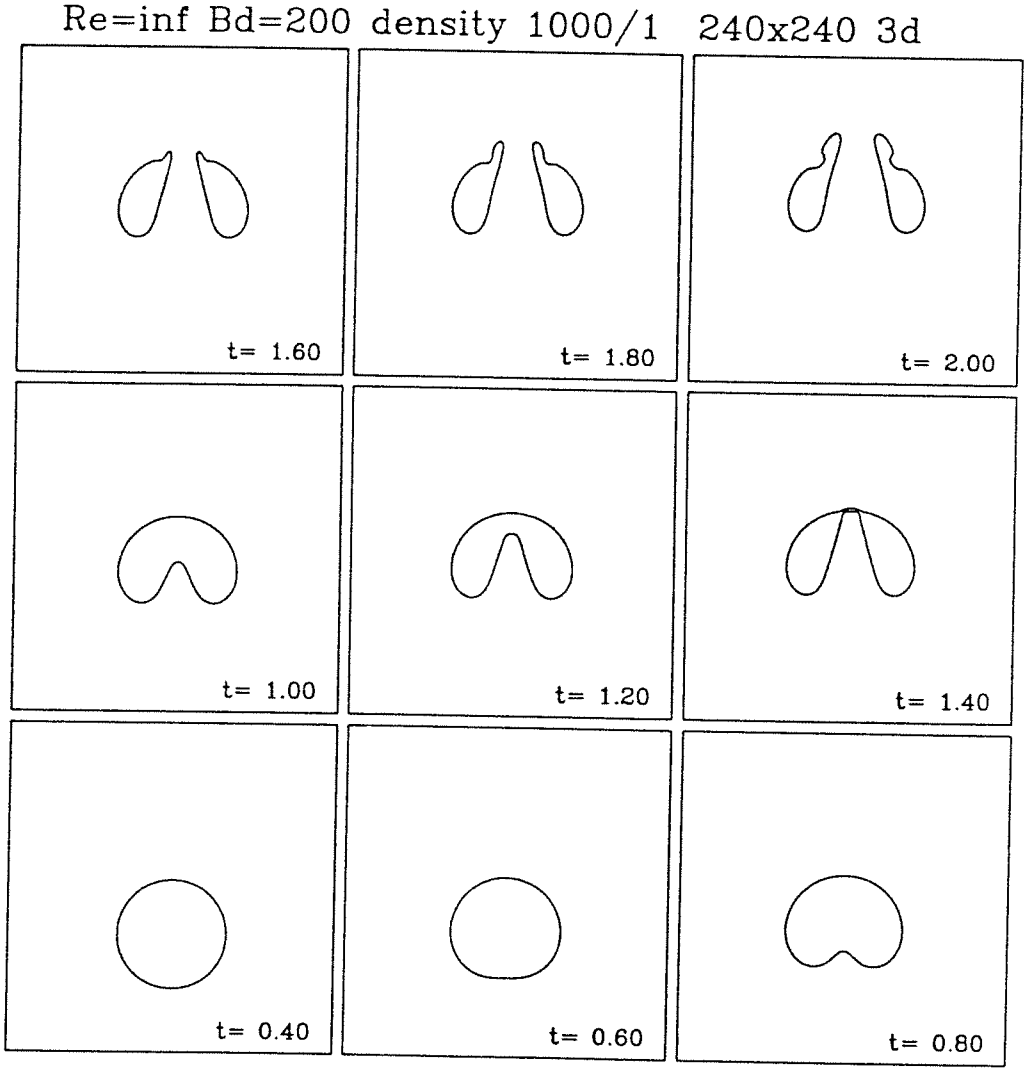

Figure 7.16: Evolution of 3D rising bubble with no viscosity and little surface tension. $\alpha = 3h$

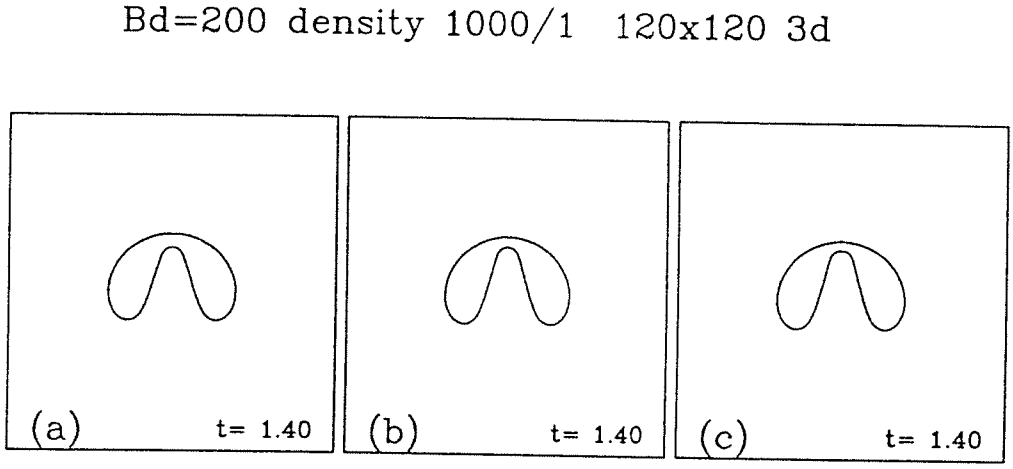

Figure 7.17: Convergence check for 3D rising bubble as Reynolds number approaches infinity ($\alpha = 3h/2$). (a) $Re = 200$ (b) $Re = 400$ (c) $Re = 800$

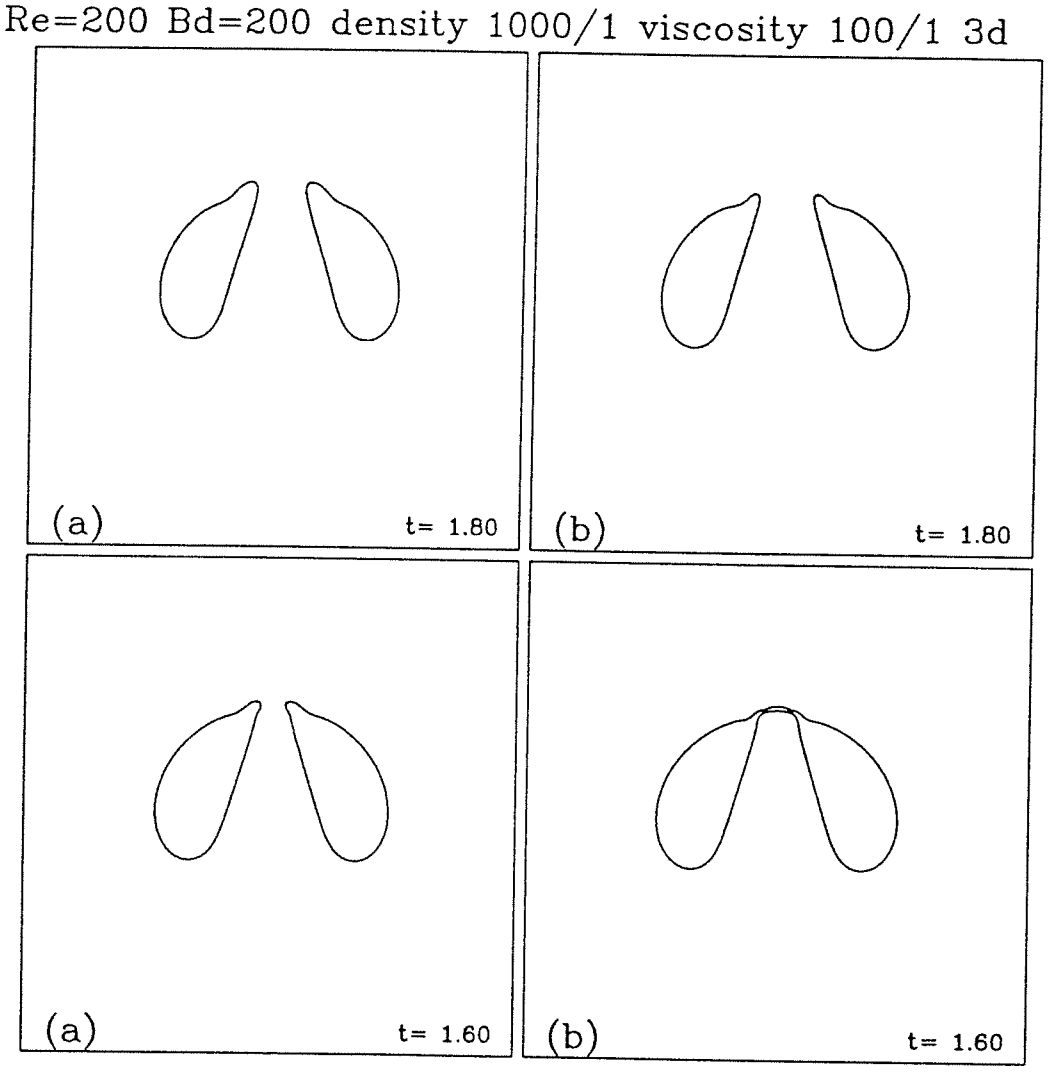

Figure 7.18: Convergence check for 3D rising bubble at time of break-up. High Reynolds number flow with low surface tension. (a) 100x100 (b) 200x200

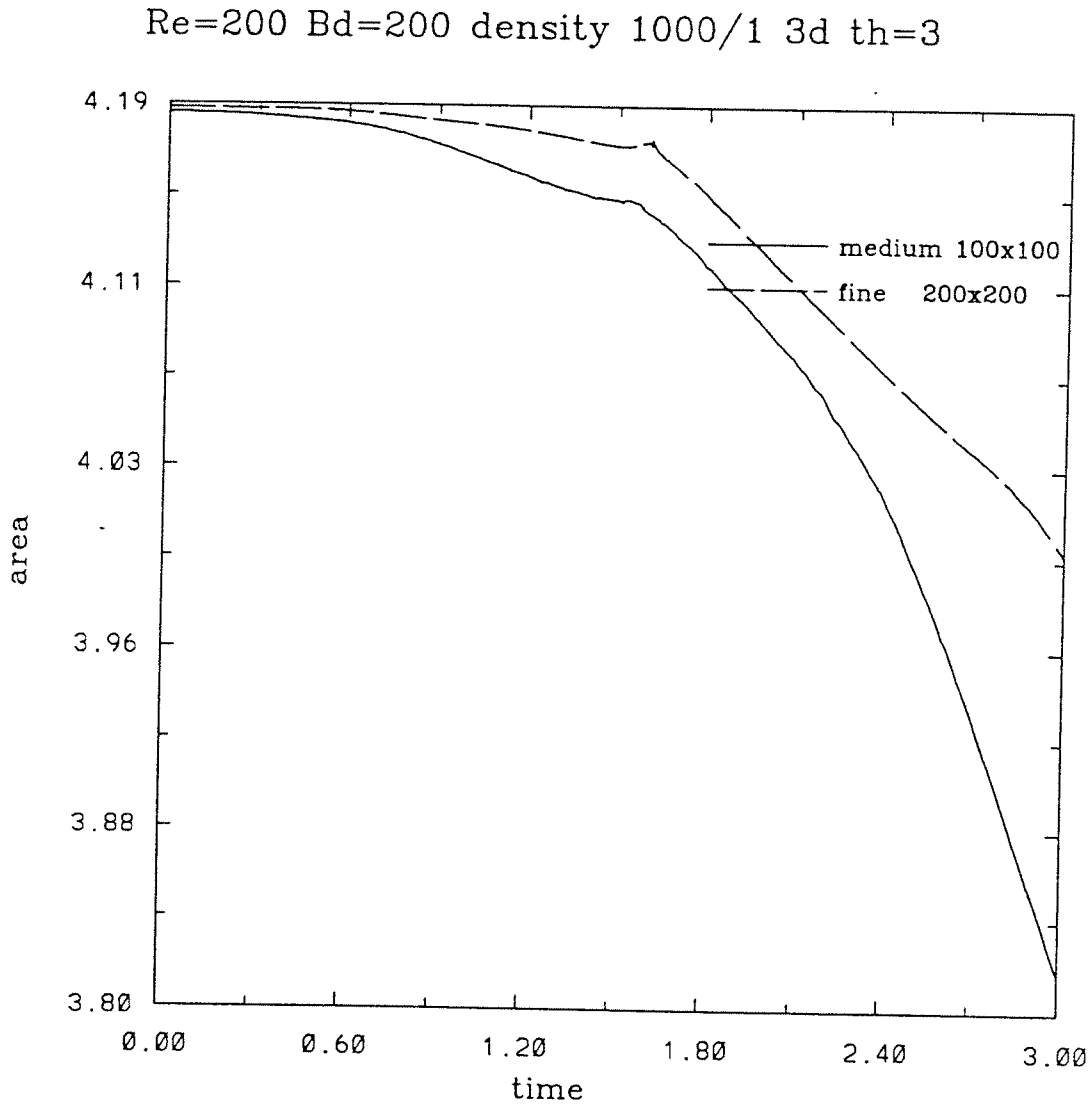

Figure 7.19: Volume conservation for 3D rising bubble at time of break-up. High Reynolds number flow with low surface tension.

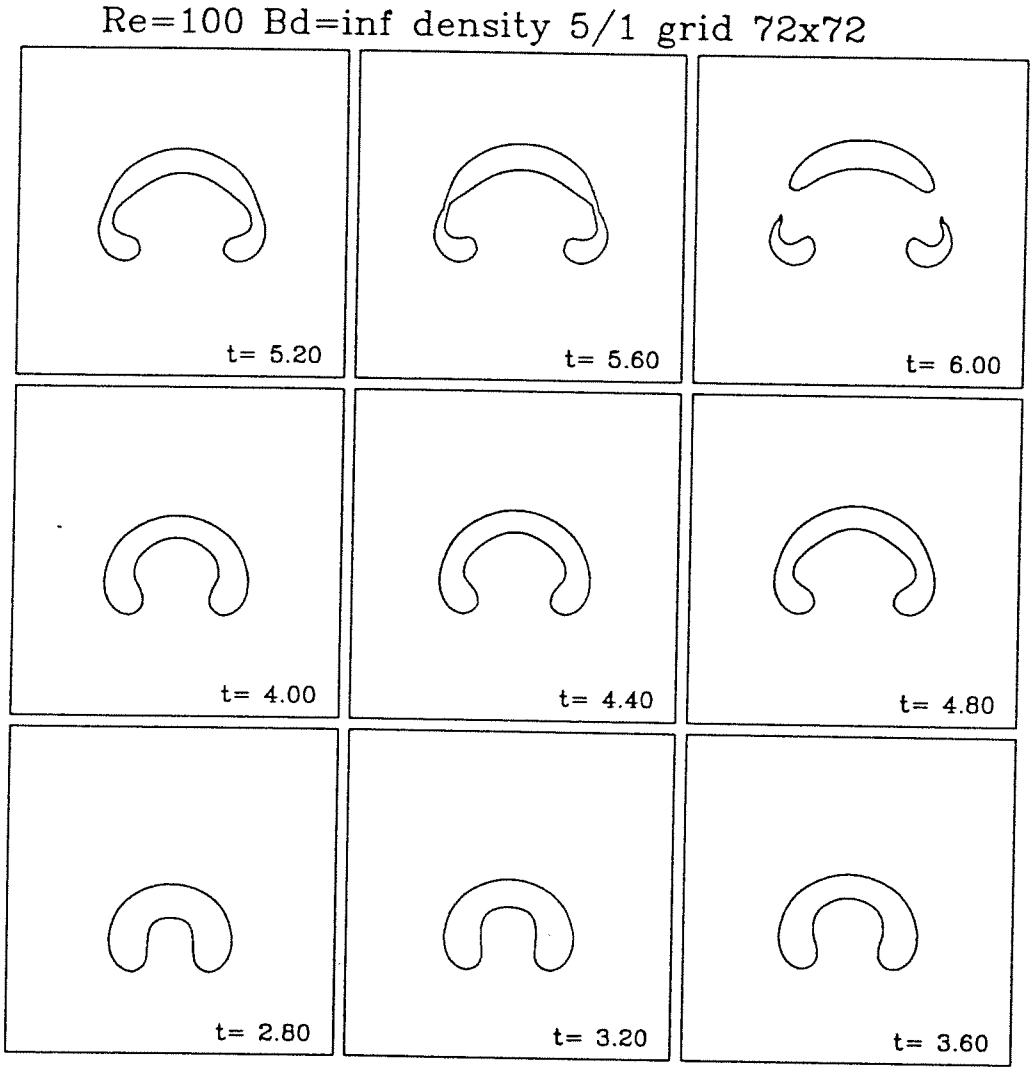

Figure 7.20: Evolution of rising bubble with low density ratio and medium range Reynolds number.

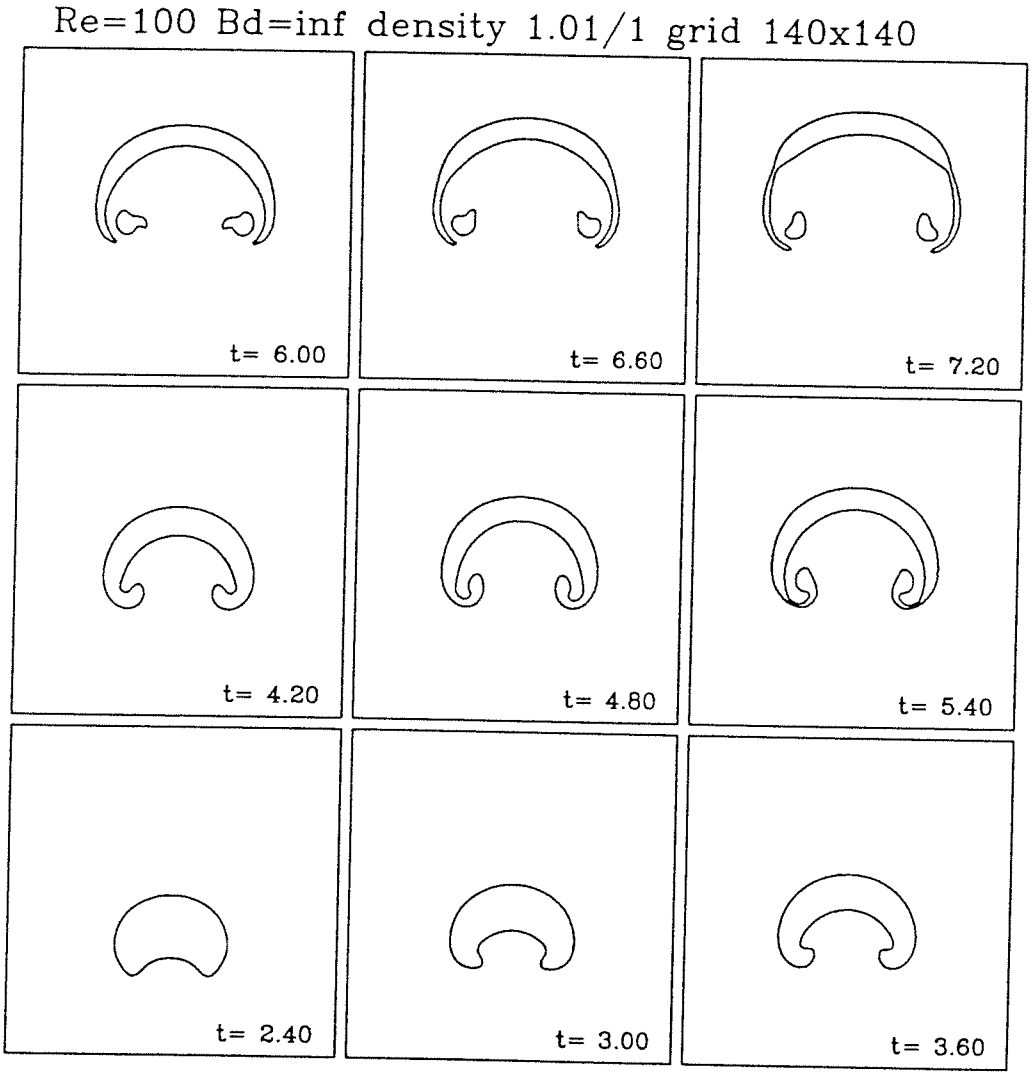

Figure 7.21: Evolution of rising bubble with slight density ratio and medium range Reynolds number.

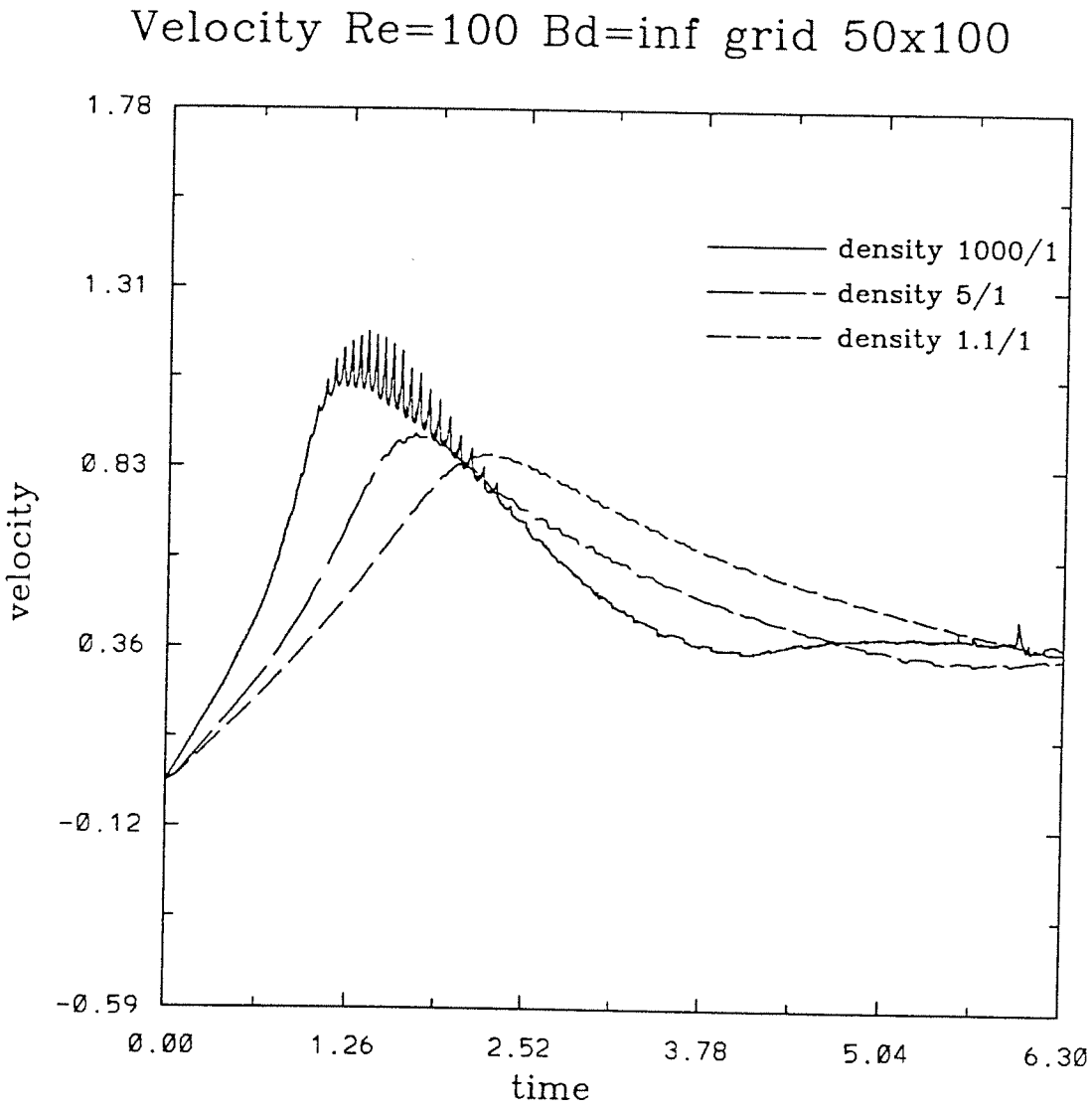

Figure 7.22: Effects of density ratio on bubble rise velocity.

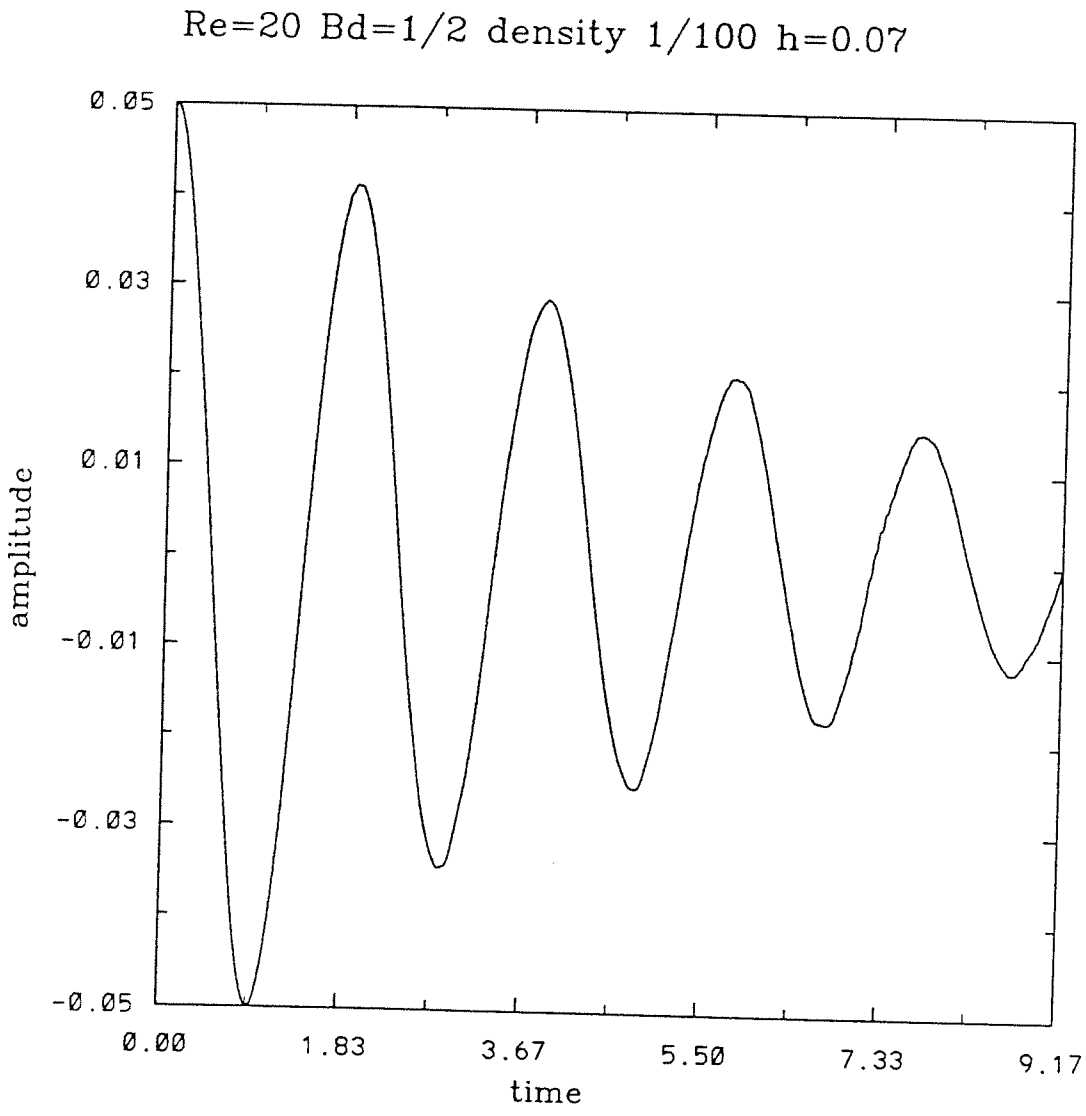

Figure 7.23: Amplitudinal oscillations of a two-dimensional drop driven by surface tension forces. Amplitude decays exponentially due to viscosity.

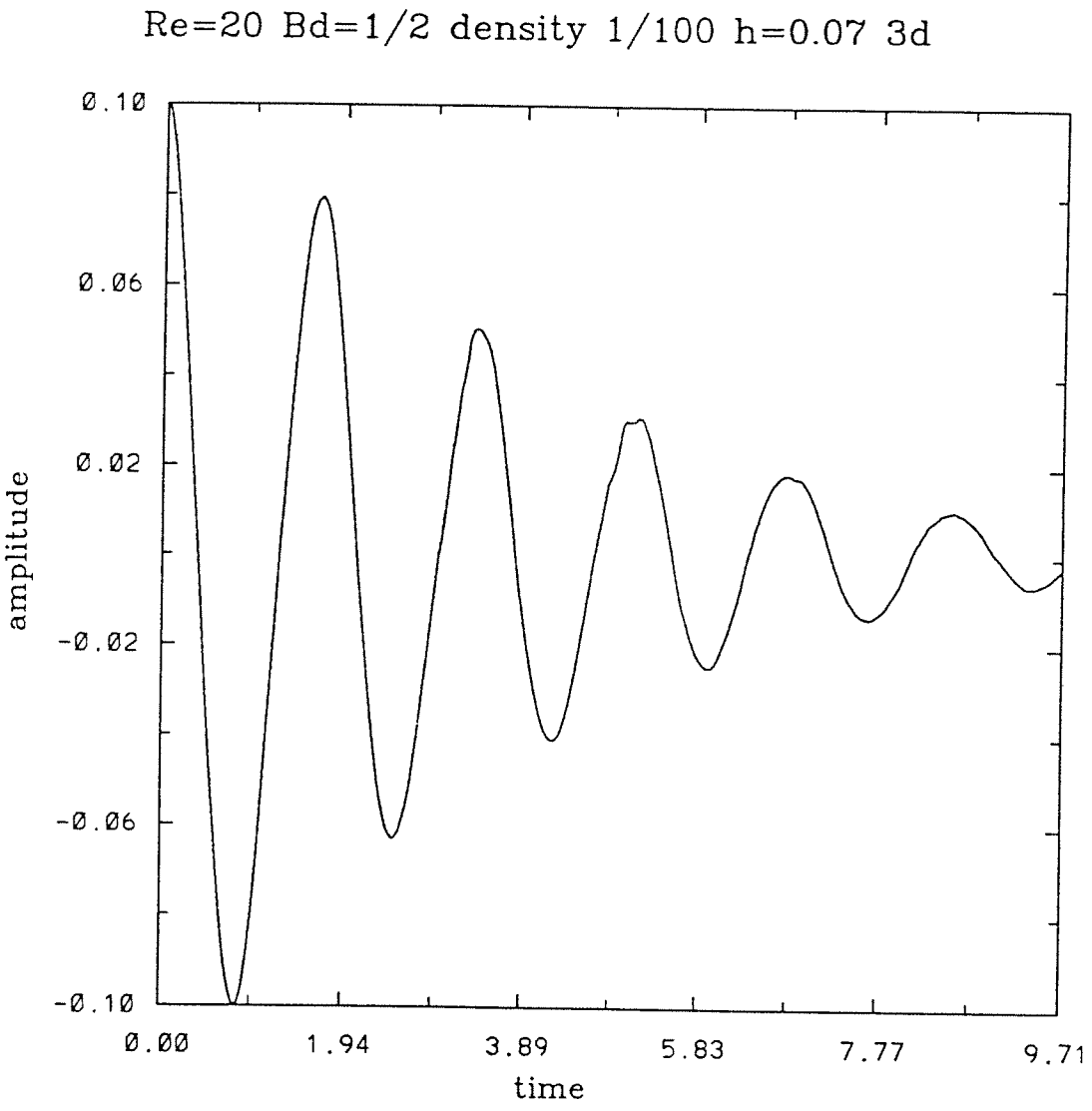

Figure 7.24: Amplitudinal oscillations of a three-dimensional drop driven by surface tension forces. Amplitude decays exponentially due to viscosity.

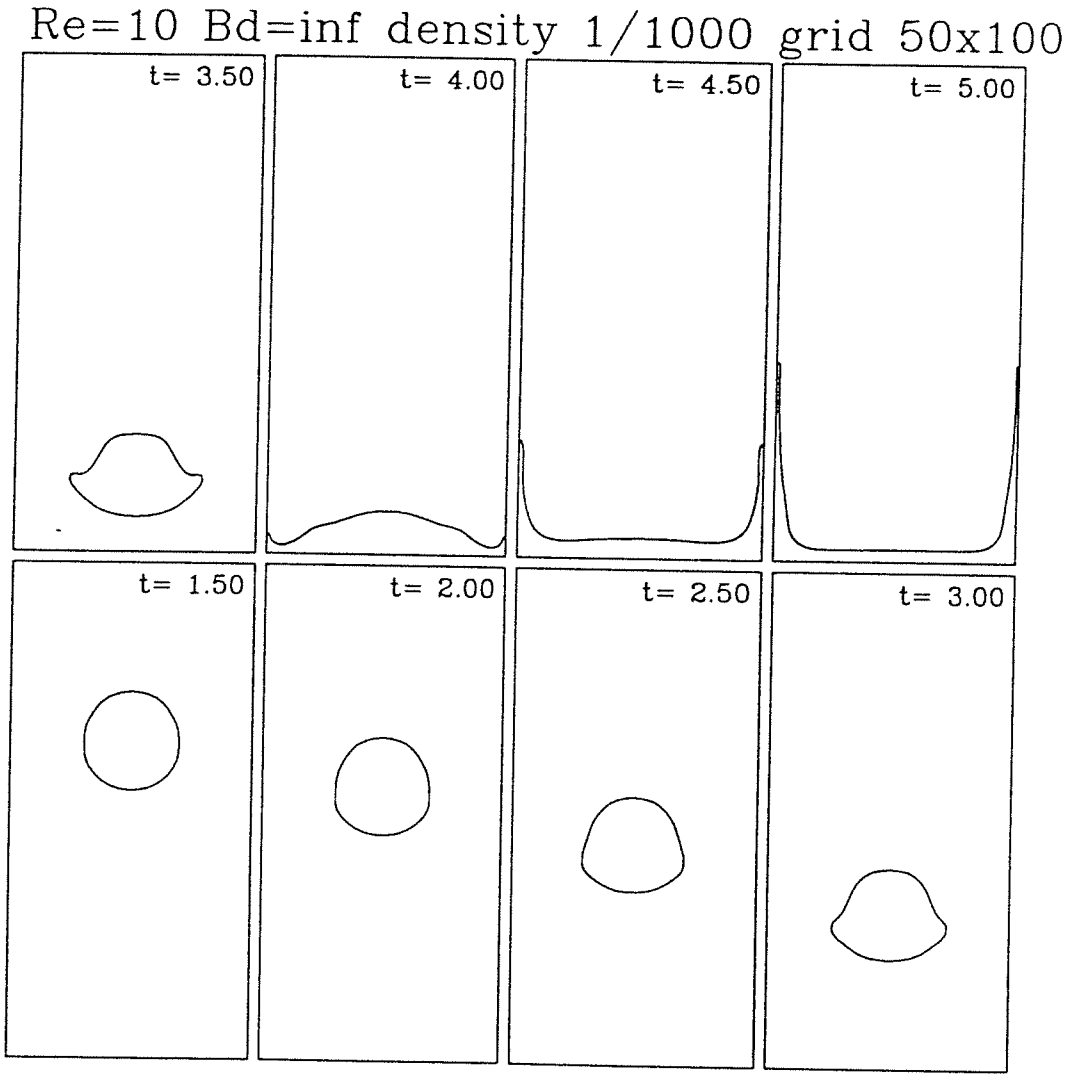

Figure 7.25: Evolution of a large water drop (no surface tension). Drop deforms as it hits the base.

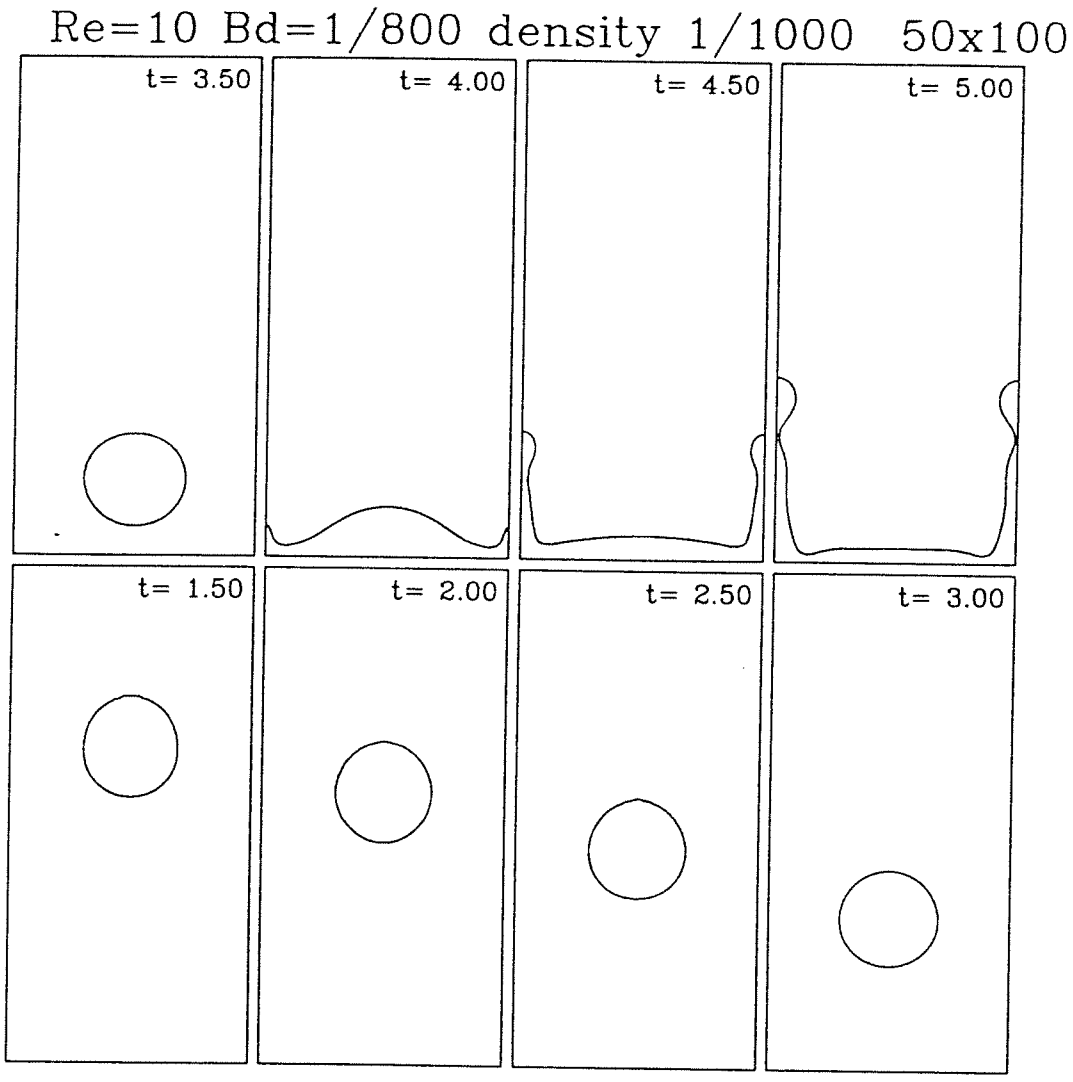

Figure 7.26: Evolution of a water drop with surface tension. Drop remains circular as it hits the base.

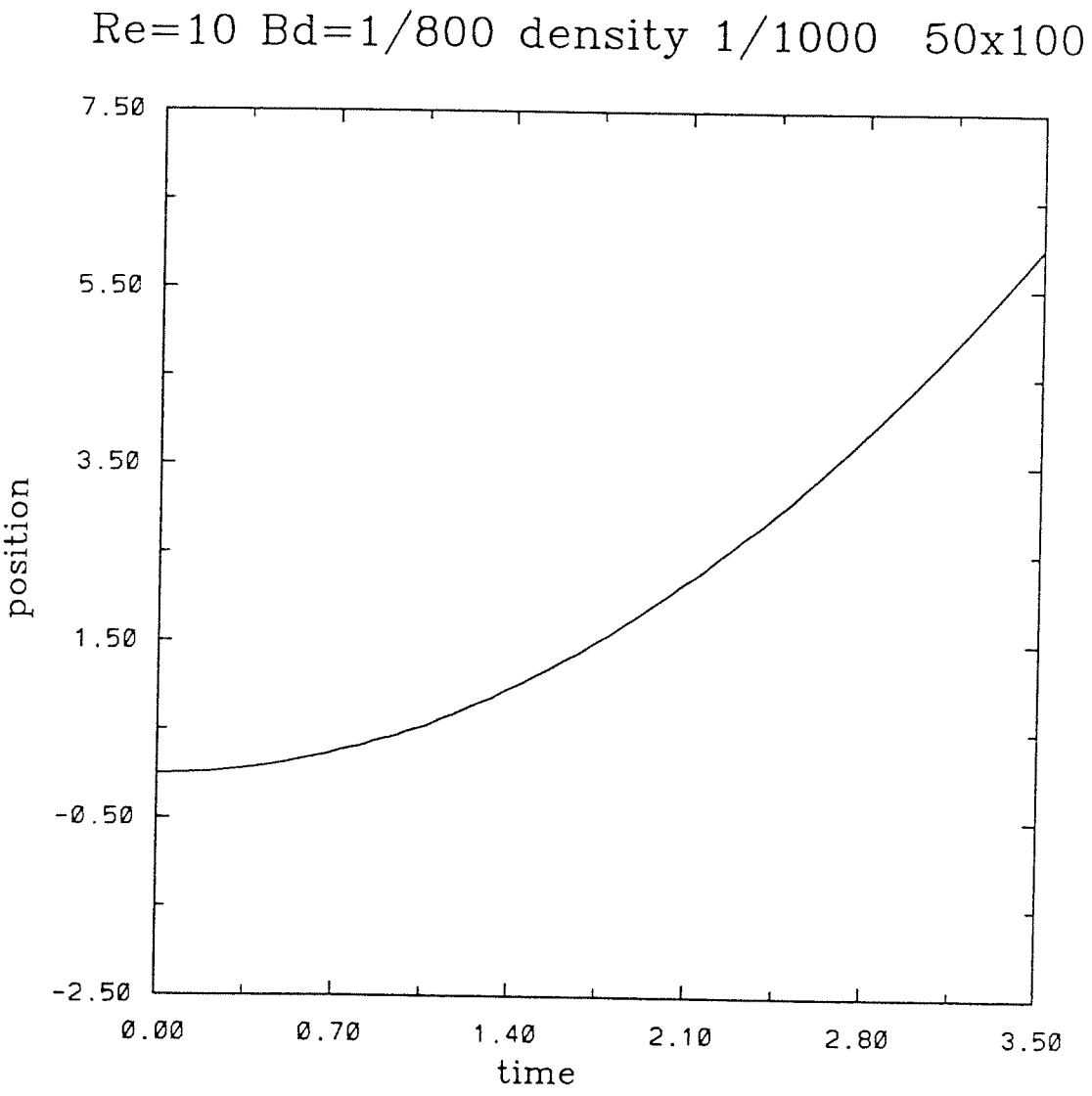

Figure 7.27: Position of water drop with surface tension versus time.

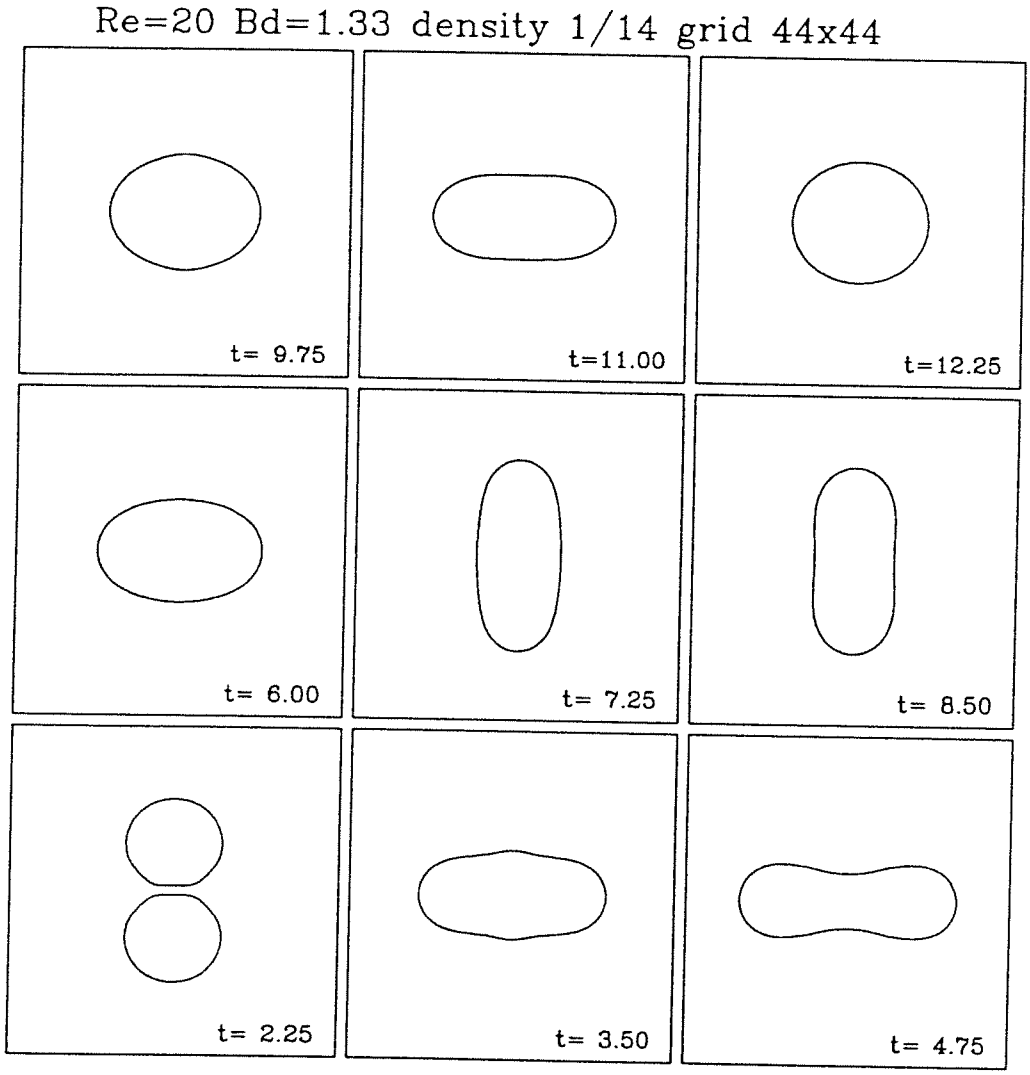

Figure 7.28: Evolution of two 2D water drops colliding with each other. Combined drop experiences surface tension driven oscillations.

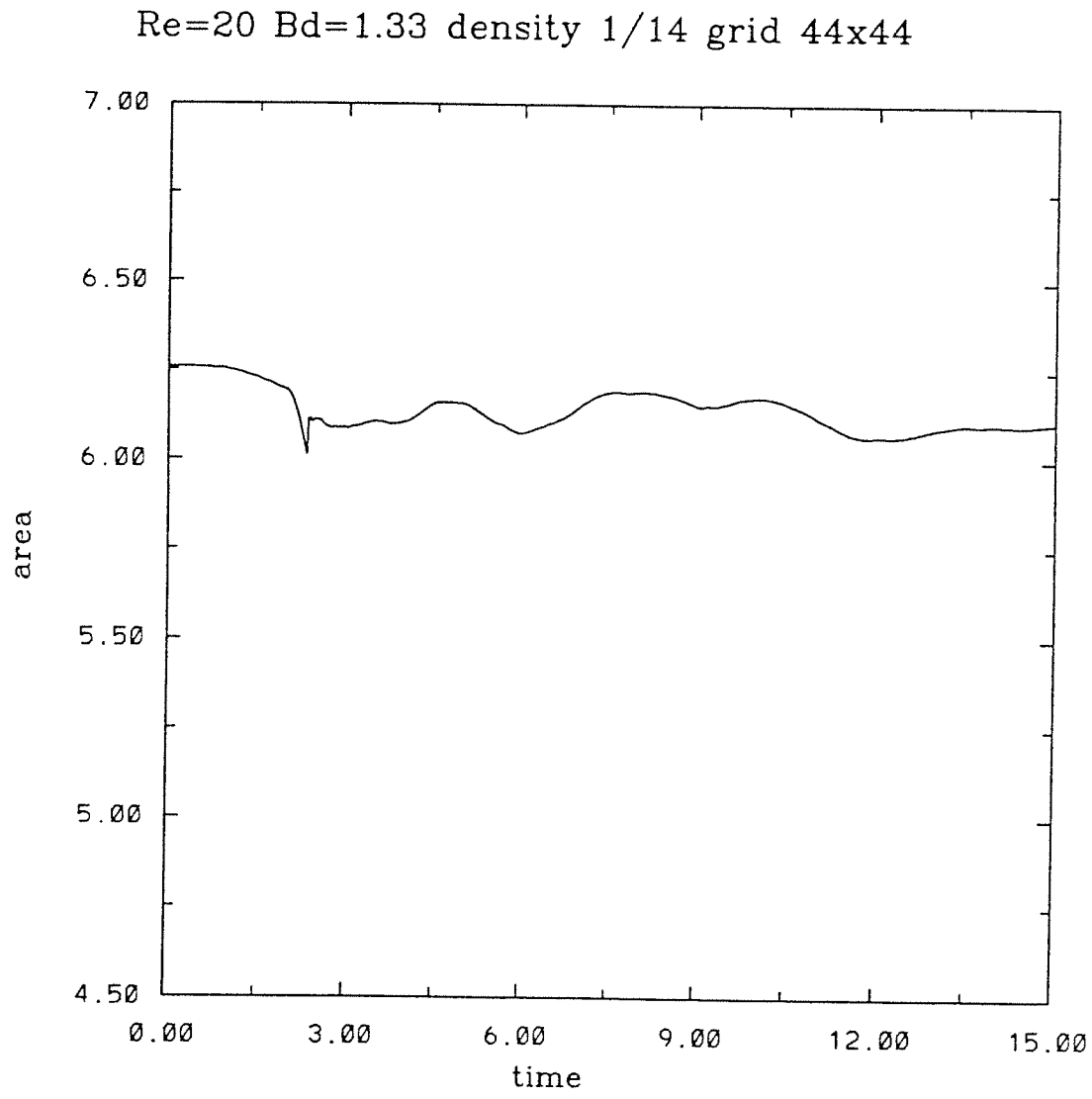

Figure 7.29: Conservation of mass for colliding drop problem.

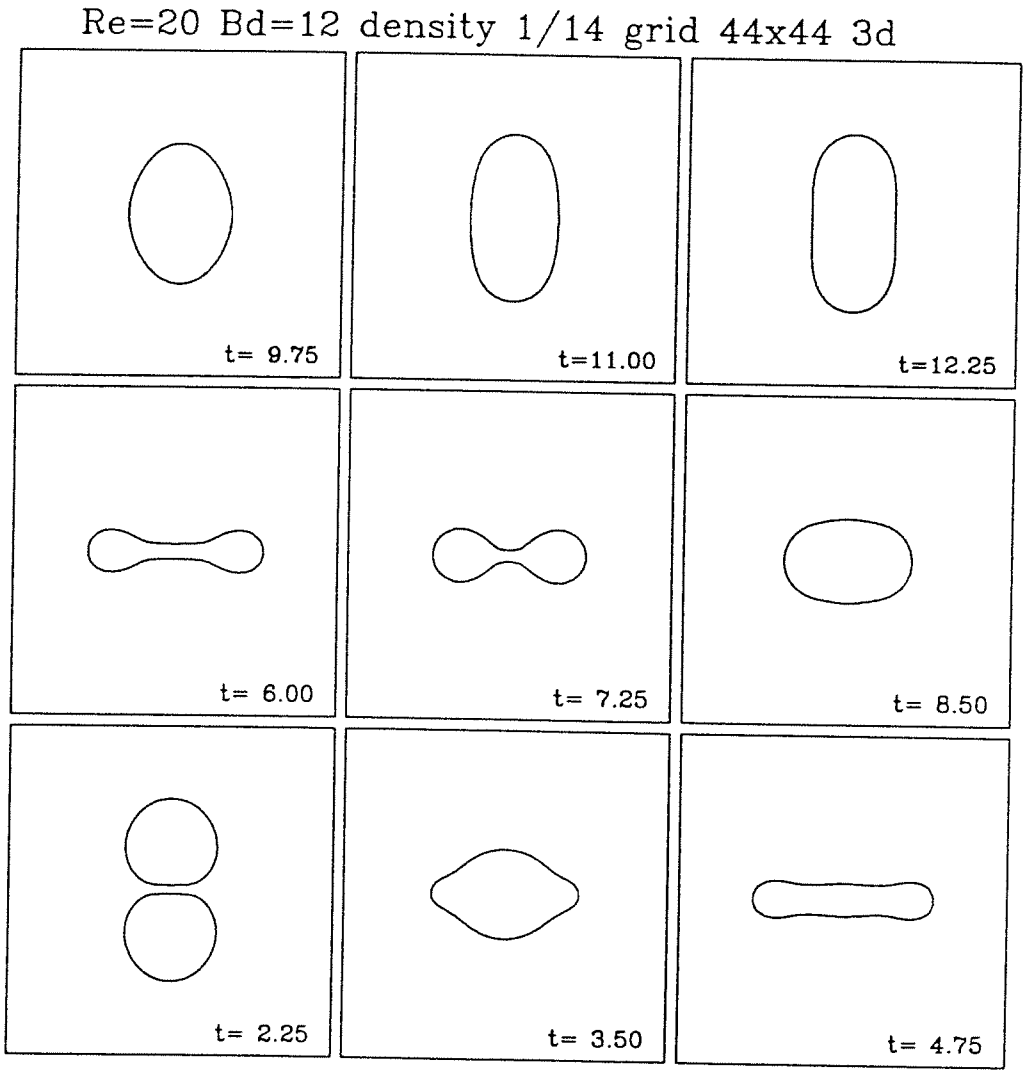

Figure 7.30: Evolution of two 3D water drops colliding with each other. Combined drop experiences surface tension driven oscillations.

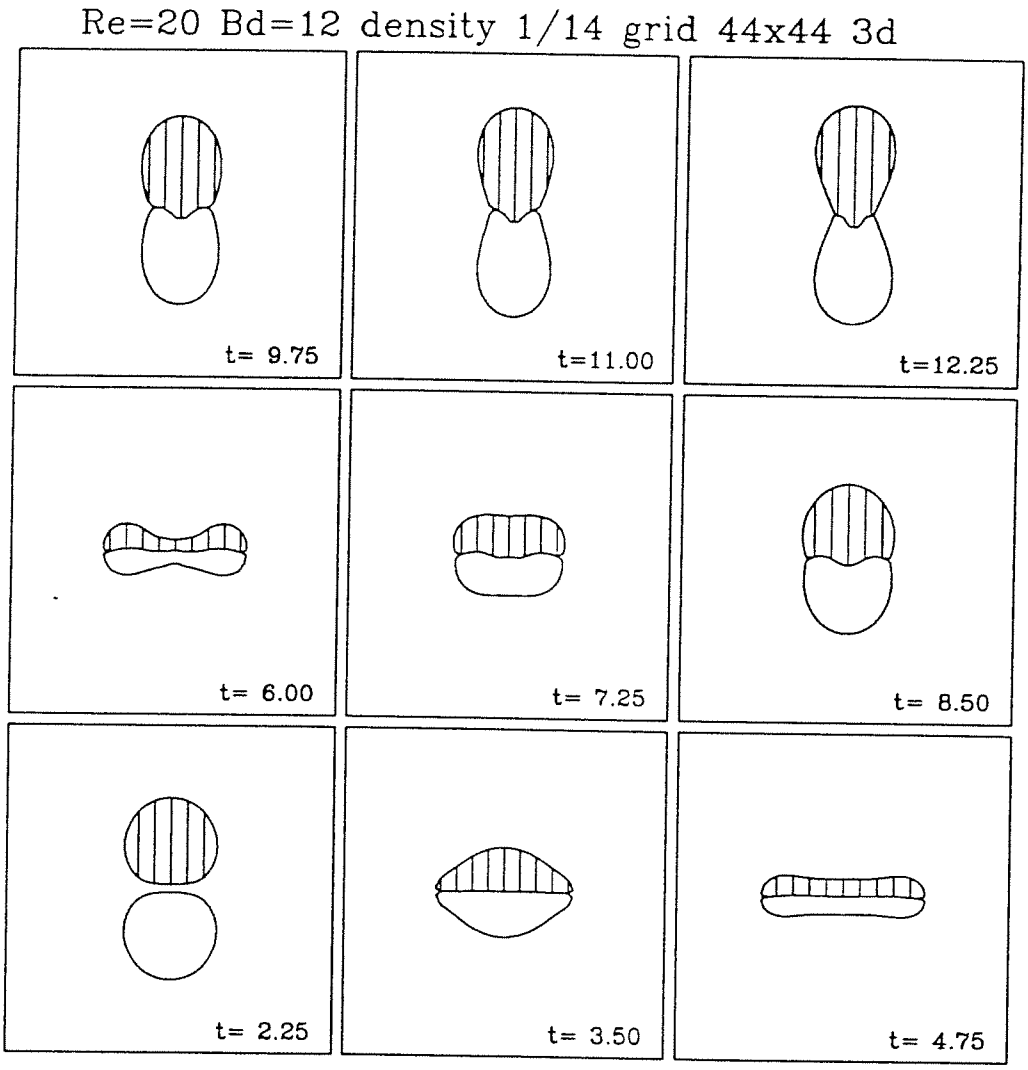

Figure 7.31: Evolution of two 3D water drops colliding with each other. Drops are burst on contact. Surface tension is modeled using the average of level set functions active at the interface.

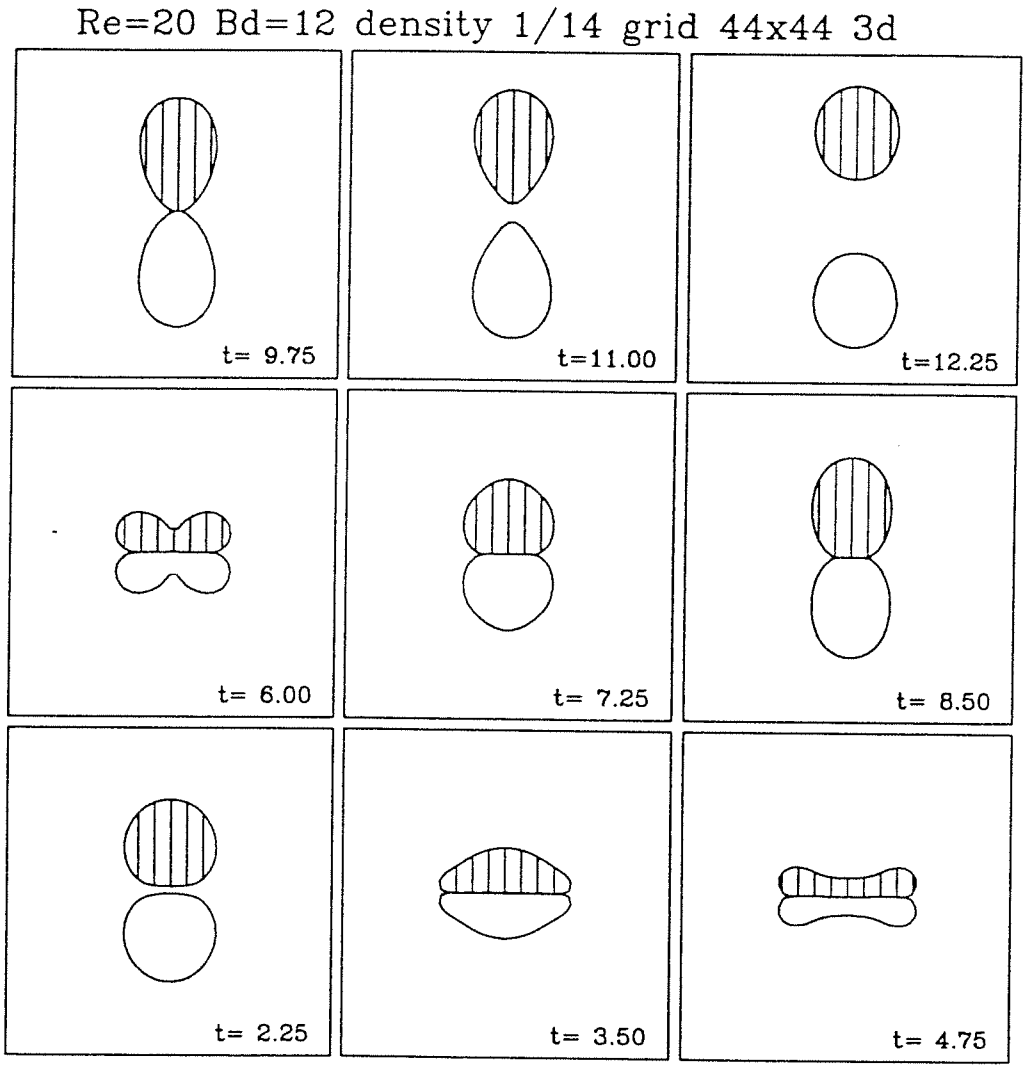

Figure 7.32: Evolution of two 3D water drops colliding with each other. Drops never allowed to burst. Surface tension at interface depends on ϕ_1 and/or ϕ_3.

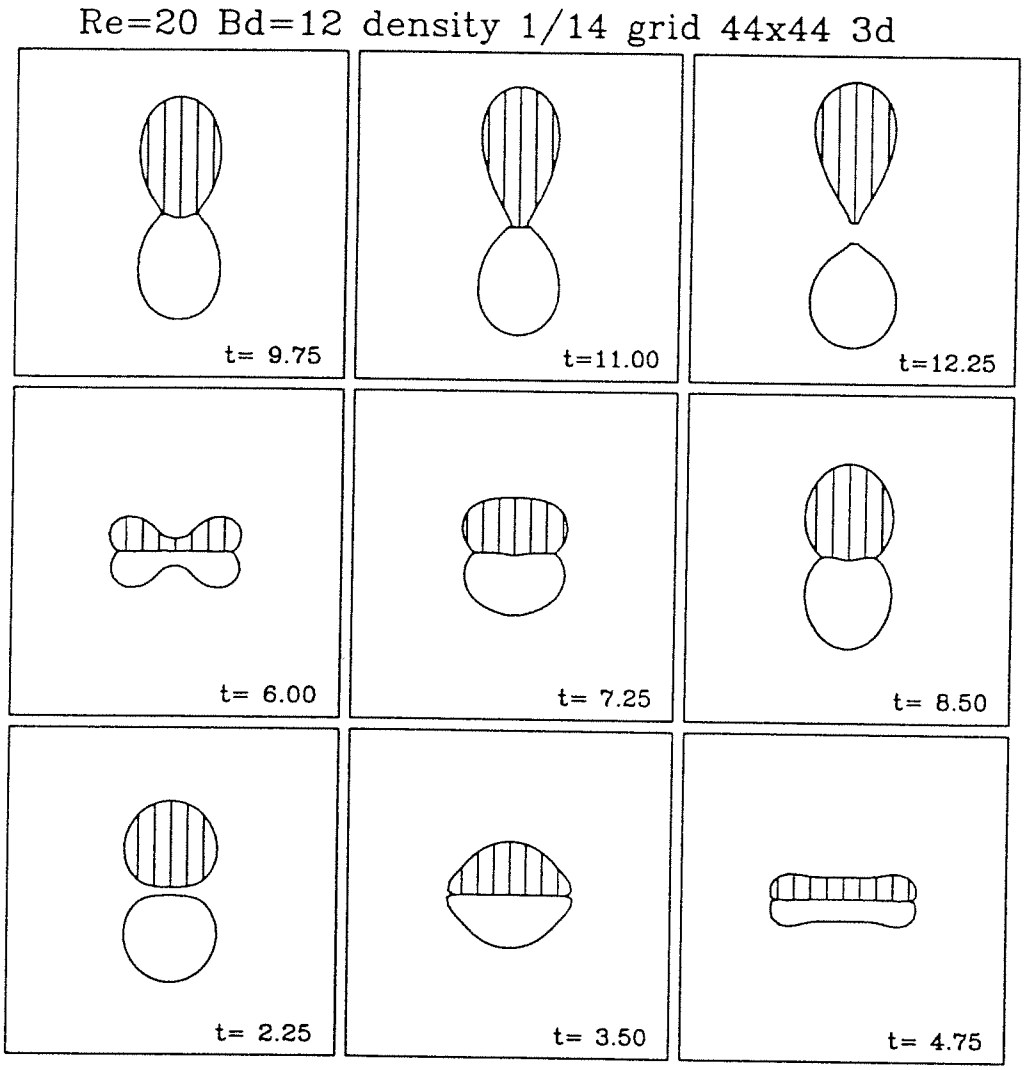

Figure 7.33: Evolution of two 3D water drops colliding with each other. Drops are burst on contact. Surface tension at interface depends on ϕ_1 and/or ϕ_3.

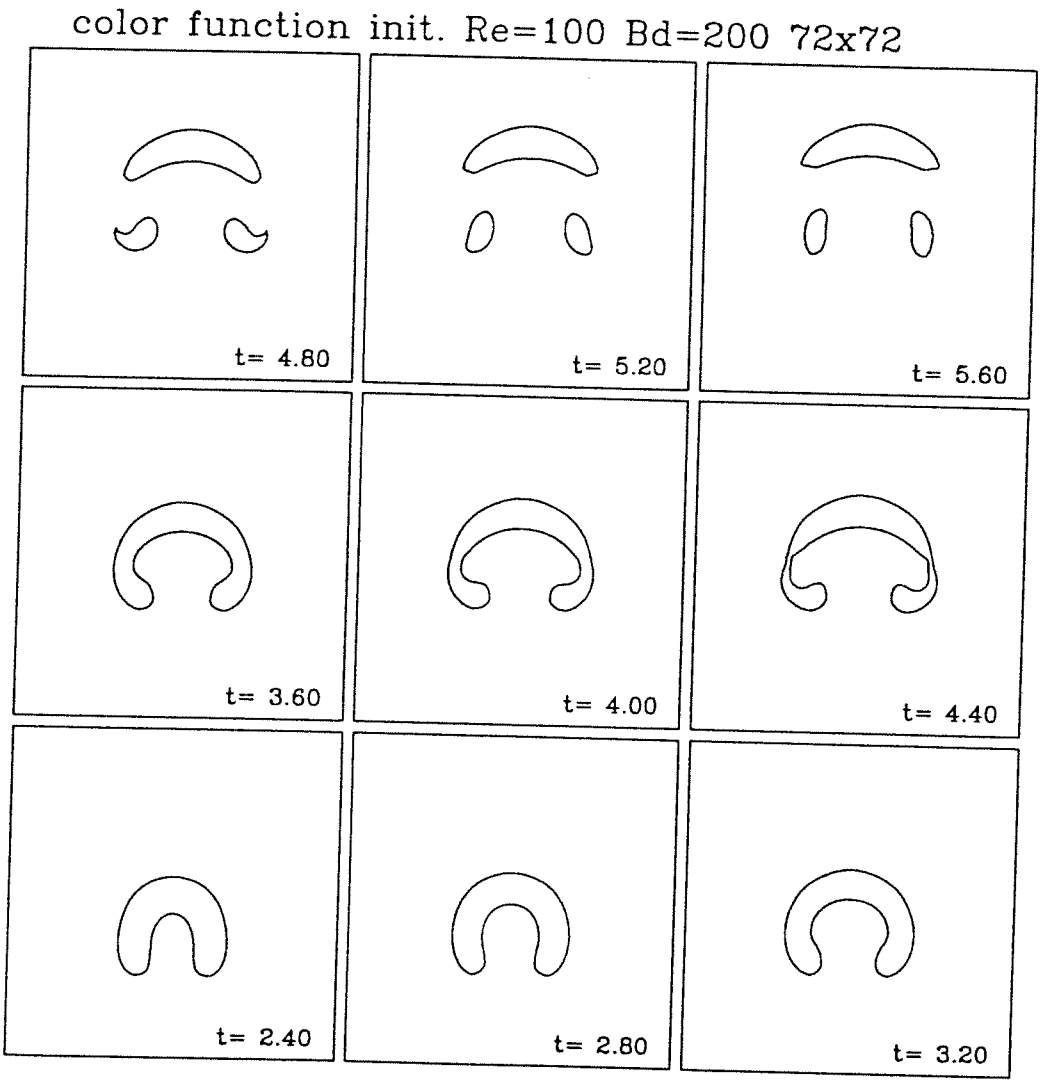

Figure 7.34: Rising gas bubble with medium range Reynolds number and low surface tension. Initial level set function is -1 in the bubble and 1 outside.

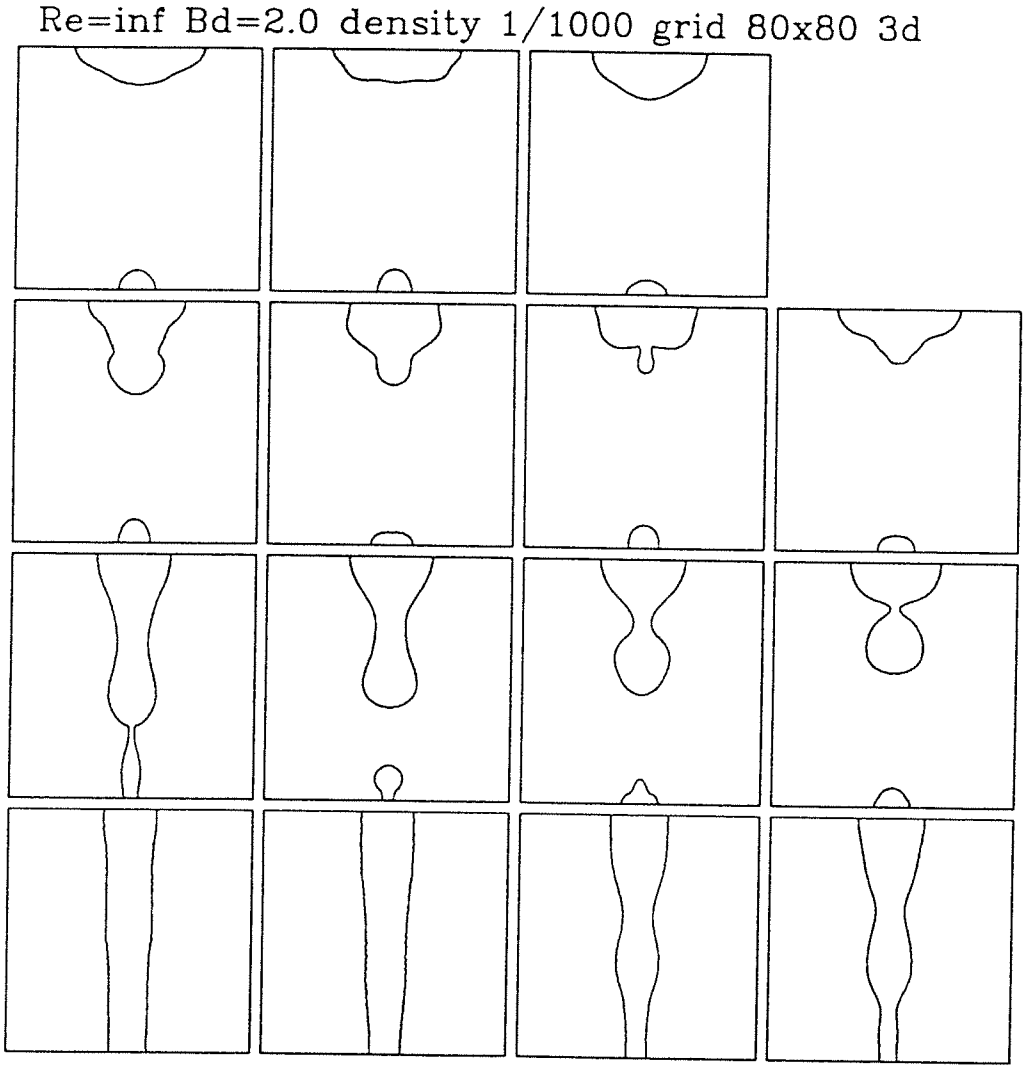

Figure 7.35: A slightly perturbed cylindrical column of fluid with surface tension (viscous and gravitational forces are zero) breaks up. Jet evolves in time from left to right and bottom to top. $t_0 = 12$, $t_4 = 20$, $t_8 = 24$, ...

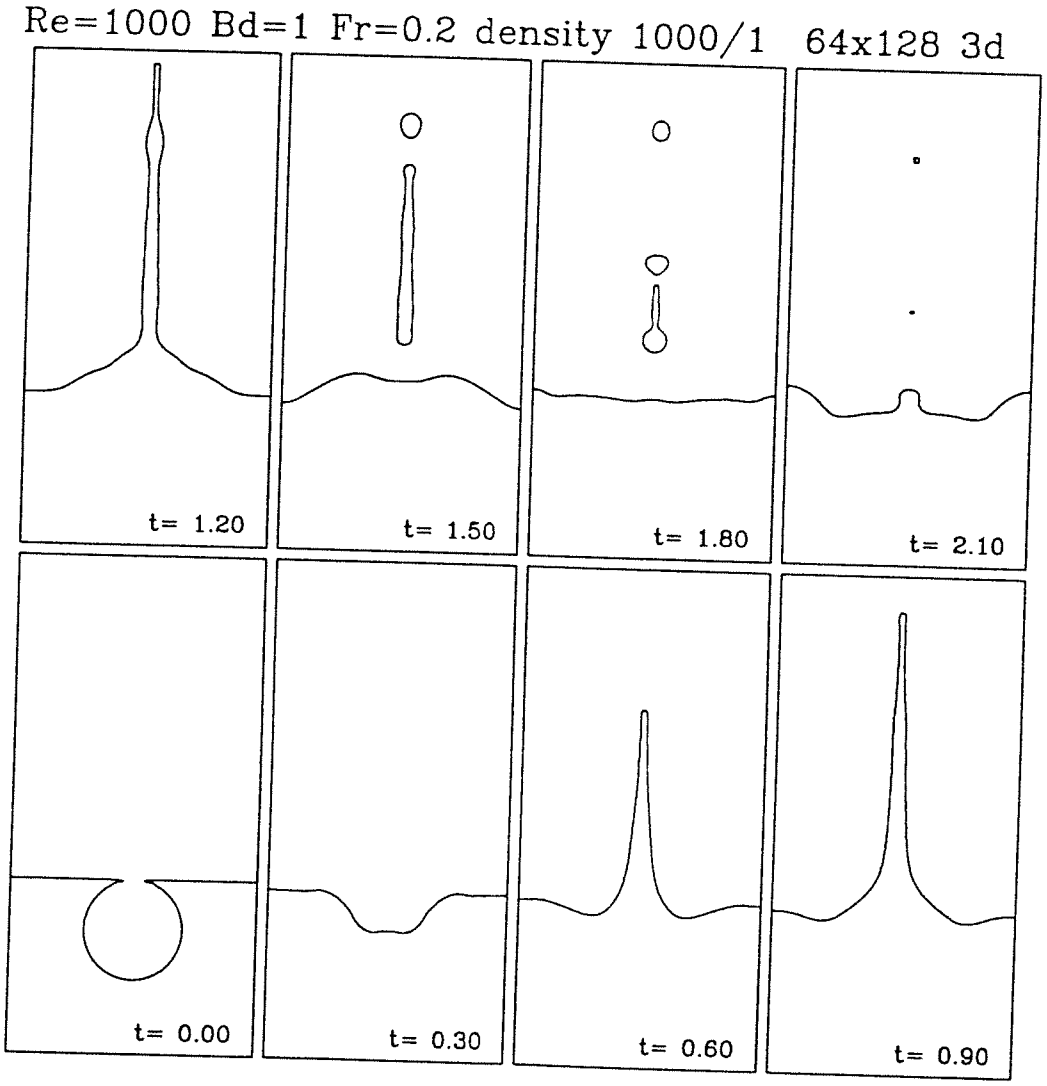

Figure 7.36: Upon rupture of a gas bubble at an air/water interface, surface tension effects cause a high speed jet of water to form.

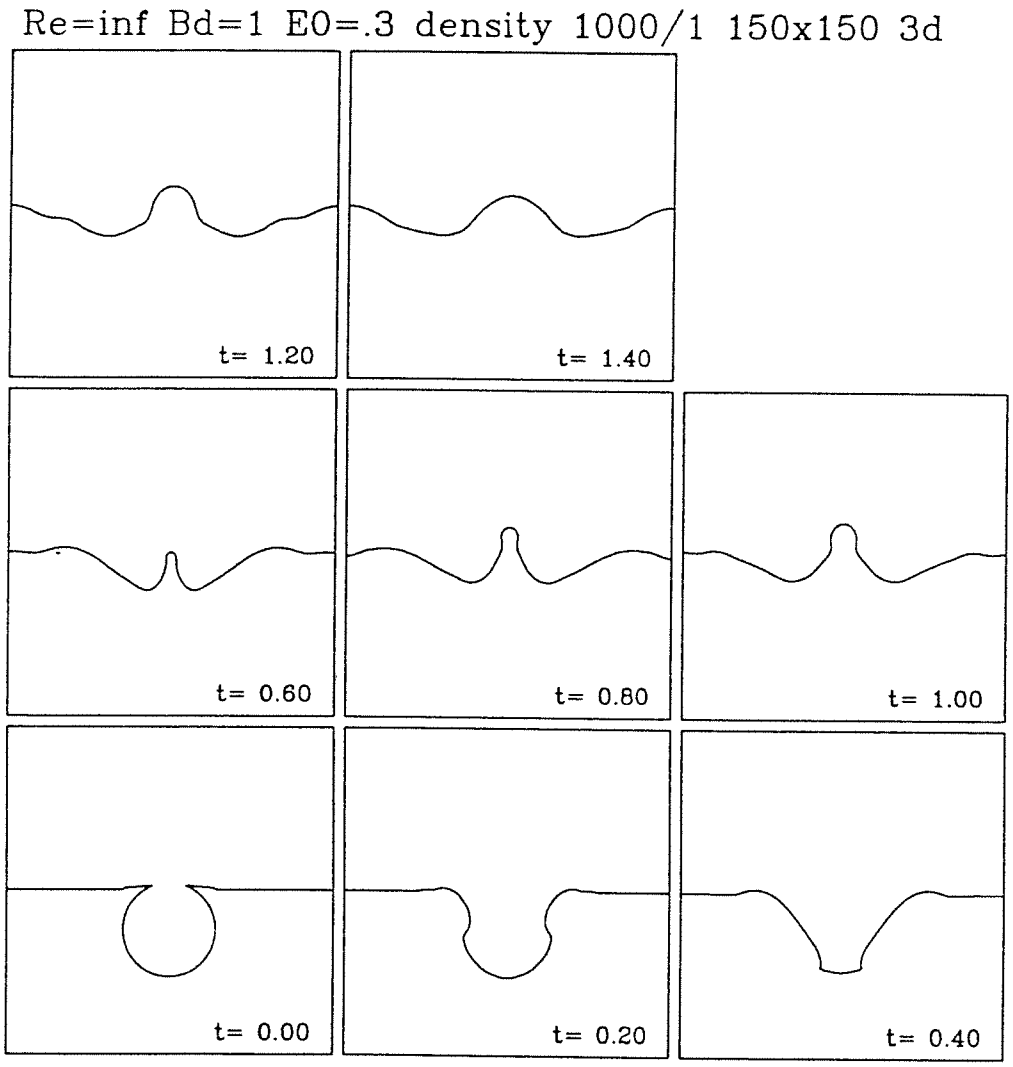

Figure 7.37: Results of a "pre-ruptured" gas bubble using an initial profile dependent on the Eotvos number. Viscous forces are zero.

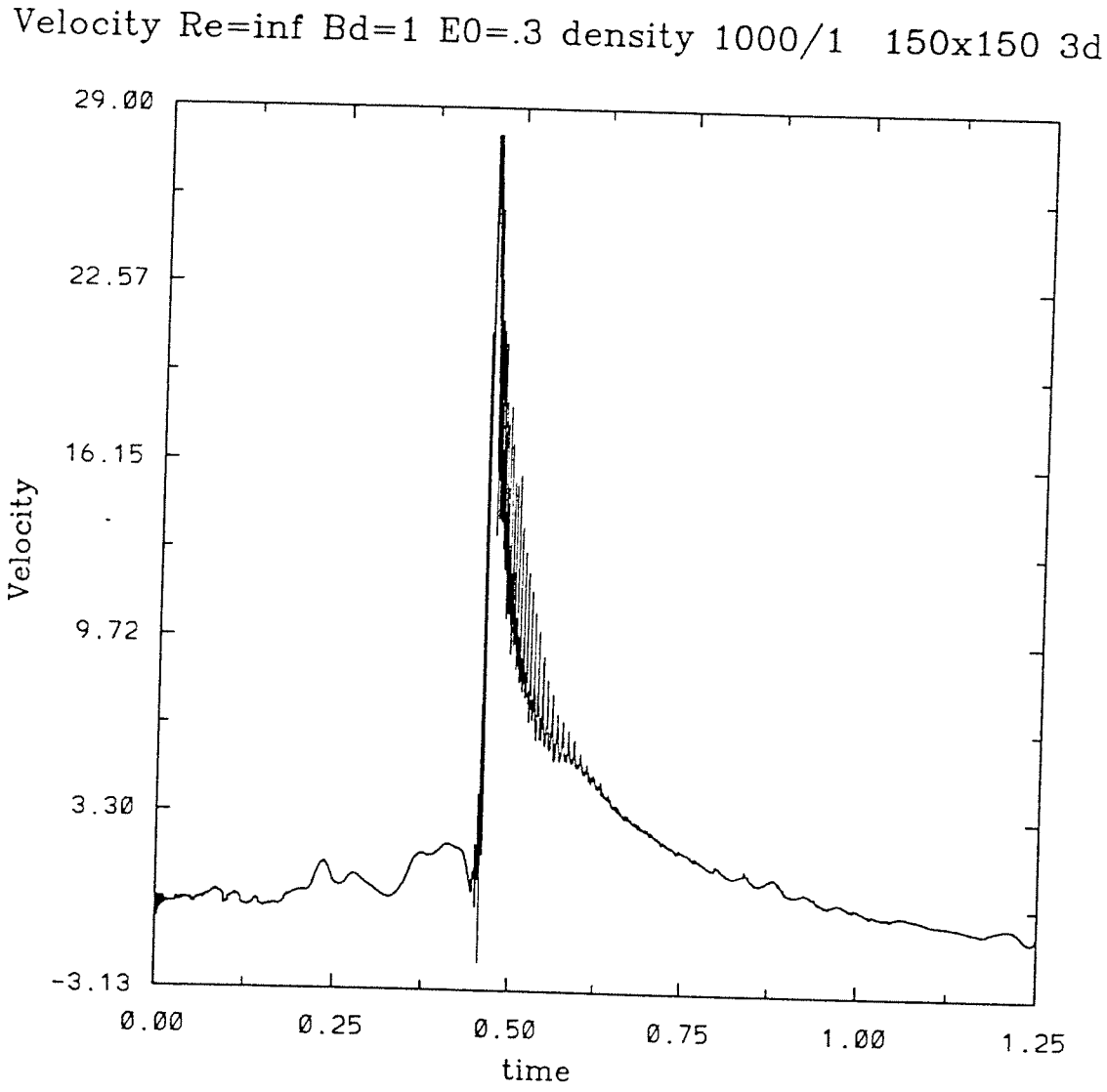

Figure 7.38: Velocity profile of water jet emitted during the evolution of a "pre-ruptured" gas bubble $E0 = 0.3$.

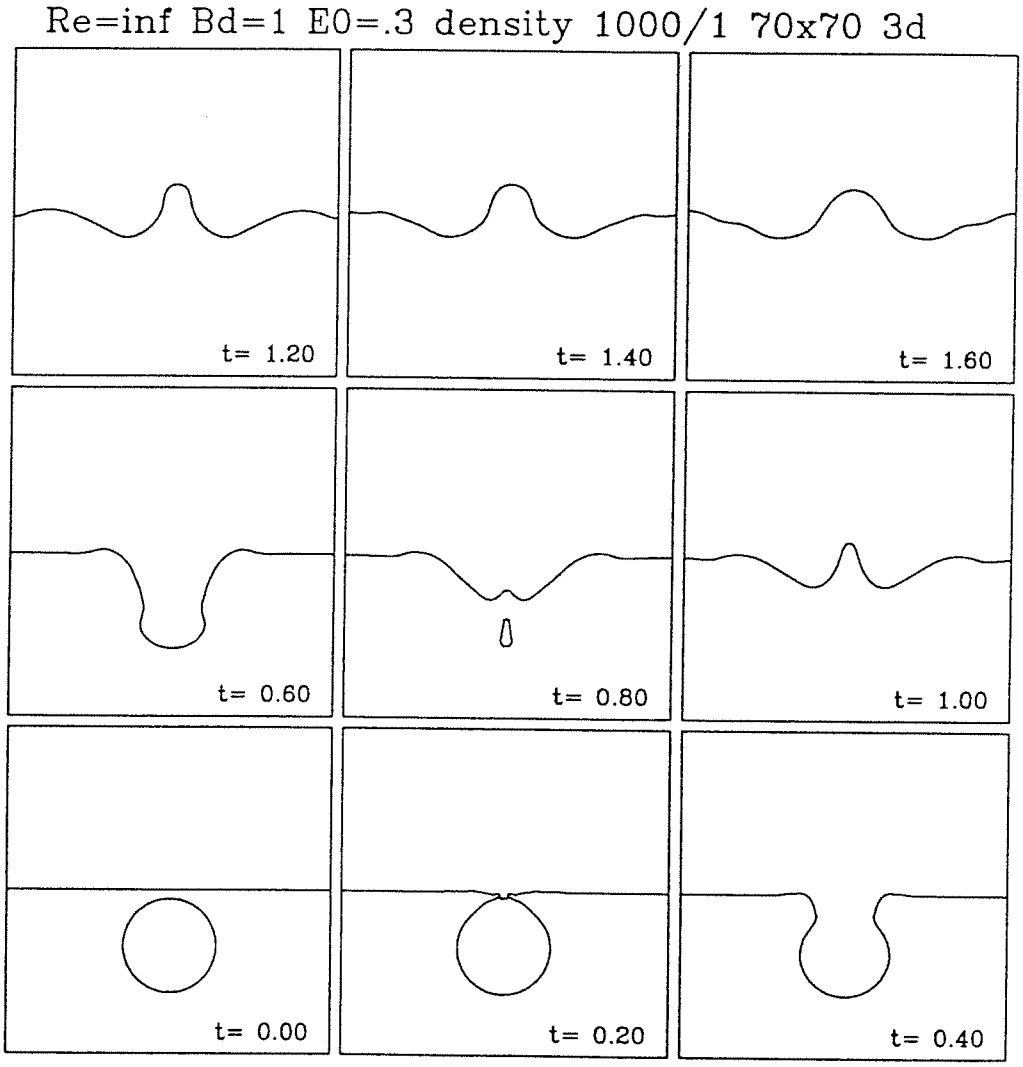

Figure 7.39: Gas bubble allowed to rise to surface and then rupture. Results should be compared with "pre-ruptured" case.

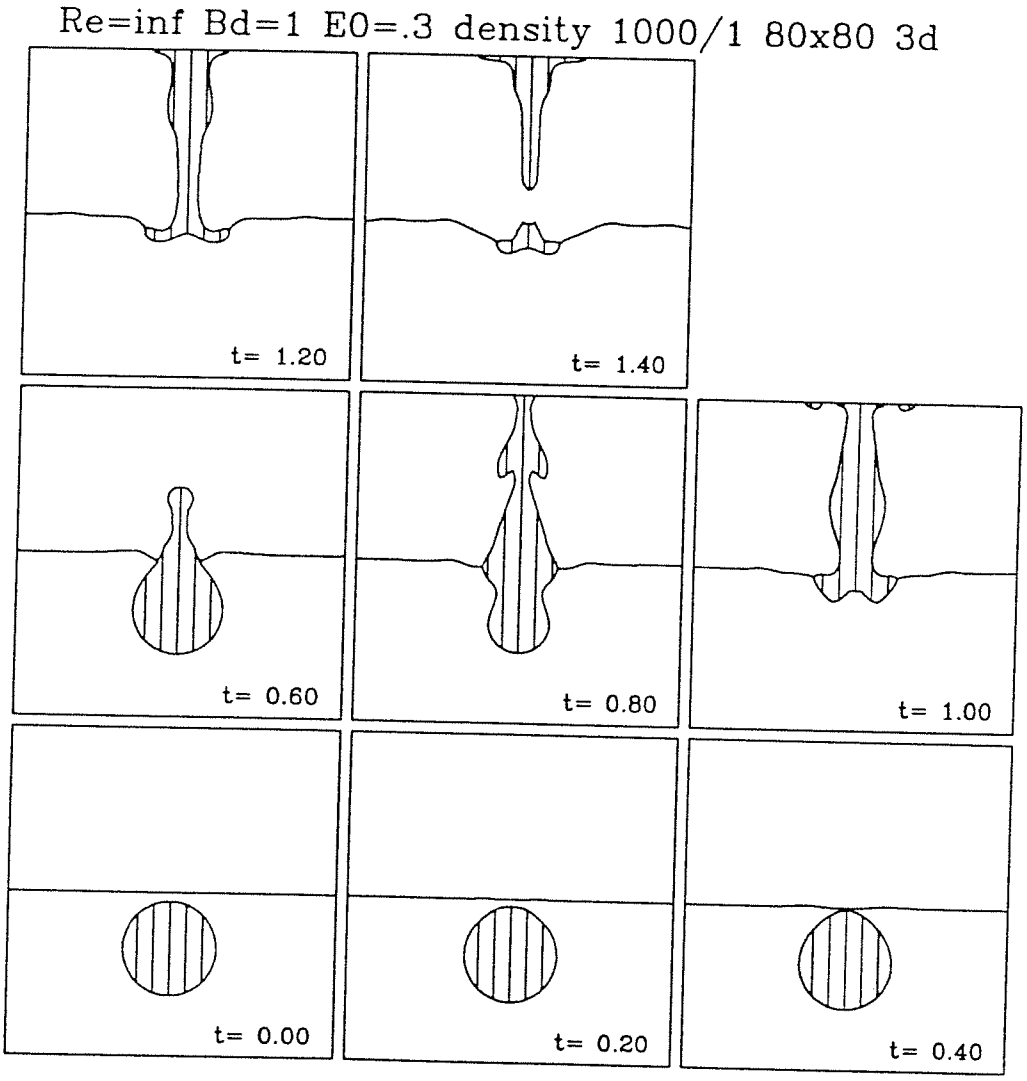

Figure 7.40: Gas bubble allowed to rise to surface and then rupture. Surface tension is modeled using average of level set functions active at the interface.

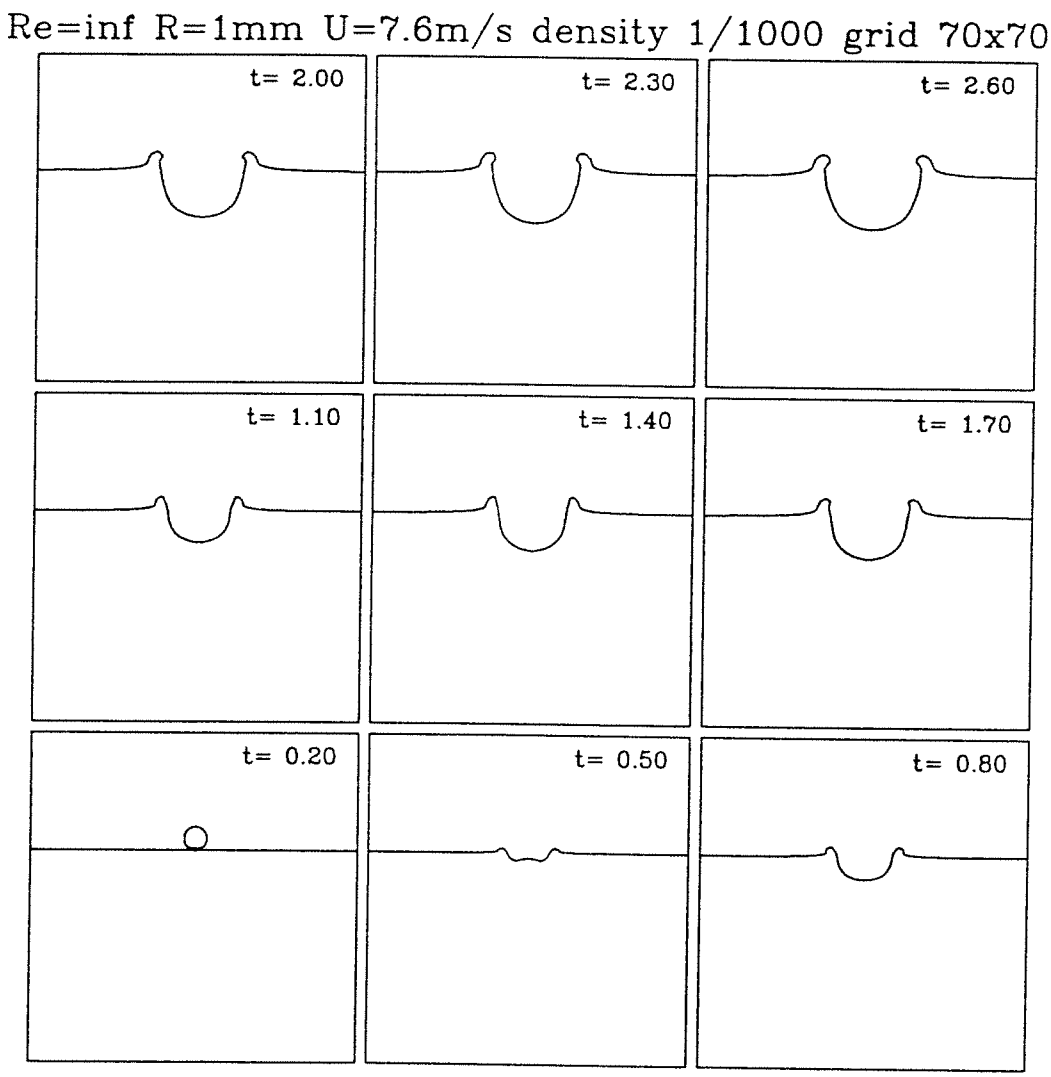

Figure 7.41: Water drop splashes against water surface.

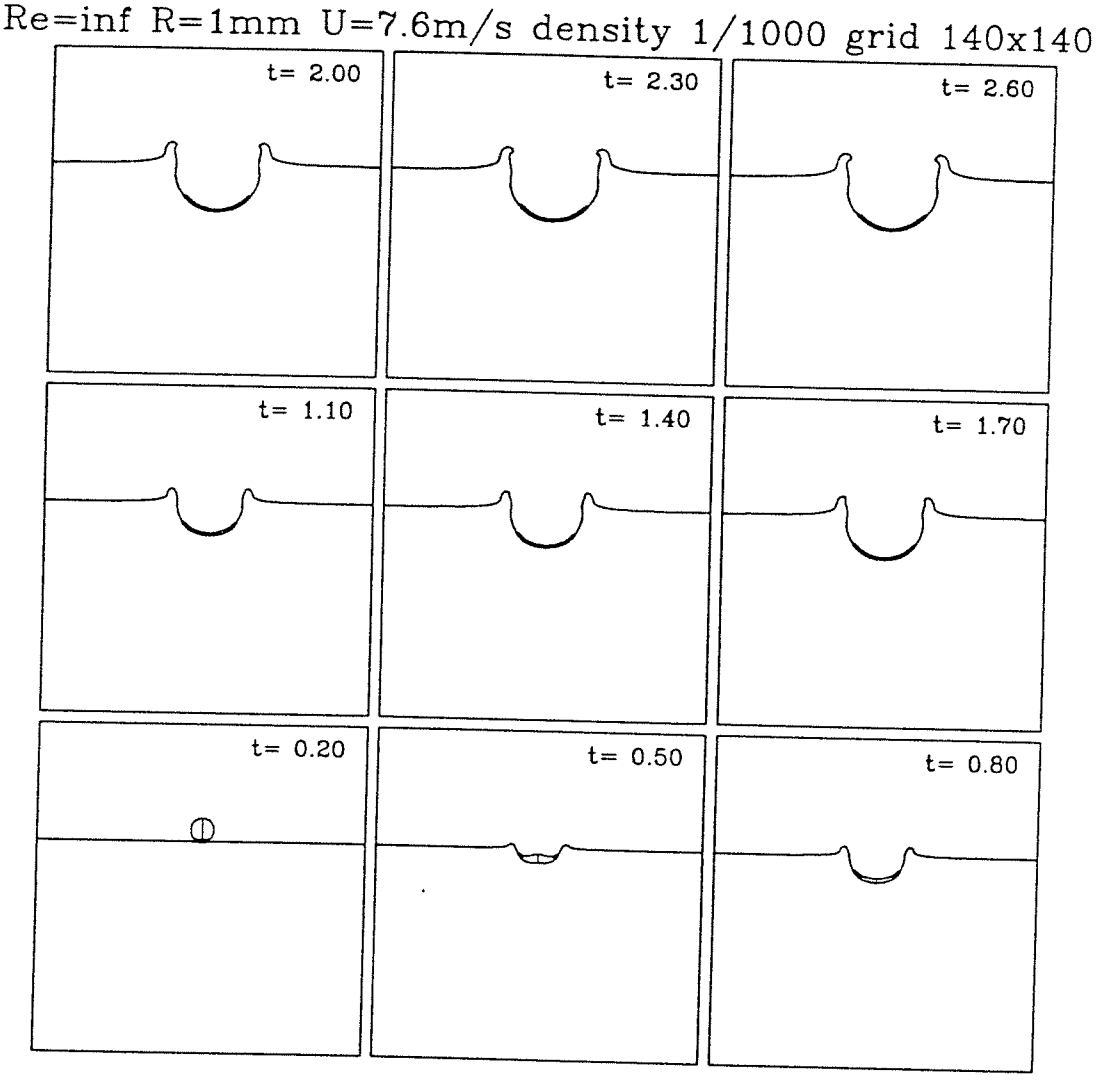

Figure 7.42: Water drop splashes against water surface. Extra interface between drop and surface is tracked throughout simulation. Surface tension is modeled using ϕ_1 and ϕ_3.

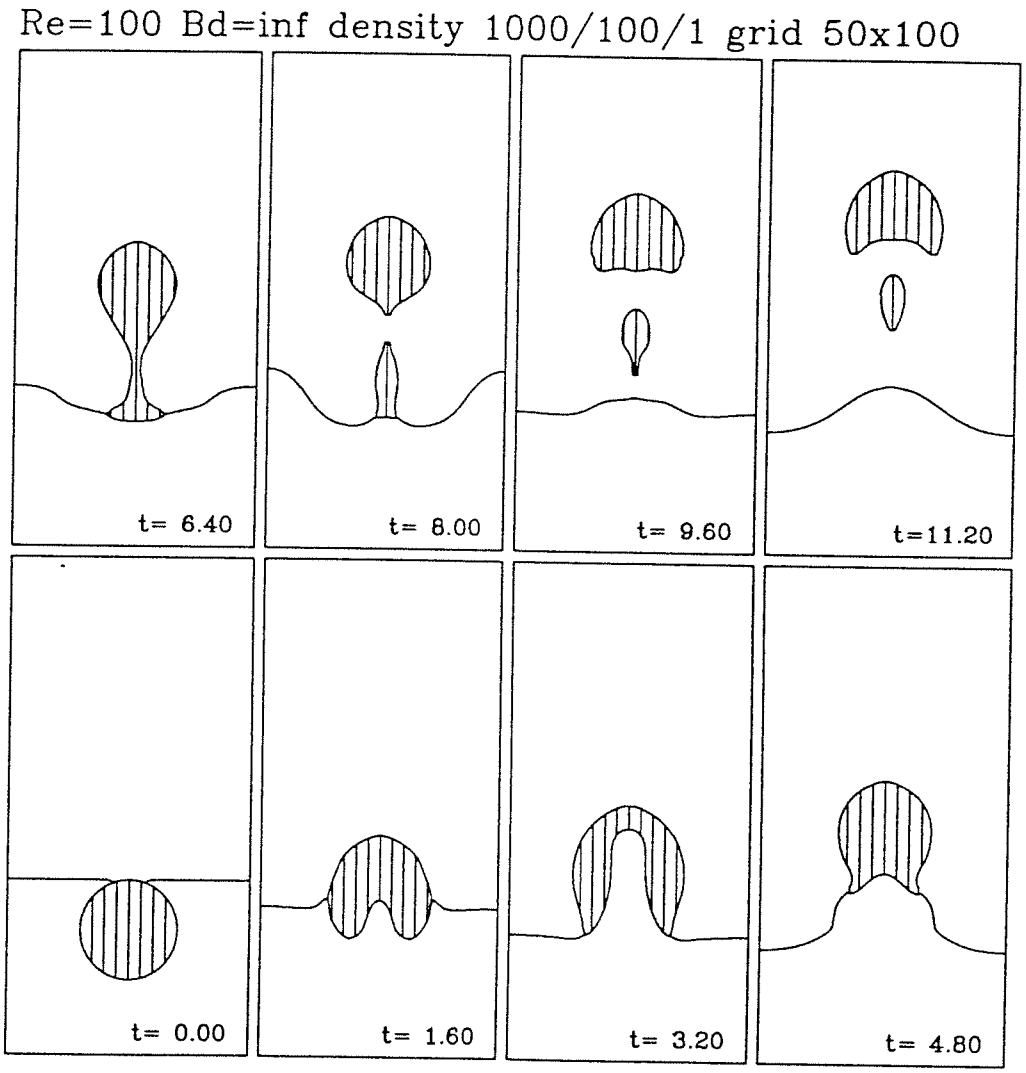

Figure 7.43: Air bubble rises through a water/"oil" interface. "oil" is a less dense but more viscous fluid. Surface tension effects are ignored.

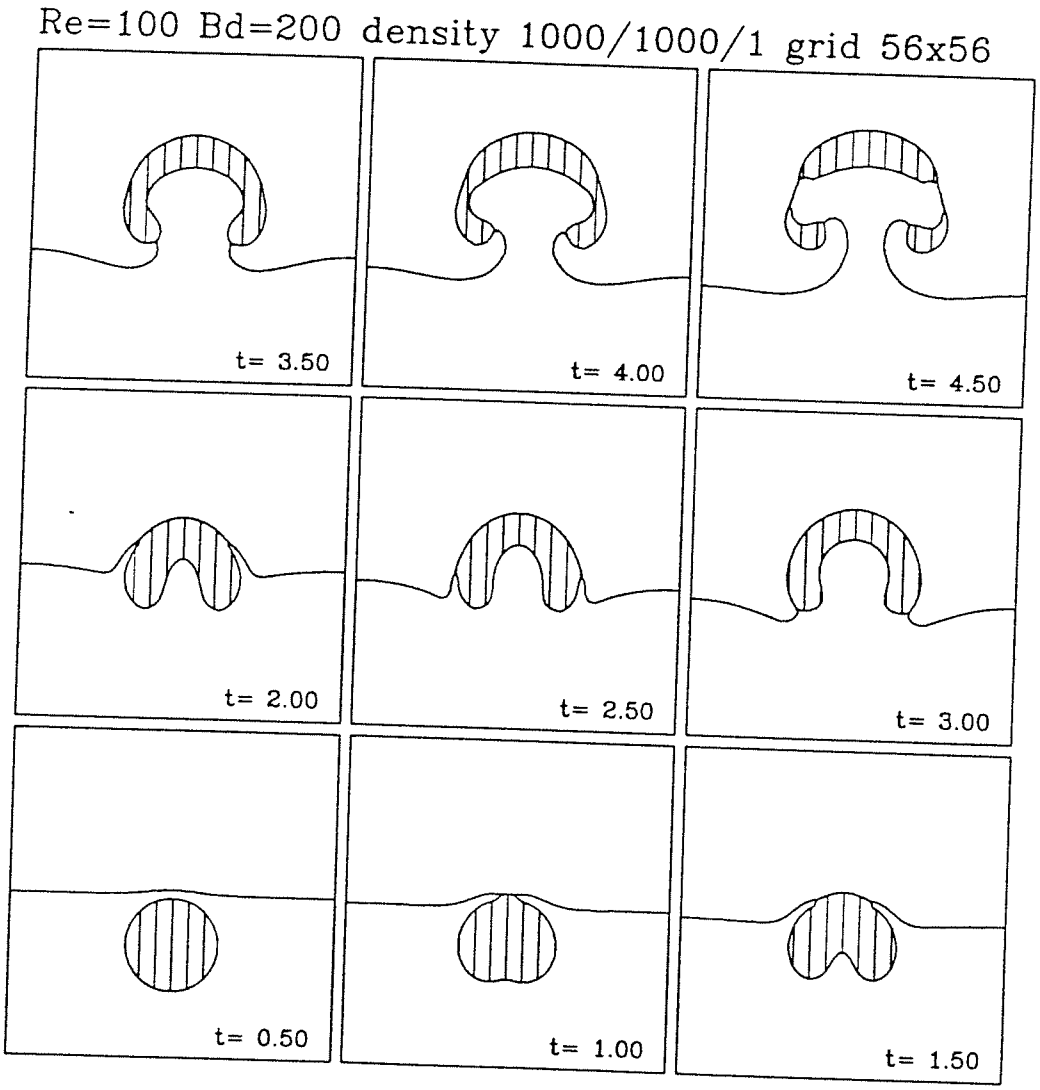

Figure 7.44: Air bubble rises through a water/water interface. Results compare well with the "one level set" version with $Re = 100$ and $B = 200$.

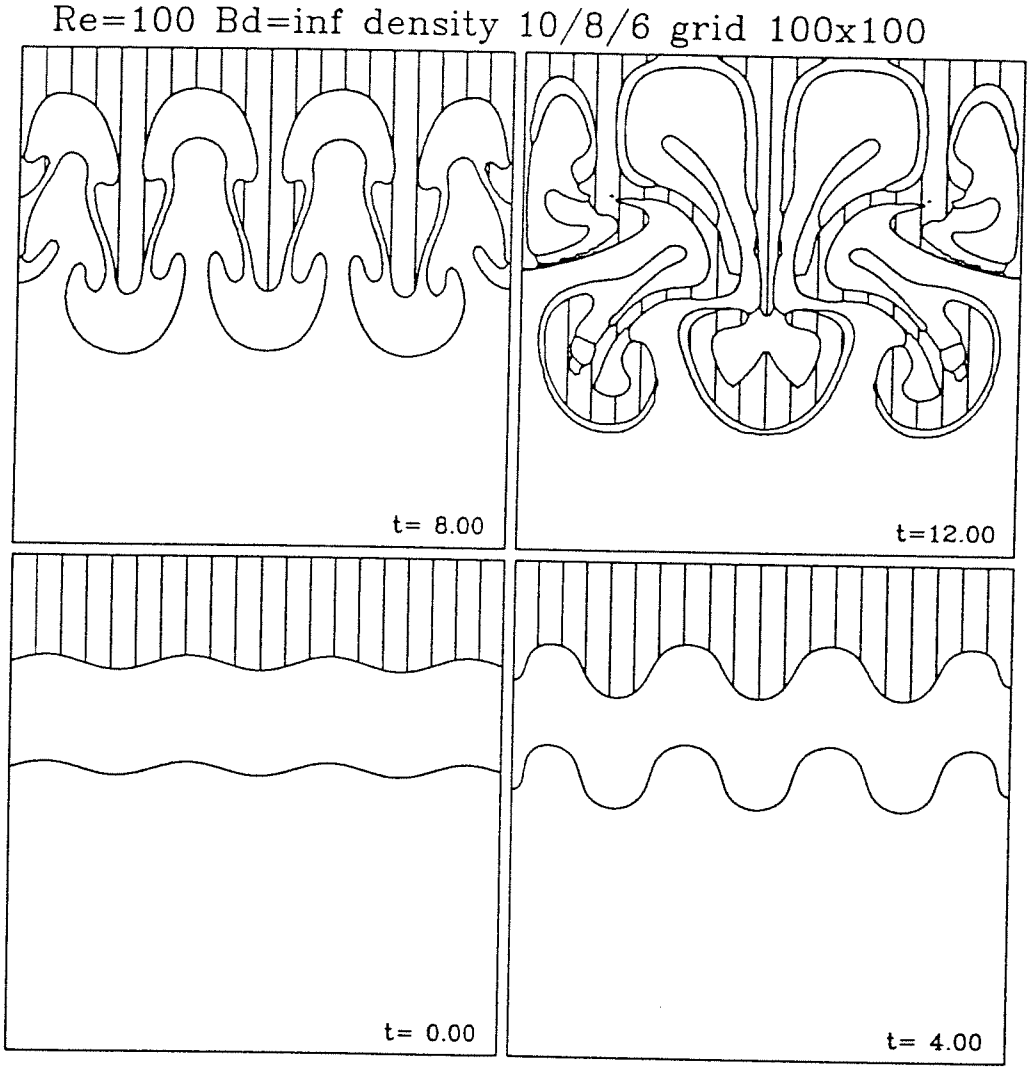

Figure 7.45: Rayleigh-Taylor instabilities occur when three fluids are layered: heavy,medium, and light. Flow assumed to have medium range Reynolds number and no surface tension.